

Copyright
by
Kyoung Eun Kweon
2012

The Dissertation Committee for Kyoung Eun Kweon

Certifies that this is the approved version of the following dissertation:

First Principles Study of Point-Like Defects and Impurities

in Silicon, Carbon and Oxide Materials

Committee:

Gyeong S. Hwang, Co-Supervisor

Sanjay K. Banerjee, Co-Supervisor

Jack Lee

Emanuel Tutuc

James R. Chelikowsky

**First Principles Study of Point-Like Defects and Impurities
in Silicon, Carbon and Oxide Materials**

by

Kyoung Eun Kweon, B.S.; M.S.E.

Dissertation

Presented to the Faculty of the Graduate School of

The University of Texas at Austin

in Partial Fulfillment

of the Requirements

for the Degree of

Doctor of Philosophy

The University of Texas at Austin

May 2012

To my parents, Youngman Kweon and Jungyoon Shim;
my husband Sejoon Yang

Acknowledgements

I would like to gratefully thank Dr. Gyeong S. Hwang for his supervision, guidance, and patience during my graduate studies. He provided me with tremendous opportunities and support in developing my expertise in computational material science. He always encouraged me to think of the big picture implications of my research and helped me figure out the details. Whenever I faced difficulties in my work, he sat down and discussed the problems with me for hours until I found out how to solve them. His scientific insight and intuition as well as knowledge inspire me as a researcher I want to be. I truly respect his passionate attitude toward science, which might be one of the most important virtues of a good scientist. I would also like to thank Dr. Sanjay Banerjee, Dr. Jack Lee, Dr. Emanuel Tutuc, and Dr. James Chelikowsky for agreeing to serve on my dissertation committee and for all of their thoughtful advice and help.

I would also like to express my gratitude to Dr. John Goodenough, professor of mechanical engineering and material science. When I took his class in 2007, even though he was in his mid 80's, he was the most passionate professor I'd ever seen. He is a sincere scientist and teacher who really enjoys his work and wants to share his knowledge with his students to help create a better world. This was not limited to scientific knowledge; he taught me that I should contribute to the greater good of society as an educated person. I also appreciate the valuable discussions with Dr. Allen Bard and his Ph. D student, Hyun S. Park on photoelectrochemistry. Through discussion with them, I realized the importance of establishing harmony between theoretical calculations and experiments for a better fundamental understanding of the science.

I would also like to thank all of the members of Dr. Hwang's research group. They include Soohwan Lee, Sangheon Lee, Robert J. Bondi, Hyun Woo Kim, Hyung

Chul Ham, Eunsu Paek, Adam Stephens, Yongjin Lee, Chia-Yun Chou, Dhivya Manogaran, Yuhao Tsai, and Alex Pak. Especially, I appreciate Eunsu Paek, Adam Stephens, and Chia-Yun Chou for their close friendship. They always listened to me and helped me to solve my problems.

Also, I would like to thank all my friends in Austin. With them, I felt comfort as if I was home and we shared many memories. Through their emotional support, I was able to successfully accomplish my journey toward earning my Ph. D in the University of Texas at Austin.

I would like to thank my parents, Youngman Kweon and Jeongyoon Shim for all of their support and unconditional love. They believed in me and had great faith in my academic success through my graduate studies. They are really wonderful parents and, at the same time, advisors in my life. They taught me the importance of diligence and effort and encouraged me to make good choices in my life. I thank my two younger sisters, Jieun and Bomin. They always make me laugh and are my best friends in my life journey. Finally, but most importantly, I would like to express deepest thanks to my husband, Sejoon Yang, for his support and love. He respects me as a fellow researcher and has encouraged me to pursue my career throughout my graduate studies. Also, I would like to thank my husband's parents for understanding and believing in me to successfully finish my studies.

Kyoung Eun Kweon

The University of Texas at Austin

May 2012

First Principles Study of Point-Like Defects and Impurities in Silicon, Carbon and Oxide Materials

Publication No. _____

Kyoung Eun Kweon, Ph. D.

The University of Texas at Austin, 2012

Supervisors: Gyeong S. Hwang and Sanjay K. Banerjee

Since materials properties are determined by the interactions between the constituent atoms, an accurate description of the inter-atomic interactions is crucial to characterize and control material properties. Particularly, a quantitative understanding of the formation and nature of defects and impurities becomes increasingly important in the era of nanotechnology, as the imperfections largely influence many properties of nanoscale materials. Indeed, due to its technological importance and scientific interest, there have been significant efforts to better understand their behavior in semiconductors and oxides, and their interfaces, yet many fundamental aspects are still ambiguous due largely to the difficulty of direct characterization. Hence, our study has focused on developing a better understanding of atomic-scale defects and impurities using first principles quantum mechanical calculations. In addition, based on the improved understanding, we have attempted to address some engineering problems encountered in the current technology.

The first part of this thesis focuses on mechanisms underlying the transient enhanced diffusion of arsenic (As) during post-implantation annealing by examining the interaction of As with vacancies in silicon. In the second part, we address some fundamental features related to plasma-assisted nitridation of silicon dioxide; this study shows that oxygen vacancy related defects play an important role in (experimentally observed) peculiar nitridation at the Si/SiO₂ interface during post O₂ annealing. In the third part, we examine the interaction between vacancies and dopants in *sp*²-bonded carbon such as graphene and nanotube, specifically the formation and dynamics of boron-vacancy complexes and their influence on the electrical properties of host materials. In the fourth part, we study the interfacial interaction between amorphous silica (*a*-SiO₂) and graphene in the presence of surface defects in *a*-SiO₂; this study shows possible modifications in the electronic structure of graphene upon the surface defect assisted chemical binding onto the *a*-SiO₂ surface. In the last part, we examine the structural and electronic properties of bismuth vanadate (BiVO₄) which is a promising photocatalyst for water splitting to produce hydrogen; this study successfully explains the underlying mechanism of the interesting photocatalytic performance of BiVO₄ that has been experimentally found to strongly depend on structural phase and doping.

Table of Contents

List of Tables.....	xii
List of Figures.....	xiii
Chapter 1: Introduction.....	1
Chapter 2: Theoretical Backgrounds.....	5
2.1 Hartree-Fock Theory.....	5
2.2 Kohn-Sham Theory.....	7
2.3 Exchange-Correlation Functional.....	10
2.3.1 Local Density Approximation.....	10
2.3.2 Generalized Gradient Approximation.....	12
2.4 Ion Potential.....	13
Chapter 3: Structure and Dynamics of Arsenic-Silicon Interstitial Complexes in Crystalline Silicon	17
3.1 Introduction	17
3.2 Calculation Methods.....	17
3.3 AsI.....	18
3.4 As ₂ I	22
3.5 AsI ₂	26
3.6 As ₂ I ₂	30
3.7 Summary.....	34
Chapter 4: Prediction of Defect Mediated N ₂ O Formation from N ₂ and O ₂ in Amorphous Silica.....	36
4.1 Introduction	36
4.2 Calculation Methods.....	38
4.3 Positively Charged Oxygen Vacancy: Structural Transformation, Energetics, and Migration.....	38
4.3.1 Positively charged dimer configuration.....	39
4.3.2 Back puckered configuration.....	40

4.3.3 Front puckered configuration.....	42
4.3.4 Migration of positively charged oxygen vacancy.....	44
4.4 Interaction Between Positively Charged Oxygen Vacancy and Molecular N ₂	45
4.4.1 Positively charged dimer configuration.....	45
4.4.2 Si dangling bond type.....	46
4.5 Interaction Between Positively Charged Oxygen Vacancy and Molecular O ₂	49
4.5.1 Positively charged dimer configuration.....	49
4.5.2 Si dangling bond type.....	51
4.6 Oxygen Vacancy Mediated Reaction Between N ₂ and O ₂	52
4.6.1 Peroxy linkage.....	52
4.6.2 Peroxy oxygen radical.....	54
Chapter 5: Formation, Structure, and Bonding of Boron-Vacancy Pairs in Graphene: A First Principles Study.....	56
5.1 Introduction	56
5.2 Calculation Methods.....	57
5.3 Substitutional Boron.....	58
5.4 Single Vacancy.....	60
5.5 Boron-Vacancy Pair.....	64
5.5.1 Formation of BV pair.....	64
5.5.2 B + V ↔ BV.....	66
5.5.3 BV + V ↔ BV ₂	68
5.6 Conclusions.....	69
Chapter 6: Boron-Vacancy Pairing and Its Effect on the Electronic Properties of Carbon Nanotubes	71
6.1 Introduction	71
6.2 Calculation Methods.....	72
6.3 Structure and Energetics of Boron, Vacancy, and Boron-Vacancy Pair...	74
6.4 Electronic Structure and Transmission.....	82

6.5 Conclusions.....	87
Chapter 7: Defect-assisted Covalent Binding of Graphene to an Amorphous Silica Surface: A Theoretical Prediction.....	88
7.1 Introduction	88
7.2 Calculation Methods.....	89
7.3 Results and Discussion.....	91
7.4 Conclusions.....	99
Chapter 8: Structure, Bonding, and Electronic Properties of BiVO ₄ : A Hybrid Density Functional Theory Study.....	100
8.1 Introduction	100
8.2 Crystal Structure And Bonding Mechanism.....	103
8.3 Calculation Methods.....	105
8.4 Relative Phase Stability and Lattice Parameters: Tetragonal vs. Monoclinic.....	106
8.5 Electronic Structure Description: Conventional vs. Hybrid DFT.....	110
Chapter 9: Formation and Transport of Excess Charge Carriers in BiVO ₄ : A Hybrid Density Functional Theory Study.....	118
9.1 Introduction	118
9.2 Calculation Methods.....	119
9.3 Nature of Excess Hole.....	120
9.3.1 Structure and stability.....	120
9.3.2 Transport.....	125
9.4 Nature of Excess Electron.....	126
9.4.1 Structure and stability.....	126
9.4.2 Transport.....	130
9.5 Summary.....	131
References.....	133
Vita.....	149

List of Tables

- Table 6.1: Selected C-C and C-B bond lengths (d) and C-B-C bend angles (\angle) for relaxed B_s , V , B_s - V geometries for different tube sizes $[(n, n)$ CNTs; $n = 4-7$, corresponding to $D = 5.6-9.6$ Å]. For comparison, the corresponding bond lengths and bend angles in flat graphene (Gr) are also listed. The bond lengths and bend angles are given in Å and degree($^\circ$), respectively. See Figs. 6.2 and 6.3 for the atom labels 78
- Table 7.1: Optimized geometrical parameters for (a) silylene site (SS), (b) dioxasilirane group (DOSG), and (c) DOSG/graphene (DOSG/Gr) and calculated total energy changes for the $SS + O_2$ (ΔE_1) and $DOSG + Gr$ (ΔE_2) reactions from cluster and periodic slab DFT-GGA (PW91) calculations. In the slab calculations, three independent slab models were employed. The distances (d) and angles (θ) are given in Å and degree ($^\circ$), respectively. The energy values (ΔE_1 , ΔE_2) are in eV; the negative sign indicates energy gain during the reaction. 92
- Table 8.1: Experimental crystallographic parameters for monoclinic (at 4.5K and 295K) and tetragonal (at 566K) $BiVO_4$ from neutron powder data. The measured atomic fractional positions of all atoms and the bond lengths are also listed. 104
- Table 8.2: Optimized lattice parameters of tetragonal and monoclinic $BiVO_4$ from corresponding calculations (PBE, HF10%, HF25%, and HF50%). The bond lengths (Bi-O and V-O) are also summarized 109
- Table 8.3: Calculated Bader Charges (Q_B) and Volumes (V_B) of Bi, V, O atoms in ts - $BiVO_4$ and ms - $BiVO_4$ from HF50% calculation. Values in parentheses in table indicate calculated values from PBE calculation at the fixed geometry (obtained from HF50%)..... 111
- Table 8.4: Calculated band gaps of ts - $BiVO_4$ and ms - $BiVO_4$ from HF 25% and HF 50% 117

List of Figures

Figure 2.1:	Kohn-Sham diagram	8
Figure 2.2:	Self consistent Kohn-Sham equation diagram	10
Figure 2.3:	Analysis of a Si atom with core and valence electrons.....	13
Figure 2.4:	Comparison between pseudo and all-electron wavefunction and between pseudopotential and all-electron potential	14
Figure 2.5:	Oxygen 2p radial function with all-electron (AE) potential, norm-conserving pseudopotential (NC PPT), and ultrasoft pseudopotential (US PPT)	16
Figure 3.1:	The diffusion pathway for AsI [(a)-(e)]. The corresponding energy pathway (in eV) is shown. The blue (dark-colored) and white ball represent As and Si atoms, respectively	19
Figure 3.2:	(Upper Panel) The pathway for AsI ⁰ and AsI ⁺ dissociation. The blue (dark-colored) and white ball represent As and Si atoms, respectively. (Lower Panel) Corresponding energy barriers (in eV) of AsI ⁰ (solid line) and AsI ⁺ (dashed line) dissociation.	21
Figure 3.3:	(Upper Panel) The diffusion pathway for As ₂ I ⁰ [(a)-(a')]. The As atoms are labeled AsI and AsII, while Si atoms involved are labeled A-G. The blue (dark-colored) and white ball represent As and Si atoms, respectively. (Lower Panel) Corresponding energy pathway (in eV) of As ₂ I ⁰ (solid line) and As ₂ I ⁺ (dashed line) diffusion.	23
Figure 3.4:	(Upper Panel) The dissociation pathway for As ₂ I ⁰ [(a)-(e)]. The blue (dark-colored) and white ball represent As and Si atoms, respectively. (Lower Panel) Corresponding energy pathway (in eV) of As ₂ I ⁰ (solid line) and As ₂ I ⁺ (dashed line) dissociation.....	25
Figure 3.5:	(Upper Panel) The pathway for AsI ₂ diffusion [(a)-(c)]. The relevant Si atoms are labeled A-D. The blue (dark-colored) and white ball represent As and Si atoms, respectively. (Lower Panel) Corresponding diffusion energy pathway (in eV) of AsI ₂ ⁰ (solid line) and AsI ₂ ⁺ (dashed line).27	

- Figure 3.6: (Upper Panel) The pathway for AsI_2^+ dissociation [(a)-(d)]. The relevant Si atoms are labeled A-D. The blue (dark-colored) and white ball represent As and Si atoms, respectively. (Lower Panel) Energetics (in eV) along the AsI_2^+ dissociation pathway 28
- Figure 3.7: (Upper Panel) The diffusion pathway for As_2I_2 [(a)-(a')]. The As atoms are labeled I and II, while Si atoms involved are labeled A and B. The blue (dark-colored) and white ball represent As and Si atoms, respectively. (Lower Panel) Corresponding energetics (in eV) along the As_2I_2^0 (solid line) and As_2I_2^+ (dashed line) diffusion pathway..... 31
- Figure 3.8: (Upper Panel) The dissociation pathway for As_2I_2 [(a)-(a')]. The As atoms are labeled I and II, while Si atoms involved are labeled A-D. The blue (dark-colored) and white ball represent As and Si atoms, respectively. (Lower Panel) Corresponding energetics (in eV) along the As_2I_2^0 (solid line) and As_2I_2^+ (dashed line) dissociation pathway... 33
- Figure 4.1: (a) neutral and (b) positively charged Si-Si dimer configuration (indicated as A and B). The isosurfaces of Wannier functions (blue colored) show the paired ($\uparrow\downarrow$) and unpaired (\uparrow) electron density for the neutral [(a)] and positively charged [(b)] state, respectively. The gray and red colored balls represent Si and O atoms, respectively. 39
- Figure 4.2: Two predicted paths for transformation of positively charged dimers [(b1) and (b2)] to back puckered configurations [(c1) and (c2)] and configurations after trapping one additional electron are shown in (d1) and (d2), respectively. The blue-colored isosurfaces show the unpaired (\uparrow) and paired ($\uparrow\downarrow$) electron and the white isosurfaces show the lone pair of the O_B atom which forms a dative covalent bond with the positively charged Si atom. The gray and red colored balls represent Si and O atoms, respectively. 41
- Figure 4.3: Predicted path for the transformation of a positively charged dimer [(b)] to a front puckered configuration [(c)] and configuration after trapping one additional electron is shown in (d). The blue-colored isosurfaces show the unpaired (\uparrow) and paired ($\uparrow\downarrow$) electron and the white isosurfaces show the lone pair of the O_F atom which forms a dative covalent bond with the positively charged Si atom..... 42
- Figure 4.4: Predicted migration pathway for the puckered configuration..... 44

- Figure 4.5: N₂ insertion into a positively charged dimer configuration: cluster model calculation [(a) and (b)] and *α*-SiO₂ bulk calculation [(c) and (d)]. The gray, red, blue, and white colored balls represent Si, O, N, and H atoms, respectively. All distances are given in Å. 45
- Figure 4.6: Interaction of N₂ molecule with (a) ≡Si• and (b) ≡Si⁺, and interaction of H₂O molecule with (c) ≡Si⁺ from cluster model calculations. N₂ interaction with (d) a back puckered, (e) front puckered, and (f) isolated E' center in the bulk system..... 47
- Figure 4.7: O₂ insertion into a positively charged dimer configuration: cluster model calculation [(a) and (b)] and *α*-SiO₂ bulk calculation [(c) and (d)]. The gray, red, and white colored balls represent Si, O, and H atoms, respectively 50
- Figure 4.8: Interaction of O₂ molecule with (a) ≡Si• and (b) ≡Si⁺ from cluster model calculations. O₂ interaction with (c) a back puckered, (d) front puckered, and (e) isolated E' center in the bulk system. 51
- Figure 4.9: Predicted reaction path for formation of a N₂O molecule from a peroxy linkage (≡Si-O-O-Si≡) and N₂ molecule. The corresponding energy pathway (in eV) is shown. 53
- Figure 4.10: Predicted reaction path for formation of a N₂O molecule from a peroxy oxygen radical (≡Si-O-O•) and N₂ molecule. The corresponding energy pathway (in eV) is shown. 54
- Figure 5.1: Optimized configurations (upper panels) and corresponding electronic band structure and total density of states (DOS) (bottom panels) of (a) pristine and (b) 0.9% boron-doped graphene sheets. Grey and black (blue) balls represent C and B atoms, respectively, and the C-C and C-B bond lengths indicated are given in Å. In each band structure and DOS plot, the Dirac energy (E_D) is set to 0 eV while the horizontal dotted line indicates the Fermi level position. In (b) the B impurity level is indicated by a thick (blue) solid line 59
- Figure 5.2: (a) Local minimum and (b) (fourfold-coordinated) local maximum configurations of a single atom vacancy; C-C bond lengths indicated are given in Å. In the inset, the unpaired and paired electrons are represented by maximally-localized Wannier functions (with an isosurface value of 0.95 electron/Å³), which were calculated using the CPMD package 61

Figure 5.3: Density of states projected onto the s , p_x , p_y and p_z states of the three C atoms surrounding the vacancy site; (a) without and (c) with H termination of the unsaturated sp^2 dangling bond. The shaded grey area represents the p_z states, and the red, blue, and green solid lines indicate the p_x , p_y , and s states, respectively. Band-decomposed charge densities near the Fermi level (E_F) are also plotted with an isosurface value of $0.04 \text{ electron}/\text{\AA}^3$ (based on the total density of states, not shown); (a) $-0.50 \text{ eV} < E - E_F < -0.30 \text{ eV}$ (mainly corresponding to the sp^2 dangling bond state) and $-0.20 \text{ eV} < E - E_F < 0 \text{ eV}$ (mainly the p_z states due to vacancy creation) and (c) $-0.15 \text{ eV} < E - E_F < 0 \text{ eV}$. (b) Spin density difference between the majority (spin up) and minority (spin down) states in (a) [$= \rho(\uparrow) - \rho(\downarrow)$]; the black (red) and grey (yellow) colors indicate the regions with excess majority and minority spin electrons, respectively. The isosurface value is set to $0.02 \text{ electron}/\text{\AA}^3$ 62

Figure 5.4: Optimized configurations of a BV pair for (a) twofold B and (b) fourfold B states. Grey and black (blue) balls represent C and B atoms, respectively, and the bond lengths indicated are given in \AA . The bonding interactions between the B and neighboring C atoms are also represented by maximally-localized Wannier functions (with an isosurface value of $0.95 \text{ electron}/\text{\AA}^3$) (right panels). Insets in (b) show the side views of the fourfold-state configurations; small black (red) balls represent Wannier Function Centers (WFCs). 63

Figure 5.5: Density of states projected onto the s , p_x , p_y and p_z states of the B and nearest C atoms for (a) twofold B and (b) fourfold B states. The shaded grey area represents the p_z states, and the red, blue, and green solid lines indicate the p_x , p_y , and s states, respectively. Band-decomposed charge densities for selected states (as indicated) are also plotted with an isosurface value of $0.09 \text{ electron}/\text{\AA}^3$ (based on the total density of states, not shown). Inset in (a) shows the difference between the majority (up) and minority (down) spin states [$= \rho(\uparrow) - \rho(\downarrow)$] near the Fermi level; the black (red) and grey (yellow) colors indicate the regions with excess majority and minority spin electrons, respectively. The isosurface value is set to $0.03 \text{ electron}/\text{\AA}^3$ 65

Figure 5.6: Energy variation (in eV) in terms of vacancy location with respect to B, together with corresponding atomic configurations. For the BV pair, 1* refers to the fourfold B state [Fig. 5.4(b)] while 1 and 1' represent the twofold state [Fig. 5.4(a)]. The bond lengths indicated are given in \AA 67

- Figure 5.7: Minimum energy configurations of (a) BV_2 and (b) V_2 . The bond lengths indicated are given in Å 69
- Figure 6.1: Model CNT system employed in electronic transport calculations, consisting of a central scattering region and two semi-infinite electrodes (shaded in grey). Impurities and defects are placed at the center of the scattering region; shown here is a (5,5) CNT with a substitutional boron (in blue)..... 73
- Figure 6.2: Fully relaxed configurations for substitutional B [(a); B_s] and single V with a weak C-C bond along the axial [(b); V_d] and the diagonal [(c); V_d] direction in (5,5) CNT; Each background lattice (in light grey) represents the pristine (5,5) CNT, for comparison. White and black (blue) balls represent C and B atoms, respectively..... 74
- Figure 6.3: Fully relaxed configurations for a B-V pair in different minimum-energy configurations. (Upper panels) a single V is located at $C1$ [in Fig. 6.2(a)]; the B atom could be twofold [(a), $B_s(Di)-V_d$], threefold [(b), $B_s(Tr)-V_d$], or fourfold [(c), $B_s(Te)-V_d$] coordinated. (Lower panels) a single V is located at $C2$ [in Fig. 6.2(a)]; the B atom could be twofold [(d), $B_s(Di)-V_d$] or fourfold [(e), $B_s(Te)-V_d$] coordinated. Each background lattice (in light grey) represents a (5,5) CNT with substitutional B. White and black (blue) balls represent C and B atoms, respectively..... 77
- Figure 6.4: (a) Relative formation energies (E_f) with respect to substitutional B for single V and B_s -V pair in different configurations (refers to Figs. 6.2 and 6.3 for the V and B-V labels) and (b) binding energies (ΔE) for $B_s(Te)-V_d$ with respect to fully separated B_s and V_d , as a functions of tube size [(n,n) = tube index, D = diameter] 81
- Figure 6.5: (a) Calculated spin-polarized conductance and (b) total DOS for (5,5) CNT with a B_s . Here, the spin-up and spin-down states are degenerate. The inset [in (b)] shows the band-decomposed charge density (with isosurface value of 0.003) within $-1.22 \text{ eV} < E - E_F < -0.74 \text{ eV}$ (shaded in grey), responsible for the corresponding broad dip as shown in (a); C and B atoms are indicated by grey and black (blue) balls, respectively. For comparison, the conductance and total DOS of pristine (5,5) CNT are also presented as broken lines..... 83

- Figure 6.6: (a) Calculated spin-polarized conductance and (b) total DOS of (5,5) CNT with a V_d . The black and grey solid lines indicate the majority (spin-up) and minority (spin-down) states, respectively. The insets [in (b)] show the band-decomposed charge density (for the majority state with isosurface value of 0.003) within $-1.26\text{eV} < E - E_F < -1.07\text{eV}$ and $-0.50\text{ eV} < E - E_F < 0.17\text{eV}$ (shaded in grey), causing the corresponding narrow and broad conductance dips [(a)]. For comparison, the conductance and total DOS of pristine (5,5) CNT are also presented as broken lines..... 85
- Figure 6.7: (a) Calculated spin-polarized conductance and (b) total DOS of (5,5) CNT with a B-V in the $B_s(Te)-V_d$ configuration. Here, the spin-up and spin-down states are degenerate. The insets [in (b)] show the band-decomposed charge density (with isosurface value of 0.003) within $-1.08\text{eV} < E - E_F < -0.69\text{eV}$ and $1.05\text{eV} < E - E_F < 1.13\text{eV}$ (shaded in grey), causing the corresponding broad and narrow conductance dips [(a)]; C and B atoms are indicated by grey and black (blue) balls, respectively. For comparison, the conductance and total DOS of pristine (5,5) CNT are also presented as broken lines..... 86
- Figure 7.1: Optimized configurations of (a) silylene site (SS), (b) dioxasilirane group (DOSG), and (c) DOSG/graphene (DOSG/Gr) determined using SLAB B (left panels) and model clusters (right panels). The inset in (b) shows a HOOH molecule for comparison. Wireframe represents bulk Si and O atoms in the α -SiO₂ lattice. The lone electron pair in SS [(a)], the O-O bonds in DOSG and HOOH [(b)], and the C-C bond in DOSG/Gr [(c)] are represented by the maximally-localized Wannier functions, which were calculated using the CPMD package. The isosurface values in (a), (b), and (c) are 0.70, 1.94, and 1.40 electron/Å³, respectively. The yellow (light grey), red (dark grey), white (white), and grey balls represent Si, O, H, and C, respectively, as also indicated. 94
- Figure 7.2: (a) Predicted reaction pathway for DOSG binding to graphene and (b) energy variation (in eV) along the reaction coordination from cluster DFT-GGA (PW91) calculations. The selected bond distances are given in Å, and the electronic charges of two terminal O atoms in DOSG are indicated in parenthesis. The yellow(light grey), red(dark grey), white, and grey balls represent Si, O, H, and C, respectively. 96

- Figure 7.3: (Left panels) Electronic density of states (DOS) and (right panes) isosurfaces of decomposed charge densities corresponding to $E_F - 1 \text{ eV} < E < E_F$ (hatched area) for (a) structure (A), (b) structure (B), and (c) structure (E) in Fig. 7.2. The isosurface value is set to $0.02 \text{ electron}/\text{\AA}^3$. Partial DOS projected on O_2 in DOSG is also presented in the inset of (a), demonstrating that the lowest unoccupied state, $\sigma^*(\text{O-O})$, is located just above the Fermi level of the DOSG + Graphene system. The vertical dotted line indicates the Fermi level position. The grey area represents p_z orbital and the solid (red and blue) lines indicate p_x and p_y orbitals, respectively. The sp^3 C atoms (bonded to DOSG) in graphene are represented by grey balls (also indicated by arrows), while the remaining sp^2 C atoms are by wireframe. 97
- Figure 8.1: Tetragonal scheelite in (a) shows BiO_8 dodecahedra (in purple) and VO_4 tetrahedra (in gray) with a, b, and c axis. Conventional unit cell of (b) tetragonal and (c) monoclinic scheelite BiVO_4 . Directions of cation displacement in $ms\text{-BiVO}_4$ are indicated by arrows in (c). Purple, silver, and red balls represent Bi, V, and O atoms, respectively. All Bi-O bonds are omitted for clarity 103
- Figure 8.2: The total energy of BiVO_4 (in eV per a primitive unit cell) as a function of the volume (in \AA^3) from (a) PBE, (b) HF10%, (c) HF25%, and (d) HF50% calculations. Two phases, $ts\text{-BiVO}_4$ (blue symbols) and $ms\text{-BiVO}_4$ (red symbols), are considered for each case. 107
- Figure 8.3: Charge density difference ($\Delta\rho = \rho^{\text{HF50}} - \rho^{\text{PBE}}$) isosurfaces ($\pm 0.022e/\text{\AA}^3$) of (a) $ts\text{-BiVO}_4$ and (b) $ms\text{-BiVO}_4$. Yellow (blue) regions corresponds to an positive $\Delta\rho$ (negative $\Delta\rho$). Purple, silver, and red balls represent Bi, V, and O atoms, respectively. All Bi-O bonds are omitted for clarity 110
- Figure 8.4: Density of states projected onto the Bi 6s (shaded in gray) and Bi 6p (red solid line) states of $ts\text{-BiVO}_4$, from (a) PBE, (b) HF25%, and (c) HF50% calculations. In the insets, the blue and green solid lines indicated the O 2p and V 3d states, respectively. The energy zero is set at the top of the valence band and dotted line indicates the Fermi energy (E_F). The right panel [in (c)] show the band-decomposed charge density (with isosurface value of $0.06 \text{ e}/\text{\AA}^3$) within $-1.40 \text{ eV} < E - E_F < 0 \text{ eV}$. Purple, silver, and red balls represent Bi, V, and O atoms, respectively. All Bi-O bonds are omitted for clarity. 112

- Figure 8.5: Density of states projected onto the Bi 6s (shaded in gray) and Bi 6p (red solid line) states of *ms*-BiVO₄, from (a) HF25% and (c) HF50% calculations. In the insets, the blue and green solid lines indicated the O 2p and V 3d states, respectively. The energy zero is set at the top of the valence band and dotted line indicates the Fermi energy (E_F). The right panel [in (b)] show the band-decomposed charge density (with isosurface value of $0.06 e/\text{\AA}^3$) within $-1.40 \text{ eV} < E-E_F < 0 \text{ eV}$. Purple, silver, and red balls represent Bi, V, and O atoms, respectively. All Bi-O bonds are omitted for clarity. 114
- Figure 8.6: Electronic band structure for (a) *ts*-BiVO₄ and (b) *ms*-BiVO₄ from HF25% calculation and (c) Brillouin zone for a body-centered tetragonal crystal structure. The energy zero is set at the top of the valence band. The bands are plotted along the Σ (to the Γ point) and Δ direction (from the Γ point). The values of direct and indirect band gap are also indicated. 116
- Figure 9.1: Total density of states (DOS) (left panels) and isosurfaces ($0.007 \text{ electron}/\text{\AA}^3$) of band-decomposed excess electron densities (right panels) of (a) delocalized and (b) small polaronic hole state in *ts*-BiVO₄. In the DOS plots, the red, blue, and green solid lines indicate the *s*, *p*, and *d* states, respectively. The energy zero is set at the top of the valence band and the dotted line indicates the Fermi energy. In the right panels, purple, silver, and red balls represent Bi, V, and O atoms, respectively. All Bi-O bonds are omitted for clarity 121
- Figure 9.2: Total density of states (DOS) (left panels) and isosurfaces ($0.004 \text{ electron}/\text{\AA}^3$) of band-decomposed excess electron densities (right panels) of (a) delocalized and (b) large polaronic hole state in *ms*-BiVO₄. In the DOS plots, the red, blue, and green solid lines indicate the *s*, *p*, and *d* states, respectively. The energy zero is set at the top of the valence band and the dotted line indicates the Fermi energy. In the right panels, purple, silver, and red balls represent Bi, V, and O atoms, respectively. All Bi-O bonds are omitted for clarity. 123
- Figure 9.3: Predicted migration pathway for small polaronic hole in *ts*-BiVO₄ (left panel) and potential energy surfaces of the initial [$E(\text{Bi}_A)$] and final state [$E(\text{Bi}_B)$] (right panel). Purple, silver, and red balls represent Bi, V, and O atoms, respectively. All Bi-O bonds are omitted for clarity. 125

- Figure 9.4: Total density of states (DOS) (left panels) and isosurfaces (0.008 electron/Å³) of band-decomposed excess electron densities (right panels) of (a) delocalized and (b) small polaronic electron state in *ts*-BiVO₄. In the DOS plots, the red, blue, and green solid lines indicate the *s*, *p*, and *d* states, respectively. The energy zero is set at the top of the valence band and the dotted line indicates the Fermi energy. In the right panels, purple, silver, and red balls represent Bi, V, and O atoms, respectively. All Bi-O bonds are omitted for clarity..... 127
- Figure 9.5: Total density of states (DOS) (left panels) and isosurfaces (0.008 electron/Å³) of band-decomposed excess electron densities (right panels) of (a) delocalized and (b) small polaronic electron state in *ms*-BiVO₄. In the DOS plots, the red, blue, and green solid lines indicate the *s*, *p*, and *d* states, respectively. The energy zero is set at the top of the valence band and the dotted line indicates the Fermi energy. In the right panels, purple, silver, and red balls represent Bi, V, and O atoms, respectively. All Bi-O bonds are omitted for clarity..... 129
- Figure 9.6: Predicted migration pathway for small polaronic electron in *ts*-BiVO₄ and *ms*-BiVO₄ (left panel) and potential energy surfaces of the initial [E(V_A)] and final state [E(V_B)] (right panel). Purple, silver, and red balls represent Bi, V, and O atoms, respectively. All Bi-O bonds are omitted for clarity..... 131

Chapter 1: Introduction

“Although the history of many new materials begins with a push towards purity, the effort to introduce impurities can start soon afterwards.”^[1] The optical and electrical properties of semiconductor materials can be greatly altered by incorporation of impurities and/or defects that alter the electronic structure. For instance, the photocatalytic performance of oxide semiconductors for water splitting has been found to be significantly altered by impurity doping, as the presence of dopants may affect the formation and transport of photogenerated electron-hole pairs.^[2] Impurities and defects may also play an important role in the fabrication and operation of electronic devices; for instance, defect-dopant complexes created during implantation are known to significantly affect the electrical activation and dopant concentration profiles in ultrashallow junction formation.^[3]

Due to its technical importance and scientific interest, there have been significant efforts to better understand the nature and behavior of defects and impurities in semiconductors, oxides, and their interfaces, yet many fundamental aspects are still ambiguous due largely to the difficulty of direct characterization.

My Ph.D. thesis work focuses on developing a better understanding of the nature and behavior of defects and impurities in semiconductors (Si, C, oxide semiconductors) and near their interfaces using first principles quantum mechanical calculations. This dissertation presents a partial of the thesis work.

Chapter 3 presents first principles calculations to understand the underlying mechanism of transient enhance diffusion (TED) of implanted arsenic (As) dopants during post-implantation annealing. In the study, we focused on silicon interstitial (I) mediated As diffusion, such as AsI, As₂I, AsI₂, and As₂I₂. The formation, dissociation,

and diffusion of probable AsI complexes were thoroughly examined to understand their relative contribution to As TED. This study suggests that AsI and AsI₂ play a major role in determining As diffusion profiles.

Chapter 4 presents some fundamental features related to plasma-assisted oxide nitridation. Our calculations show that N₂ molecules can be interstitially trapped in the amorphous silica matrix, and further reacts with O₂ molecules (in assistance with oxygen vacancy-related defects) and form N₂O molecules during high temperature O₂ post annealing. The newly formed N₂O species may diffuse to the Si/SiO₂ interface, and contribute to additional Si nitridation. Our findings support the experimental observation of anomalous interface nitridation.

Chapter 5, based on first principles calculations, presents how mobile single vacancies interact with substitutional boron in graphene as well as modifications in the electronic structure of graphene by the formation of boron-vacancy (BV) pairs as compared to substitutional B and single vacancy cases. We find that B in a BV pair favors fourfold-coordination, rather than remaining twofold coordinated, by forming a distorted tetrahedral structure with neighboring lattice carbon atoms. In the fourfold state, the B-V binding energy is predicted to be 2.4 eV. Our calculations also suggest possible magnetic moment oscillations induced by interconversion between the twofold (1 μ_B) and fourfold (0 μ_B) states, as the energy difference between them is rather moderate (≈ 0.3 eV). The influence of BV pairing on the electronic structure of graphene is also discussed. We finally calculate variations in the energetics and barriers of vacancy migration in the vicinity of boron; the results suggest that boron is likely to trap mobile vacancies within a certain radius and can possibly serve as an anchor for vacancy clusters.

Chapter 6, based on density-functional theory (DFT) calculations we present the interaction between a single vacancy (V) and a substitutional boron atom (B) in armchair carbon nanotubes (CNTs) with different tube diameters. We also employed the nonequilibrium Green's function (NEGF) method with DFT to examine how the boron-vacancy (B-V) pairing modifies the electronic transport properties of CNTs, as compared to the isolated V and B cases. Our calculations show that the B atom in a B-V pair energetically prefers to remain fourfold coordinated by passivating the vacancy dangling bonds. The energy gain due to B-V pairing increases with tube diameter; it is predicted to be about 1.6 eV for an armchair (5,5) tube and increases up to 2.5 eV in flat graphene. From DFT-NEGF calculations of spin-polarized conductance in CNTs, we find that the tube conductance with a B-V pair exhibits similarity to the B case while most of the vacancy features likely disappear.

Chapter 7 presents a possible mechanism for defect-assisted covalent binding of graphene to the surface of amorphous silica (α -SiO₂) based on first principles density functional calculations. Our calculations show that a dioxasilirane group (DOSG) on α -SiO₂ may react with graphene to form two Si-O-C linkages with a moderate activation barrier (\approx 0.3 eV) and considerable exothermicity (\approx 1.0 eV). This suggests that graphene can be strongly bound to the chemically modified α -SiO₂ surface. We also examined DOSG formation via the adduction of molecular O₂ to a silylene center which is a prevailing surface defect in α -SiO₂, and briefly discuss possible modifications in the electronic structure of graphene upon the DOSG-assisted chemical binding onto the α -SiO₂ surface.

Lastly, in Chapters 8 and 9, the thesis work focuses on examining the performance characteristics of oxide semiconductors, particularly bismuth vanadate (BiVO₄), for solar-powered photoelectrochemical (PEC) production of H₂ through hybrid

DFT calculations. BiVO_4 has received much interest as a promising visible-light-active photocatalyst for O_2 evolution in aqueous solutions. However, its photocatalytic performance suffers from poor electrical conductivity, especially due to low electron mobility that may cause undesirable recombination of photogenerated electron-hole ($e-h$) pairs.^[4,5] Thus, it is important to accurately describe the transport of excess charges (e and h) that greatly affects the photocatalytic performance. First, we use hybrid DFT method to determine the structural properties of BiVO_4 , including monoclinic and tetragonal scheelite phases; our study shows that conventional DFT is likely inadequate to describe the monoclinic-to-tetragonal phase transformation associated with stereochemically active Bi $6s^2$ lone pair formation. Our hybrid DFT calculations have successfully described the formation and transport of excess charge carriers in both monoclinic and tetragonal structures of BiVO_4 . The calculation results explain well existing experimental observations and also predict the doping effect on the enhanced photocatalytic performance of BiVO_4 ; the theoretical prediction has been validated by recent experiments. The improved understanding regarding excess charge carriers provides invaluable guidance to the modification of existing photocatalysts and the rational design of new materials for high-efficiency solar-powered hydrogen generation.

Chapter 2: Theoretical Backgrounds

2.1 HARTREE-FOCK THEORY

In a many-body system, the Schrödinger equation must be solved for the N-electron wavefunction $\Psi(\mathbf{R}_1, \mathbf{R}_2, \dots; \mathbf{r}_1, \mathbf{r}_2, \dots)$:

$$\hat{H} \cdot \Psi(\mathbf{R}_1, \mathbf{R}_2, \dots; \mathbf{r}_1, \mathbf{r}_2, \dots) = E \cdot \Psi(\mathbf{R}_1, \mathbf{R}_2, \dots; \mathbf{r}_1, \mathbf{r}_2, \dots) \quad (2.1.1)$$

Where $\{\mathbf{R}_I\}$ and $\{\mathbf{r}_i\}$ are used for the nuclear and electronic coordinates, respectively, and the spin has been omitted for simplicity. The Hamiltonian consists of kinetic energy operator \hat{T} and potential operator \hat{V} :

$$\hat{H} = \hat{T} + \hat{V} \quad (2.1.2)$$

$$\hat{T} = \sum_I -\frac{\hbar^2}{2M_I} \nabla_I^2 - \sum_i -\frac{\hbar^2}{2m_e} \nabla_i^2 \quad (2.1.3)$$

Using Born-Oppenheimer approximation^[6,7], the first term in Eq. (2.1.3) can be ignored.

The potential operator part is written as

$$\hat{V} = \frac{1}{2} \sum_{ij(i \neq j)} \frac{e^2}{|\mathbf{r}_i - \mathbf{r}_j|} - \sum_{iI} \frac{Z_I e^2}{|\mathbf{R}_I - \mathbf{r}_i|} + \frac{1}{2} \sum_{IJ(I \neq J)} \frac{Z_I Z_J e^2}{|\mathbf{R}_I - \mathbf{R}_J|} \quad (2.1.4)$$

Using Eq. (2.1.3) and (2.1.4), the electronic part of total Hamiltonian can be described by

$$\begin{aligned} \hat{H} = \hat{T} + \hat{V} &= -\sum_i -\frac{\hbar^2}{2m_e} \nabla_i^2 - \sum_{iI} \frac{Z_I e^2}{|\mathbf{R}_I - \mathbf{r}_i|} + \frac{1}{2} \sum_{ij(i \neq j)} \frac{e^2}{|\mathbf{r}_i - \mathbf{r}_j|} \\ &= -\sum_i -\frac{\hbar^2}{2m_e} \nabla_i^2 + \sum_i V_{ion}(\mathbf{r}_i) + \frac{e^2}{2} \sum_{ij(i \neq j)} \frac{1}{|\mathbf{r}_i - \mathbf{r}_j|} \end{aligned} \quad (2.1.5)$$

The first term in Eq. (2.1.5) is for the kinetic energy operator of the many-body system and the second term represents the interaction of electrons with the fixed nuclei. The last term in Eq. (2.1.5) represents the classical Coulomb interactions between the electrons. In the Hartree approximation^[7], the many-body wavefunction is written as a product of non-interacting single particle wavefunctions.

$$\Psi^H(\mathbf{r}_1, \mathbf{r}_2, \dots, \mathbf{r}_N) = \varphi_1(\mathbf{r}_1)\varphi_2(\mathbf{r}_2)\cdots\varphi_N(\mathbf{r}_N) \quad (2.1.6)$$

Thus, the total Hartree energy becomes

$$\begin{aligned} E^H &= \langle \Psi^H | \hat{H} | \Psi^H \rangle \\ &= \sum_i \langle \varphi_i | -\frac{\hbar^2}{2m_e} \nabla_i^2 + V_{ion}(\mathbf{r}) | \varphi_i \rangle + \frac{e^2}{2} \sum_{ij(i \neq j)} \langle \varphi_i \varphi_j | \frac{1}{|\mathbf{r}-\mathbf{r}'|} | \varphi_i \varphi_j \rangle \end{aligned} \quad (2.1.7)$$

In order to find the single particle wavefunctions φ_i , the variational method is applied to Eq. (2.1.7), which leads to the following single particle Hartree equation:

$$\left[-\frac{\hbar^2}{2m_e} \nabla_i^2 + V_{ion}(\mathbf{r}) + e^2 \sum_{j(j \neq i)} \langle \varphi_j | \frac{1}{|\mathbf{r}-\mathbf{r}'|} | \varphi_j \rangle \right] \varphi_i(\mathbf{r}) = \varepsilon_i \varphi_i(\mathbf{r}) \quad (2.1.8)$$

Since the third term in the Hamiltonian of Eq. (2.1.8), $e^2 \sum_{j(j \neq i)} \langle \varphi_j | \frac{1}{|\mathbf{r}-\mathbf{r}'|} | \varphi_j \rangle$, is orbitally dependent and φ_i can be only solved if all the other φ_j are known, it is hard to solve the Hartree equation directly. Thus, the self-consistent field approximation is used to solve this equation. The Hartree equation, however, fails to recognize that no two electrons can have the same quantum number. To obey the Pauli Exclusion Principle, the wavefunction should be anti-symmetric under the interchange of two electrons. In order to be compatible with the Pauli principle, the N-body wavefunction is written as a Slater determinant. The result is the so-called Hartree-Fock equation:

$$-\frac{\hbar^2}{2m_e} \nabla_i^2 \varphi_i(\mathbf{r}) + V_{ion}(\mathbf{r}) \varphi_i(\mathbf{r}) + e^2 \left[\sum_{j(j \neq i)} \int \frac{|\varphi_j(\mathbf{r}')|^2}{|\mathbf{r}-\mathbf{r}'|} d\mathbf{r}' \right] \varphi_i(\mathbf{r}) - \sum_{j(j \neq i)} \int \frac{d\mathbf{r}'}{|\mathbf{r}-\mathbf{r}'|} \varphi_j^*(\mathbf{r}') \varphi_i(\mathbf{r}') \varphi_j(\mathbf{r}) \varphi_i^*(\mathbf{r}) = \varepsilon_i(\mathbf{r}) \quad (2.1.9)$$

The last term of Eq. (2.1.9) on the left hand side is the exchange term. This exchange term represents a first order approximation to the total energy due to many body

interactions. Despite including the exchange term, the Hartree-Fock equation still does poorly for many properties. Later, Post Hartree-Fock methods include other approximations for electron correlation in order to represent many body interactions more accurately. The Hartree-Fock equation is an earlier approach to many-body systems, and next I will introduce another approach to solve the many-body problem.

2.2 KOHN-SHAM THEORY

Density Functional Theory (DFT) methods are based on the Hohenberg-Kohn theorem^[8] which states that the ground state electron density $\rho(\mathbf{r})$ of a structure uniquely determines the ground state electronic energy of the system. A ‘functional’ takes a function as an input and gives a number as an output. For DFT, the density $\rho(\mathbf{r})$ is an input, while the ground state energy is an output; that is, the ground state energy can be viewed as a functional of the ground state density $\rho(\mathbf{r})$. The Hohenberg-Kohn theorem can be applied to any system of interacting particles in an external potential, with the following Hamiltonian:

$$\hat{H} = -\frac{\hbar^2}{2m_e} \sum \nabla_i^2 + \frac{1}{2} \sum_{ij(i \neq j)} \frac{e^2}{|\mathbf{r}_i - \mathbf{r}_j|} + \sum_i V_{ext}(\mathbf{r}_i) \quad (2.2.1)$$

The electronic energy E is expressed as:

$$E[\rho(\mathbf{r})] = T[\rho(\mathbf{r})] + E_{int}[\rho(\mathbf{r})] + \int V_{ext}(\mathbf{r})\rho(\mathbf{r})d\mathbf{r} + E_{II} \quad (2.2.2)$$

Where $T[\rho(\mathbf{r})]$ is the kinetic energy of the interacting electron system, $E_{int}[\rho(\mathbf{r})]$ is the Coulomb potential energy between electrons, $\int V_{ext}(\mathbf{r})\rho(\mathbf{r})d\mathbf{r}$ represents electron-nuclear Coulomb potential energy (for the fixed atomic nuclei), and E_{II} is the interaction energy between the nuclei at the fixed position.^[9] Although the Hohenberg-Kohn theorems reformulated the many-body problem in terms of density [see Eq. (2.2.2)], there is no analytical expression for $T[\rho(\mathbf{r})]$ or $E_{int}[\rho(\mathbf{r})]$ of the interacting electron system.

Since the Hohenberg-Kohn theorems consider the many-body interacting electron problem without any approximation, the theory is exact in principal, but impractical and unrealistic for dealing with real systems for any useful purposes.

In 1965, Kohn and Sham showed that it is possible to replace the original many body problem in the interacting electron system with exactly equivalent set of non-interacting single electron equations.^[10] Figure 2.1 describes the concept of the Kohn-Sham theorem.

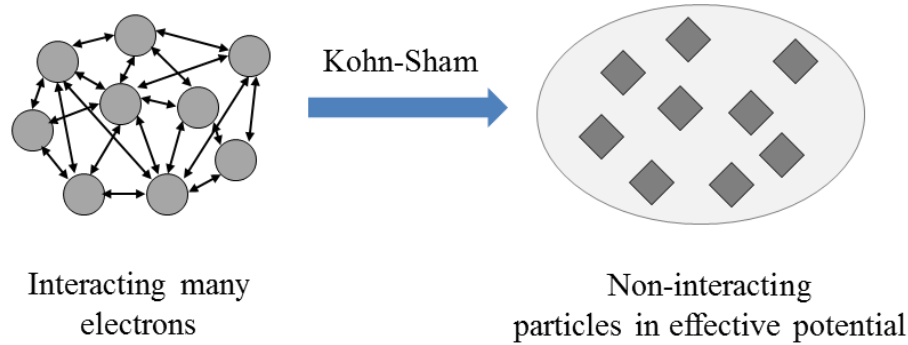


Figure 2.1 Kohn-Sham diagram.

In Eq. (2.2.2), the first term on the right hand side $T[\rho(\mathbf{r})]$ is the kinetic energy of interacting electrons. This $T[\rho(\mathbf{r})]$ can be decomposed into two parts, $T_s[\rho(\mathbf{r})]$ and $E_c[\rho(\mathbf{r})]$, in the Kohn-Sham equation [in Eq. (2.2.3)]. $T_s[\rho(\mathbf{r})]$ is the kinetic energy of independent electrons and $E_c[\rho(\mathbf{r})]$ accounts for the effect of many body interactions; that is, the latter deals with the repulsive coulombic forces between moving and interacting electrons. The second term in Eq. (2.2.2), $E_{\text{int}}[\rho(\mathbf{r})]$, is the internal energies between electrons of the actual many-body system. This can be expressed by the sum of $E_{\text{Hartree}}[\rho(\mathbf{r})]$ and $E_{\text{xc}}[\rho(\mathbf{r})]$ [in Eq. (2.2.3)]; the former $E_{\text{Hartree}}[\rho(\mathbf{r})]$ is the interaction energy between independent electrons and can be treated as a classical

Coulomb interaction, while the remaining energy due to interacting electrons is included in the $E_{xc}[\rho(\mathbf{r})]$. So, the total electronic energy of the Kohn-Sham equation is written as:

$$\begin{aligned}
E_{KS}[\rho(\mathbf{r})] &= T_s[\rho(\mathbf{r})] + E_{Hartree}[\rho(\mathbf{r})] + (T[\rho(\mathbf{r})] - T_s[\rho(\mathbf{r})] + E_{int}[\rho(\mathbf{r})] - E_{Hartree}[\rho(\mathbf{r})]) \\
&\quad + \int V_{ext}(\mathbf{r})\rho(\mathbf{r})d\mathbf{r} + E_{II} \\
&= T_s[\rho(\mathbf{r})] + E_{Hartree}[\rho(\mathbf{r})] + E_{xc}[\rho(\mathbf{r})] + \int V_{ext}(\mathbf{r})\rho(\mathbf{r})d\mathbf{r} + E_{II}
\end{aligned} \tag{2.2.3}$$

Where, analytically $\rho(\mathbf{r}) = \sum_i |\Psi_i(\mathbf{r})|^2$, $T_s[\rho(\mathbf{r})] = -\frac{\hbar^2}{2m_e} \sum_i \int \Psi_i^*(\mathbf{r}) \nabla_i^2 \Psi_i(\mathbf{r}) d\mathbf{r}$ and $E_{Hartree}[\rho(\mathbf{r})] = \frac{1}{2} \int \frac{\rho(\mathbf{r})\rho(\mathbf{r}')}{|\mathbf{r}-\mathbf{r}'|} d\mathbf{r}d\mathbf{r}'$. As in Eq. (2.2.3), the many body effects in the real system are included in $E_{xc}[\rho(\mathbf{r})]$. Using proper approximations in E_{xc} , which will be explained in the next section, $E_{KS}[\rho(\mathbf{r})]$ is minimized by the following variational equation:

$$\frac{\delta E_{KS}[\rho(\mathbf{r})]}{\delta \rho(\mathbf{r})} = \left[\frac{T_s[\Psi_i(\mathbf{r})]}{\delta \Psi_i(\mathbf{r})} \right] \frac{\delta \Psi_i(\mathbf{r})}{\delta \rho(\mathbf{r})} + \frac{E_{Hartree}[\rho(\mathbf{r})]}{\delta \rho(\mathbf{r})} + \frac{E_{xc}[\rho(\mathbf{r})]}{\delta \rho(\mathbf{r})} + \frac{\int V_{ext}(\mathbf{r})\rho(\mathbf{r})d\mathbf{r}}{\delta \rho(\mathbf{r})} \tag{2.2.4}$$

subject to constraint $\langle \Psi_i | \Psi_j \rangle = \delta_{ij}$.^[9]

This minimization yields the Kohn-Sham equation as following:

$$\left[-\frac{\hbar^2}{2m_e} \nabla_i^2 + V_{Hartree}(\mathbf{r}) + V_{xc}(\mathbf{r}) + V_{ext}(\mathbf{r}) \right] \Psi_i(\mathbf{r}) = \varepsilon_i \Psi_i(\mathbf{r}) \tag{2.2.5}$$

In Eq. (2.2.5), the eigenfunction $\Psi_i(\mathbf{r})$ and the eigenvalue ε_i is the Kohn-Sham orbital and corresponding energy, respectively. Since $\rho(\mathbf{r}) = \sum_i |\Psi_i|^2$ and $V_{Hartree}(\mathbf{r})$, $V_{xc}(\mathbf{r})$ and $V_{ext}(\mathbf{r})$ are functions of density, the Kohn-Sham equation can be solved self-consistently.

The self-consistent Kohn-Sham equation solver is briefly described in Figure 2.2.

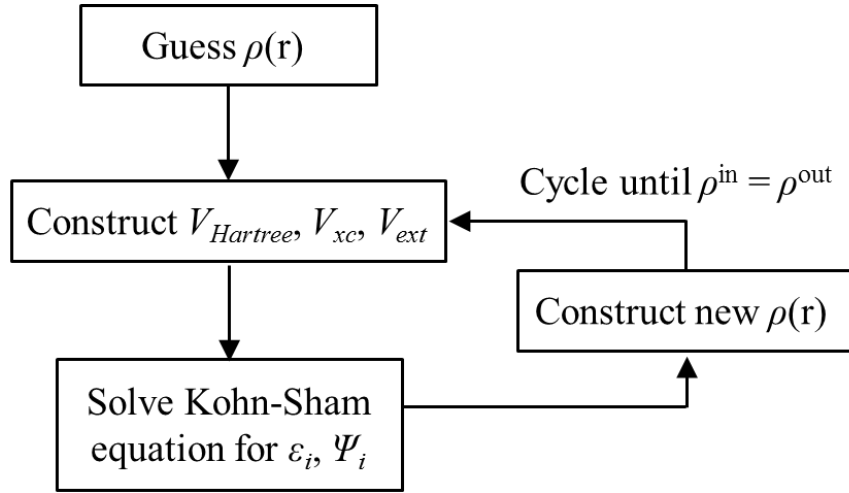


Figure 2.2 Self-consistent Kohn-Sham equation diagram

By introducing the exchange-correlation energy into the Hohenberg-Kohn theorem, Kohn and Sham treat the interacting electron system as the non-interacting and soluble particle system.

2.3 EXCHANGE-CORRELATION FUNCTIONAL

2.3.1 Local Density Approximation

In DFT calculation, a reasonable approximation of $E_{xc}[\rho(r)]$, which contains all many-body aspect, is important to calculate the total energy and other electronic properties. In 1965, Kohn and Sham introduced the local-density approximation (LDA) to exchange-correlation energy. The basic concept of the LDA is assuming that the electronic density at each point in space is the same as that of the homogenous electron gas. Thus, the $E_{xc}[\rho(r)]$ can be expressed in terms of exchange-correlation in the

homogenous electron gas. The exchange energy of the homogeneous electron gas is [11,12]

$$e_x^{hom}[\rho] = -\frac{3q^2}{4} \left(\frac{3}{\pi}\right)^{1/3} \rho^{4/3} \quad (2.3.1)$$

Thus, the LDA for E_x is written as,

$$E_x^{LDA}[\rho] = -\frac{3q^2}{4} \left(\frac{3}{\pi}\right)^{1/3} \int dr \rho(r)^{4/3} \quad (2.3.2)$$

However, the correlation energy of the homogeneous electron gas, $e_c^{hom}[\rho]$, is not known explicitly. In order to express $e_c^{hom}[\rho]$, Quantum Monte Carlo (QMC) methods are applied to the homogenous electron gas.^[13]

Concisely, the LDA for $E_{xc}[\rho]$ is

$$E_{xc}[\rho] \approx E_{xc}^{LDA}[\rho] = \int dr e_{xc}^{hom}[\rho]|_{\rho \rightarrow \rho(r)} = \int dr e_{xc}^{hom}[\rho(r)] \quad (2.3.3)$$

where $e_{xc}^{hom} = e_x^{hom} + e_c^{hom}$.^[14]

Since the real system is not the same as the homogenous electron gas, a huge discrepancy was expected in the LDA. Amazingly, however, this approximation for $E_{xc}[\rho(r)]$ has proved successful and been applied in many cases. The success of LDA can be attributed to the systematic error cancellation. Typically, E_x is underestimated by 10%, whereas this error is compensated by an overestimation of E_c by a factor of 2 or 3. Thus, the overall error is only 7% for E_{xc} . In the LDA, E_{xc} is the solution of a spatially homogeneous interacting electron gas and therefore, E_{xc} gives relatively good results for the system with slowly varying charge densities. However, it does not give accurate agreement with the exact exchange correlation energy and leads to considerable overbinding. Several attempts have been made to improve the LDA by taking into account the derivatives of electron density as well as the electron density itself. This refinement is called the Generalized Gradient Approximation (GGA).

2.3.2 Generalized Gradient Approximation

Comparing with the LDA, which is a local functional, the GGA is classified as a semi-local functional. Since the charge density $\rho(\mathbf{r})$ at point \mathbf{r} is spatially varying, it can be expected that E_{xc} is represented more accurately by including the varying rate of the electronic density in the exchange-correlation functional. The brief idea of the GGA is ^[15],

$$E_{xc}^{GGA}[\rho] = \int d\mathbf{r} f(\rho(\mathbf{r}), \nabla\rho(\mathbf{r})) \quad (2.3.4)$$

By including gradient of density, the GGA corrects the local limit of the LDA; the GGA increases exchange energy, while reducing the contribution of correlation energy. Thus, it predicts better electric properties, such as binding energy and transition state barrier, over the LDA. Depending on the choice of the functional $f(\rho(\mathbf{r}), \nabla\rho(\mathbf{r}))$ in Eq. (2.3.4), the GGAs have many different types. PW91 by Perdew and Wang in 1991 ^[16,17] was constructed by introducing a real space cutoff to the exchange and correlation hole of density gradient expansion approximation (GEA). It includes a large number of parameters, and in some cases, these parameters do not represent the exact features of the exchange-correlation energy. In order to address this weakness of the PW91, PBE (Perdew-Burke-Ernzerhof), the most popular GGA functional, was constructed with minor changes over the PW91 in 1996. ^[18,19] The PBE simplifies the derivation of PW91 and reduces the parameters if they are not either fundamental constants or ones given from the quantum mechanical relation. This functional works well in high and low density gradient constraints, although it has problems in intermediate density gradient stage. To improve this weak point, the Revised PBE (RPBE) functional was constructed, ^[20] which satisfies the boundary condition and provides a better description of molecules. Although the RPBE has been introduced to remedy the PBE, there are still larger disagreements with experimental results in some material properties compared

with the PBE calculations. Thus, choosing the appropriate exchange correlation functional is important to calculate the properties of materials.

2.4 ION POTENTIAL

In the Kohn-Sham equation [Eq. (2.2.5)], the external potential $V_{ext}(r)$ describes the interaction of electrons and fixed ions. Electrons are decomposed into two parts, core and valence electrons. Core electrons are localized near the nucleus with a strong Coulombic force and have rapidly oscillating wavefunctions. To describe wavefunction of core electrons using plane-waves, a large basis set is required. However, in most cases, only valence electrons are chemically important to determine electronic properties. For this reason, the external potential $V_{ext}(r)$, which is the interacting potential of all electrons and nucleus, can be simplified with fewer basis sets, which describe valence region (outside the atomic core) exactly but core region approximately.

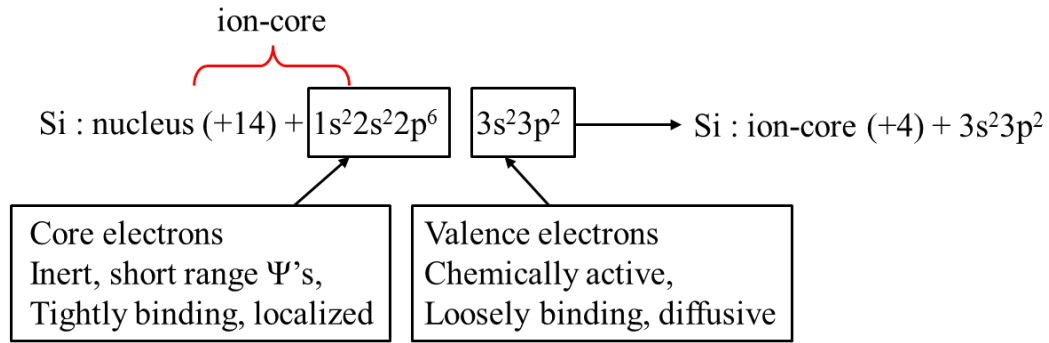


Figure 2.3 Analysis of a Si atom with core and valence electrons.

For example, a Si atom has fourteen protons and electrons ($1s^2 2s^2 2p^6 3s^2 3p^2$); among these electrons, the first ten ($1s^2 2s^2 2p^6$) are core electrons and last four ($3s^2 3p^2$) are valence electrons, and the ion-core is composed of a nucleus (+14) and ten core electrons (-10), as shown in the left hand side of Figure 2.3. So, the four chemically

active valence electrons can be seen as interacting with their own ion-core (+4) and all other ion-cores in the Si matrix.

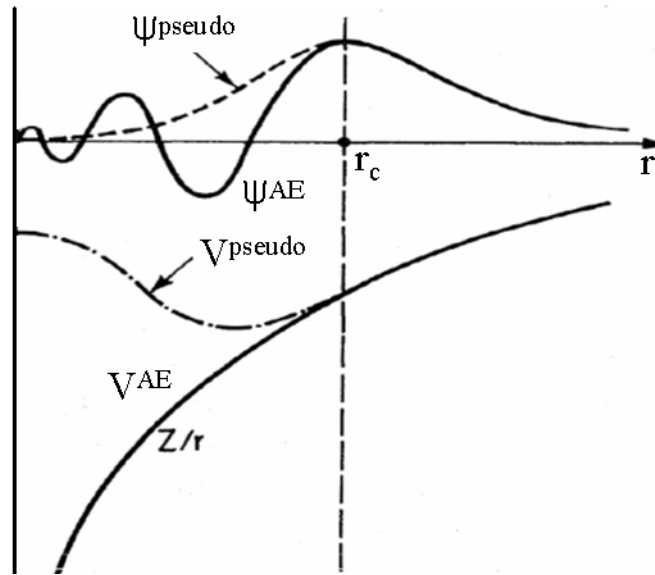


Figure 2.4 Comparison between pseudo and all-electron wavefunction and between pseudopotential and all-electronic potential.^[21]

As presented in Figure 2.4, outside the core region ($r > r_c$, radius cutoff r_c), the pseudo wavefunction ψ^{pseudo} is the same as the all-electron (AE) wavefunction ψ^{AE} , since the scattering properties should be described exactly in the valence region. Also, in the core region ($r < r_c$), the pseudopotential (PPT) is constructed not to have radial nodes in the pseudo wavefunction ψ^{pseudo} . With these basic constraints, there are several types of PPTs. Ab initio norm-conserving pseudopotential (NC PPT) gives an important step toward realistic and transferable PPTs, while previous empirical PPTs were based on parameters fit to reference data. Ab initio NC PPTs are generated from ab initio atomic calculations and there are several requirements to make reasonable ab initio NC PPTs.^[21,22]

1. All-electron (AE) and pseudo valence eigenvalues are identical: $\epsilon_v^{\text{pseudo}} = \epsilon_v^{\text{AE}}$
2. All-electron and pseudo valence wavefunctions agree outside the core region:

$$\psi_v^{\text{pseudo}} = \psi_v^{\text{AE}} \quad (r > r_c)$$
3. The integrated charge in the core region is the same (norm-conserving):

$$\int_0^{r_c} |\psi_v^{\text{AE}}|^2 dr = \int_0^{r_c} |\psi_v^{\text{pseudo}}|^2 dr$$
4. ψ_v^{pseudo} is continuous at $r = r_c$ as well as its logarithmic derivative:

$$\psi_v^{\text{pseudo}}(r_c) = \psi_v^{\text{AE}}(r_c) \quad , \quad \left[\frac{d}{dr} \ln \psi_v^{\text{pseudo}}(r) \right]_{r_c} = \left[\frac{d}{dr} \ln \psi_v^{\text{AE}}(r) \right]_{r_c}$$

NC PPTs have been constructed with these constraints from ab initio self-consistent AE calculations. Since the cutoff radius r_c is used as a dividing point of the core and valence regions, r_c can determine the hardness and softness of the pseudopotentials. Smaller values better match the AE case, but require a larger basis set (more computational cost). In contrast, a larger r_c gives less accurate results, but it makes smooth pseudopotentials and wavefunctions and thus, a relatively smaller basis set is required. However, due to norm conserving constraint, NC PPTs still require a large basis set. In order to reduce the size of basis set of plane waves further (corresponding to reduce the cutoff energy), ultra-soft Pseudo potentials (US PPTs) have been introduced.^[23,24] Instead of fulfilling norm-conserving conditions, charge augmentation term is used in US PPTs to normalize the final pseudo wavefunctions to correct the charge. The most commonly used US PPT (invented by Troullier and Martins^[25]) applies maximal smoothness to ψ^{pseudo} . Smoothing the pseudo wavefunction allows a choice of larger r_c with improved accuracy.

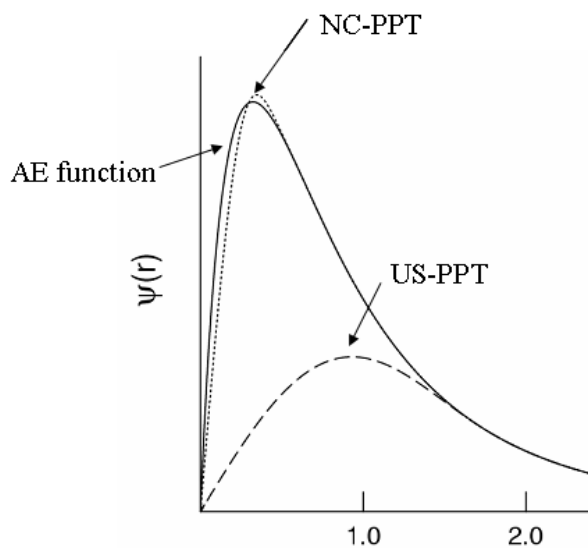


Figure 2.5 Oxygen 2p radial function with all-electron (AE) potential, norm-conserving pseudopotential (NC PPT), and ultrasoft pseudopotential (US PPT).^[23]

As shown in Figure 2.5, the NC pseudo wavefunction is accurate but has a hard curve and an overshoot due to norm conservation. On the other hand, the US pseudo wavefunction has a smooth curve and a larger r_c than the NC case, but it does not agree well with the AE wavefunction and is less accurate.

Chapter 3: Structure and Dynamics of Arsenic-Silicon Interstitial Complexes in Crystalline Silicon

3.1 INTRODUCTION

Scaling complementary metal oxide semiconductor (CMOS) devices beyond the 45-nm node may require the formation of highly doped ultrashallow junctions less than 7 nm deep with high lateral abruptness. To meet these stringent requirements, it is necessary to have a better understanding of the underlying mechanisms of transient enhanced diffusion (TED) of implanted dopants during post-implantation annealing. It is now well accepted that dopant diffusion is mainly mediated by native defects created in the substrate. Some early experimental studies suggested that arsenic (As) TED could be mediated by both interstitials and vacancies.^[26-30] While various mobile dopant-defect complexes have been identified by extensive first principles quantum mechanical calculations, their relative contribution to evolution of dopant diffusion profiles has not been clarified yet. In this chapter, we will focus on addressing the relative contribution of various As-interstitial complexes (AsI , AsI_2 , As_2I , and As_2I_2) to diffusion of As, based on extensive first principles calculations. We have found that AsI and AsI_2 are important diffusing species for As diffusion profiles. The pathways and barriers for their diffusion and dissociation will be presented. Based on the data, we will discuss how these mobile species determine dopant diffusion profiles.

3.2 CALCULATION METHODS

All atomic configurations and energies reported herein were calculated on the basis of density functional theory (DFT) within the generalized gradient approximation (GGA-PW91)^[31], as implemented in the Vienna *Ab-initio* Simulation Package (VASP).^[32]

A plane-wave basis set for valence electron states and Vanderbilt-type ultrasoft pseudopotentials^[23] for core-electron interactions were employed. An energy cutoff of 12 Ry (163.2 eV) was applied for the plane wave expansion of electronic eigenfunctions. A (2×2×2) *k*-point mesh generated based on the scheme of Monkhorst-Pack was used for the Brillouin zone sampling.^[33] In the calculations, 216-Si atom supercell with a fixed lattice constant of 5.457 Å was used as a model system. For defect configurations, the geometries were optimized using the conjugate gradient method until residual forces on constituent atoms became smaller than 5×10^{-2} eV/Å. The nudged elastic band method (NEBM) was used to determine the diffusion and dissociation barriers and pathways.^[34]

3.3 AsI

The structure, stability and diffusion of substitutional As-interstitial Si (AsI) pairs in the positive, neutral and negative charge states were determined by Hwang and coworkers using DFT-GGA calculations.^[35] In Fig. 3.1 (a), we present the atomic configurations of the AsI pairs. The relative formation energy of the neutral AsI complex is estimated to be 3.07 eV with respect to neutral substitutional As (As^0). Our DFT-GGA calculations also predict that the first acceptor and donor levels of the AsI pair are located 0.50 eV above the valence band maximum ($E_V + 0.50$ eV) and 0.47 eV below the conduction band minimum ($E_C - 0.47$ eV), respectively, within the computed Si bandgap of 0.63 eV. This suggests that the neutral pair will be dominant under intrinsic conditions, although uncertainty exists in the DFT computed ionization levels.

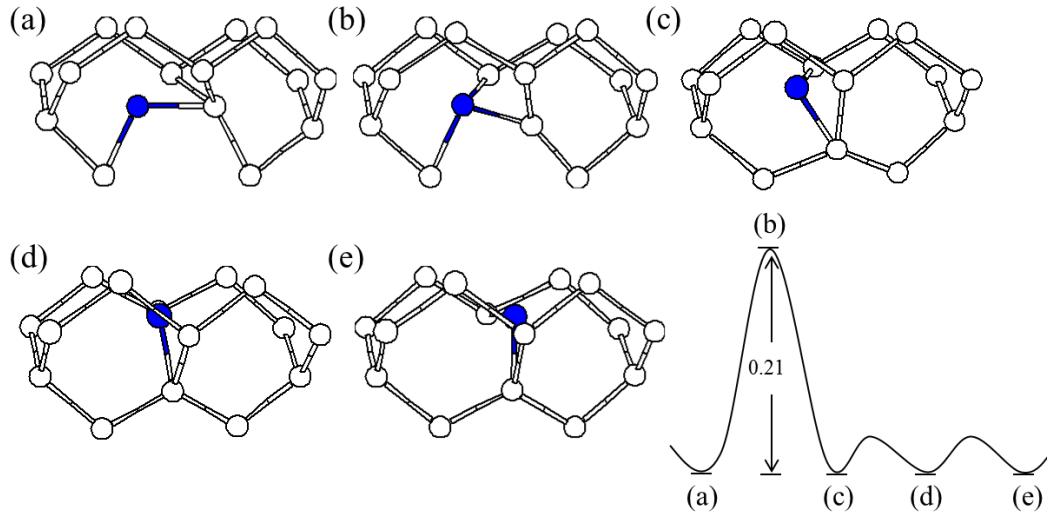


Figure 3.1 The diffusion pathway for AsI [(a)-(e)]. The corresponding energy pathway (in eV) is shown. The blue (dark-colored) and white ball represent As and Si atoms, respectively.

Fig. 3.1 shows the diffusion pathway and transition states for neutral AsI. The initial step involves As migration from one bridged site [(a)] to another [(c)] by breaking an As-Si bond and forming a new As-Si bond. The transition state [(b)] for this step was found to be 0.21 eV above the initial state [(a)]. The next two migration steps from (c) to (d) and (d) to (e) involve As reorientation within the same bridged site by overcoming negligible energy barriers (0.03 eV). Accordingly the overall activation energy for the AsI pair diffusion is estimated to be 0.21 eV.

Fig. 3.2 shows predicted dissociation pathways and barriers for neutral and positive AsI pairs. We paid special attention to AsI^+ dissociation ($\text{AsI}^+ \rightarrow \text{As}^+ + \text{I}$) since substitutional As as a shallow donor preferentially remains positively charged. The neutral and positive AsI pairs follow a nearly identical dissociation route. The first step [(a) \rightarrow (b)] involves that the Si interstitial is dislodged to an adjacent $\langle 110 \rangle$ -split site while the As atom moves to a substitutional site. In the second step [(b) \rightarrow (c)], the Si

interstitial undergoes further migration to a neighboring hexagonal site. The total energy of (c) is comparable to that of the fully separated substitutional As and <110>-split Si interstitial; since the formation energy of neutral Si interstitial at a hexagonal site is 3.83eV, only 0.09eV higher than that of ground state <110>-split configuration, it would be legitimate to consider As and I are fully separated in the (c) state. For the neutral (positive) pair, the (b) and (c) states are 0.53 (0.21) eV and 0.76 (0.34) eV above the lowest-energy state (a), while the first and second events require overcoming barriers of 0.92 (0.59) eV and 0.38 (0.38) eV, respectively. The pathway from (a) to (c) only represents dissociation in short range, and for the long range, the dissociation energy can simply be estimated by adding the binding energy of dissociation products and the migration barrier of a mobile species. Realistically, dissociation in both short and long ranges should be considered in determining the overall barrier.

For AsI^0 and AsI^+ , the sums of corresponding AsI binding energies and I migration barriers are 1.01 eV and 0.74 eV. Accounting the barriers of both short- and long-range dissociations, overall dissociation barriers for $\text{AsI}^0 (\rightarrow \text{As}^0 + \text{I})$ and $\text{AsI}^+ (\rightarrow \text{As}^+ + \text{I})$ are predicted to be 1.01 eV and 0.59 eV, respectively. The energy variations for AsI^0 and AsI^+ are combined as shown in Fig. 3.2 in reference to the formation energy difference (0.15 eV) found in neutral and positive states. Considering possible charge variations, $\text{AsI}^0 \rightarrow \text{As}^+ + \text{I}^0$ would be the more probable dissociation reaction by crossing a barrier of 0.74 eV under intrinsic conditions.

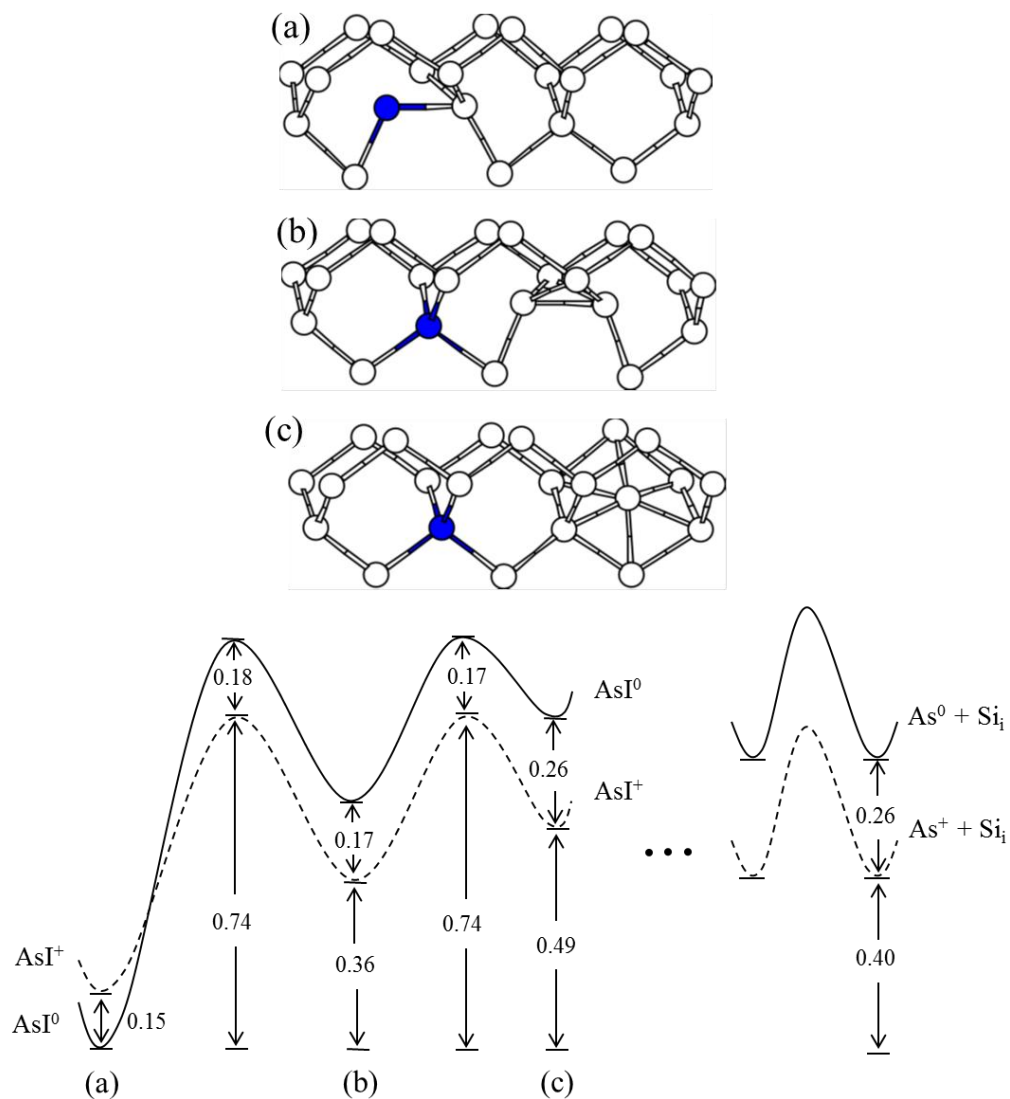


Figure 3.2 (Upper Panel) The pathway for AsI^0 and AsI^+ dissociation. The blue (dark-colored) and white ball represent As and Si atoms, respectively. (Lower Panel) Corresponding energy barriers (in eV) of AsI^0 (solid line) and AsI^+ (dashed line) dissociation.

3.4 As₂I

In Fig. 3.3 (a), we show the lowest-energy structure of As₂I with C_{2v} symmetry in which two As atoms share a lattice site while the As-As bond axis is slightly tilted from the [110] direction, as first identified by Hwang and coworkers.^[36] The relative formation energy of the neutral As₂I complex is predicted to be 1.92eV with respect to As⁰. We also calculate the formation energies of As₂I for the positive and negative charge state to estimate the donor and acceptor levels for As₂I, and according to our calculations, the As₂I complex is unlikely to be ionized under intrinsic conditions.

A diffusion pathway for neutral As₂I is presented in Fig. 3.3 with corresponding energy variations for both neutral and positive charge states. In the first step [(a) → (b)], by breaking the As_I-Si_A bond and Si_C-Si_E bond, As_I and Si_C atoms rotate together and form As_I-Si_E and As_{II}-Si_A bonds. In step [(b) → (c)], the strained As_I-As_{II} bond is broken and new bonds, As_I-Si_F and As_{II}-Si_C are formed. In the resulting local minimum state (c), the threefold coordinated As_I and Si_C and fourfold coordinated As_{II} all maintain the sp^3 hybridized configuration. In the next step [(c) → (d)], Si_C configuration inverts about the plane formed by As_I, As_{II} and Si_G; the hybridization of Si_C changes from sp^3 to sp^2 and again to sp^3 . Another inversion of As_I configuration occurs in the following step [(d) → (e)], and the unbonded electron pair on As_I is now pointing at the opposite direction. After reaching the state (e), conversion to the equivalent state (e') occurs by breaking the Si_C-Si_G bond and forming the Si_B-Si_C bond.

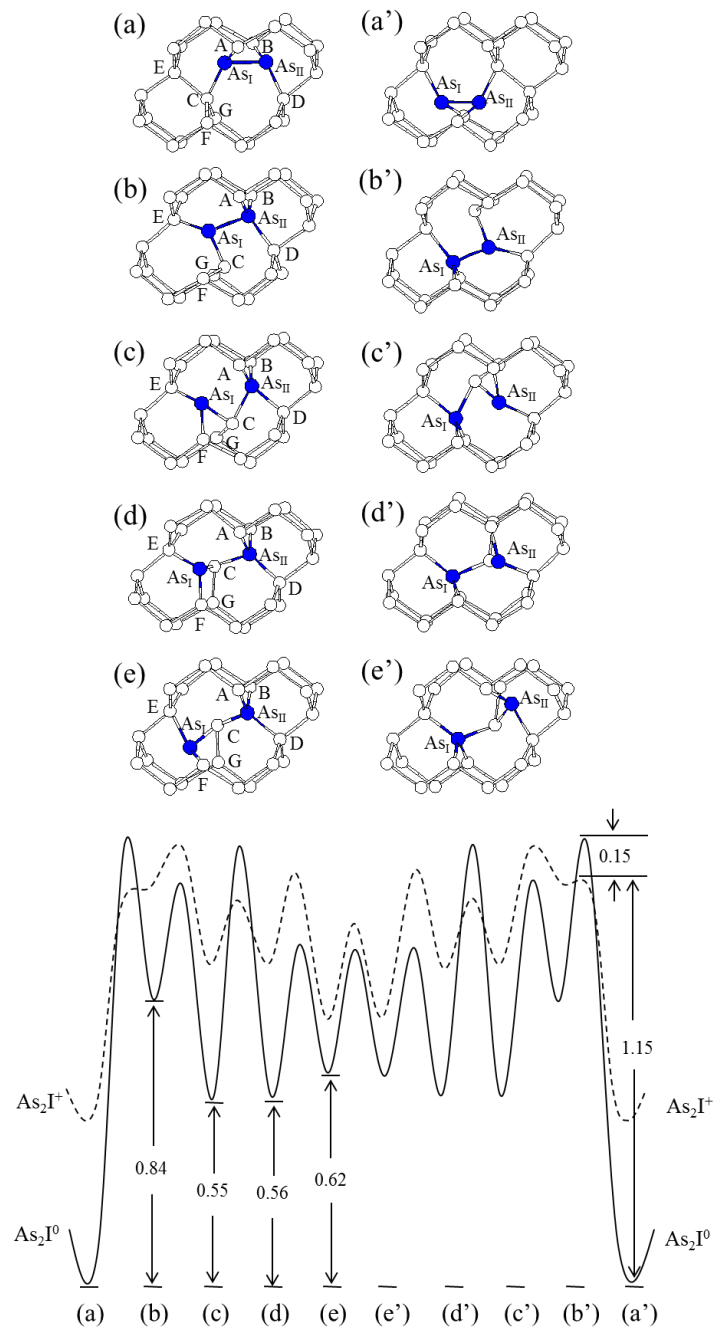


Figure 3.3 (Upper Panel) The diffusion pathway for As_2I^0 [(a)-(a')]. The As atoms are labeled As_I and As_II , while Si atoms involved are labeled A-G. The blue (dark-colored) and white ball represent As and Si atoms, respectively. (Lower Panel) Corresponding energy pathway (in eV) of As_2I^0 (solid line) and As_2I^+ (dashed line) diffusion.

Opposite to the As_I and As_{II} configurations observed in state (e), As_I is fourfold coordinated while As_{II} is threefold coordinated with an electron lone pair in the state (e'). As shown in Fig. 3.3, the states (a')-(e') are the mirror states of (a)-(e), thus the diffusion pathway from (e') to (a') follows the same mechanism as described above but in reverse direction. To evaluate the effect of charge variation, the positive As_2I , which follows the same diffusion pathway, is also considered. In reference to state (a), the relative energies of states (b)-(e) for the neutral (positive) pair are 0.84 (0.69), 0.55 (0.44), 0.56 (0.43), and 0.62 (0.29) eV, and the overall diffusion barrier is predicted to be 1.30 (0.80) eV. The energy variations for both charge states are put together as shown in Fig. 3.3 based on the relative formation energies of the neutral and positive As_2I under intrinsic condition. The positive and neutral As_2I follow the same diffusion pathway with the neutral state being more favorable; however, the As_2I^+ has lower barriers, which reduces the total diffusion energy barrier by 0.15 eV. This reduction at the first transition in energy barrier can be understood as the stable configuration of As atoms with unbounded electron pairs is disturbed by losing one electron, making the transition from (a) to (b) easier in the positive state.

As shown in Fig. 3.4, As_2I dissociation follows the same pathway as in diffusion up to (d). From (d) to (e), dissociation occurs predominantly by AsI liberation, i.e., $As_2I \rightarrow As + AsI$ and the structure (e) is considered as the final configuration for As_2I dissociation as its energy is comparable to that of the fully separated AsI and As. The relative energy of state (e) for the neutral (positive) state is 0.70 (0.44) eV. Since As at the substitutional site prefers to be ionized to As^+ , charge variation from neutral to positive is expected in the last transition step [(d) \rightarrow (e)]. However, as shown in Fig.3.4 (d) and (e), the favorable dissociation occurs in the neutral state instead, which can be explained if taken As^+ and AsI^- as the dissociation products rather than As^0 and AsI^0 .

Under intrinsic conditions, the energy gain from As ionization ($\text{As}^0 \rightarrow \text{As}^+$) is 0.27 eV, that compensates the 0.18 eV energy loss from ($\text{AsI}^0 \rightarrow \text{AsI}$) and results in 0.1 eV net gain.

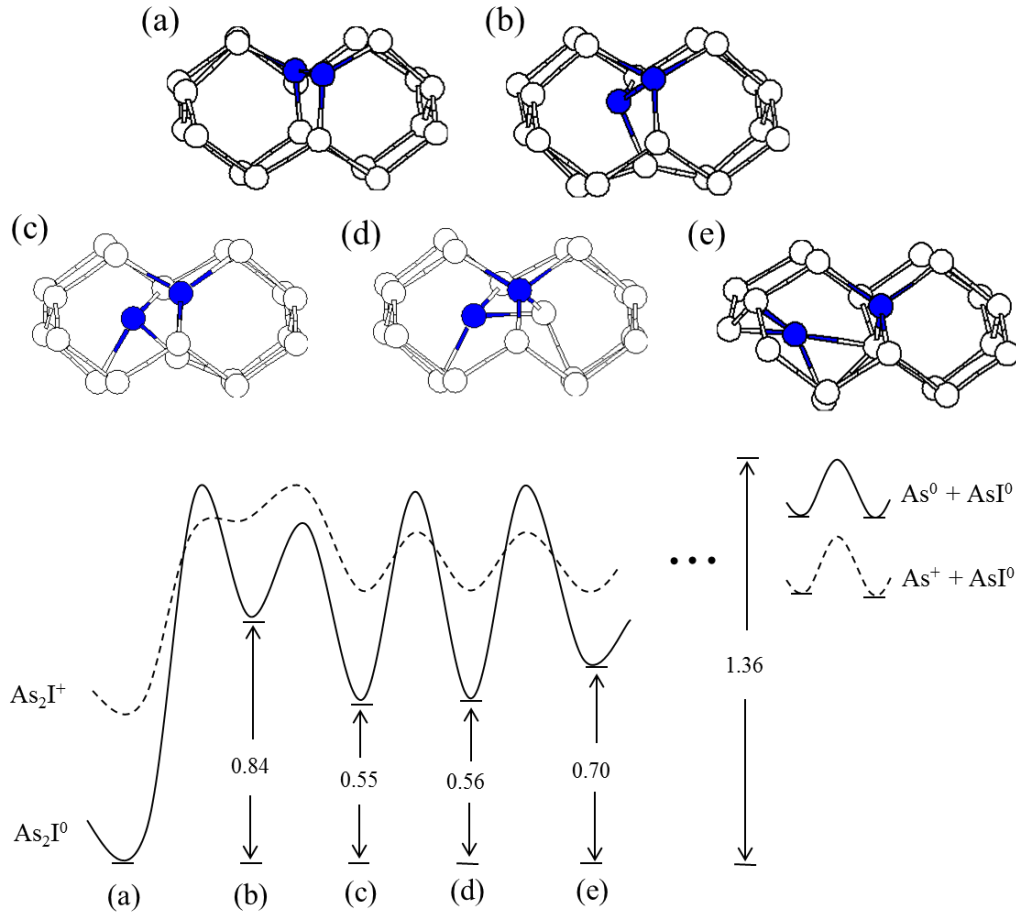


Figure 3.4 (Upper Panel) The dissociation pathway for As_2I^0 [(a)-(e)]. The blue (dark-colored) and white ball represent As and Si atoms, respectively. (Lower Panel) Corresponding energy pathway (in eV) of As_2I^0 (solid line) and As_2I^+ (dashed line) dissociation.

Moreover, the attractive electrostatic interaction between As^+ and AsI^- can add to additional energy gain. Therefore, the dissociation pathway follows the neutral charge state from (d) to (e). Considering the long range dissociation for the reason explained

earlier, the sum of As₂I binding energy and AsI migration barrier is 1.36 (0.62) eV for the neutral (positive) case. Accounting the barriers of both short- and long-range dissociations, overall dissociation barriers for As₂I⁰ (\rightarrow As⁰ + AsI) and As₂I⁺ (\rightarrow As⁺ + AsI) are predicted to be 1.36 eV and 0.80 eV, respectively. Furthermore with the possibility of charge variation, As₂I⁰ \rightarrow As⁺ + AsI⁰ becomes the preferential dissociation reaction by crossing a barrier of 1.21 eV under intrinsic conditions.

3.5 AsI₂

Fig. 3.5(a) shows the lowest-energy structure of AsI₂, which resembles the C_{1h} structure of neutral di-interstitial.^[37,38] Two Si interstitials (indicated as Si_A and Si_B) are aligned in the [110] direction while sharing a lattice site with the As atom. The relative formation energy of the neutral AsI₂ complex is estimated to be 4.97 eV with respect to neutral substitutional As. For the computed Si band gap of 0.63 eV, the first donor level of AsI₂ is predicted to be located 0.11 eV below the conduction band ($E_c - 0.1$ eV) while the first acceptor level is not within the bandgap, suggesting that the AsI₂ complex may favor the positive charge state under intrinsic conditions. The positive AsI₂ configuration exhibits no significant deviation from the neutral state geometry.

Fig. 3.5 shows a viable diffusion pathway for AsI₂ with the corresponding energy variations for neutral and positive charge states. Between two equivalent lowest-energy states [(a) and (c)], the As and four Si atoms (Si_A, Si_B, Si_C and Si_D) are relocated via a transitional state [(b)]. In this single transition step, diffusion and reorientation of the dumbbell are included. First, AsI₂ diffuses in the [111] direction defined by atoms Si_A and Si_D, and then the dumbbell (Si_B and Si_D) reorients, resulting in the new configuration (c). AsI₂ diffusion is analogous to the I₂ diffusion mechanism, except all detailed motion is included in one single step for AsI₂.^[39] The energy barriers for diffusion are

predicted to be 0.35 (0.20) eV in the positive (neutral) state. Taking the computed diffusion barriers and relative formation energies of the neutral and positive AsI_2 complexes, AsI_2 diffusion appears to occur more favorably in the positive charge state with an overall diffusion barrier of 0.35 eV.

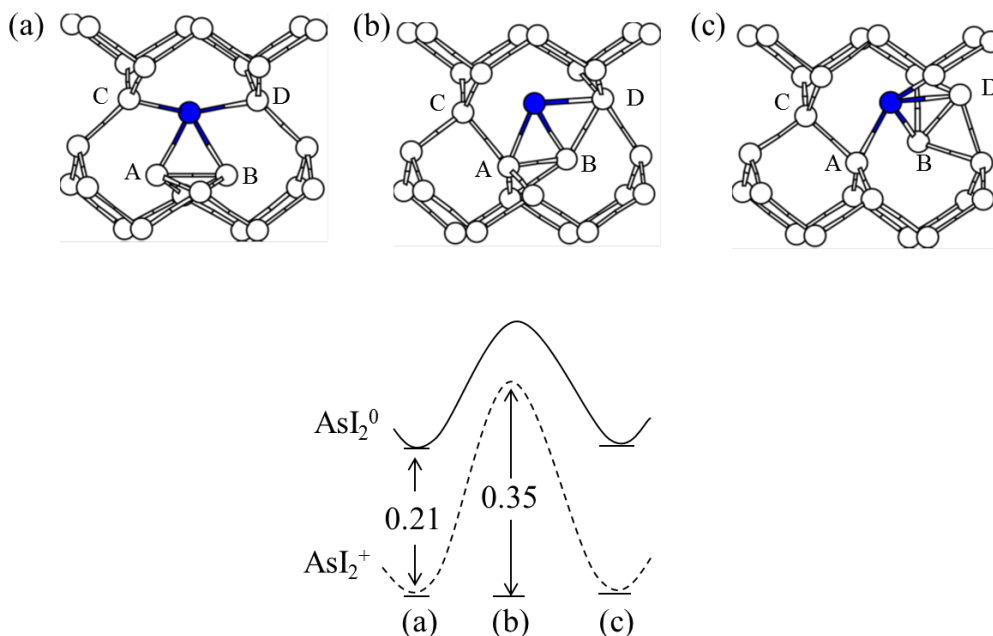


Figure 3.5 (Upper Panel) The pathway for AsI_2 diffusion [(a)-(c)]. The relevant Si atoms are labeled A-D. The blue (dark-colored) and white ball represent As and Si atoms, respectively. (Lower Panel) Corresponding diffusion energy pathway (in eV) of AsI_2^0 (solid line) and AsI_2^+ (dashed line).

Fig. 3.6 presents a viable route by which the positive AsI_2 complex dissociates to yield mobile I_2 and substitutional As. We also considered the possibility of AsI_2 dissociated into mobile AsI and I, but it appears to be energetically far less favorable (Recall that the sum of the relative AsI and I formation energies is 6.82 eV which is substantially greater than 5.53eV for the case of As + I_2 even in the neutral state). The

$\text{AsI}_2 \rightarrow \text{As} + \text{I}_2$ reaction follows the similar mechanism as AsI_2 diffusion, except that in the case of dissociation the Si interstitial pair (I_2) diffuses away while leaving the As atom at the substitutional site. Dissociation pathway shown in Fig. 3.6 occurs through four local minimum states labeled as (a), (b), (c) and (d).

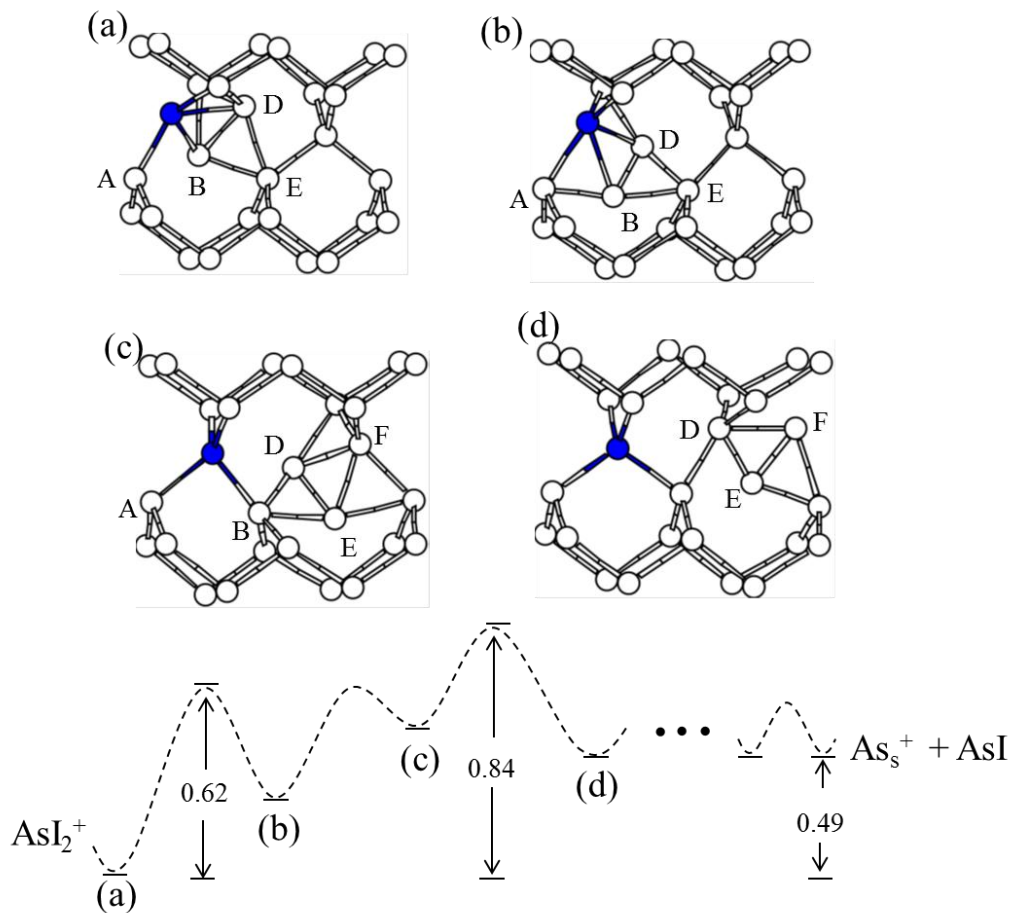


Figure 3.6 (Upper Panel) The pathway for AsI_2^+ dissociation [(a)-(d)]. The relevant Si atoms are labeled A-D. The blue (dark-colored) and white ball represent As and Si atoms, respectively. (Lower Panel) Energetics (in eV) along the AsI_2^+ dissociation pathway

In the first transformation [(a) \rightarrow (b)], two Si interstitials (Si_B and Si_D) in the AsI_2 complex translate in the $[-1 -1 -1]$ direction defined by Si_B and Si_D and form a I_2 dumbbell structure with the adjacent Si atom (Si_E) while holding As as a neighboring interstitial. In the subsequent transformation [(b) \rightarrow (c)], I_2 may migrate further away from As and form another dumbbell structure with adjacent Si (Si_E), leaving the As atom at the substitutional site. As the total energy of configuration (d) is comparable to that of the fully separated substitutional As and I_2 , it is taken as the final step to address AsI_2 dissociation. The relative energies of states (b), (c), and (d) are 0.22, 0.51 and 0.41 eV compared to that of state (a) and the energy barriers for the three transformation steps, (a) \rightarrow (b), (b) \rightarrow (c), and (c) \rightarrow (d) are 0.58, 0.39, and 0.33 eV, respectively. Along with the positive charge state, we also considered the dissociation energy pathway for the neutral one, which is demonstrated to be energetically less favorable. In addition, the dissociation energy barrier for AsI_2 in the long range is also examined. The sum of AsI_2 binding energy and I_2 migration barrier is 0.80 eV for the positive case. Considering the barriers of both short- and long-range dissociations, overall dissociation barriers for AsI_2^+ ($\rightarrow \text{As}^+ + \text{I}_2$) is calculated to be 0.84 eV.

3.6 As₂I₂

Fig. 3.7 (a) shows the predicted lowest-energy configuration of As₂I₂ in which each As is covalently bonded to three Si neighbors while having one lone pair of electrons, and thereby exhibits a tetrahedral sp^3 -like geometry. Our calculations show that the As₂I₂ complex is unlikely to be ionized under intrinsic conditions. The relative formation energy of neutral As₂I₂ is predicted to be 4.01 eV, with respect to substitutional As in the neutral state.

Fig. 3.7 shows the As₂I₂ diffusion pathway and energy variations along the local minimum states [(a), (b) and (c)] and their mirror states [(a'), (b') and (c')]. The first transition [(a) → (b)] involves rotation of two As and the adjacent Si atoms, and in the resulting configuration (b), the lone pair electrons originally located on As are delocalized causing a reduction in As-As bond distance. From (b) to (c), As_I, As_{II} and Si_B, translate and rotate collaboratively resulting in configuration (c) where two As atoms share one lattice site while atom Si_B is relocated in [111] direction to an interstitial site. The transformation from [(c)] to [(c')] involves a structural inversion into the equivalent mirror structure [(c')]. It marks the midpoint in diffusion of As₂I₂ to a new lattice site through subsequent steps ((c') → (b') → (a')) which are inverse order of previous ones ((a) → (b) → (c)). The energies of states (b) and (c) are 0.16 and 0.24 eV above that of state (a) and the energy barriers for the (a) → (b) and (b) → (c), and (c) → (c') are 1.07, 0.43 and 0.34 eV, respectively. As shown in the energetic pathway, the first transition determines the overall diffusion energy; also, in the step [(a) → (b)], charge variation from neutral to positive lowers the total energy barrier to 0.93eV.

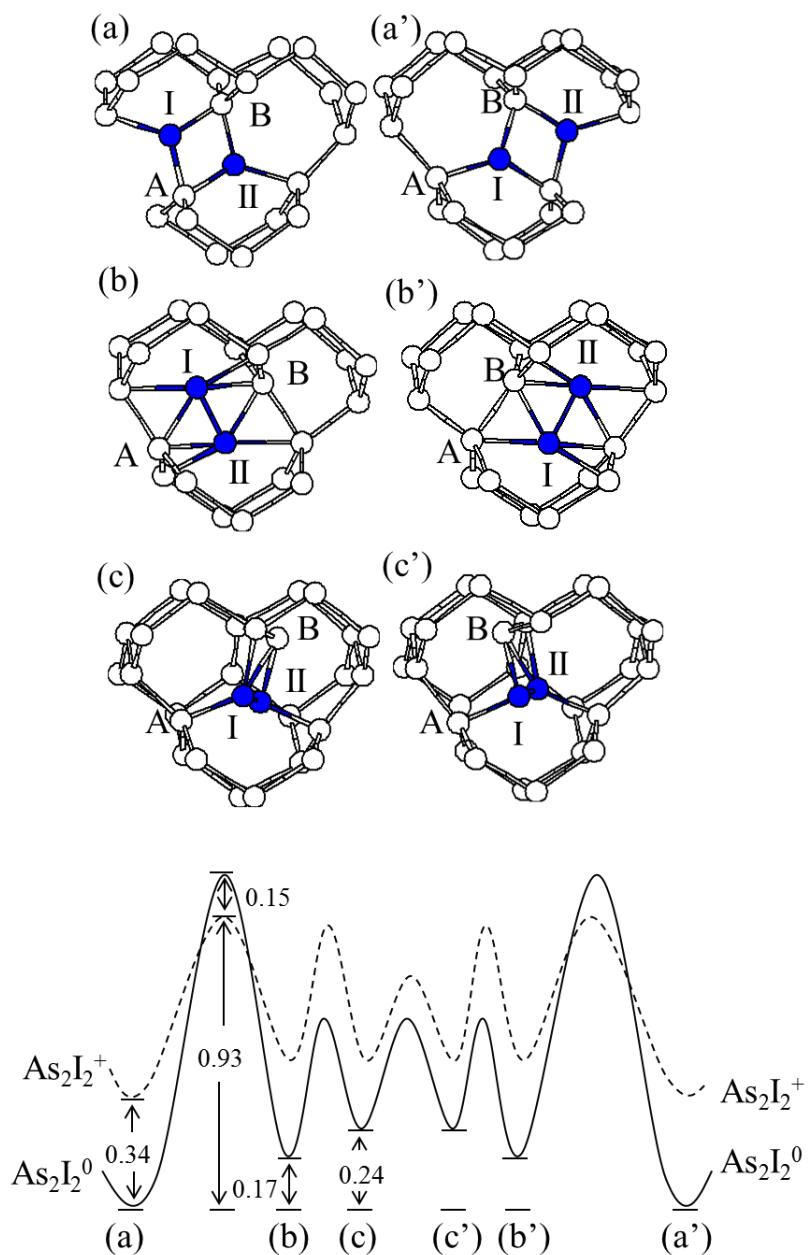


Figure 3.7 (Upper Panel) The diffusion pathway for As_2I_2 [(a)-(a')]. The As atoms are labeled I and II, while Si atoms involved are labeled A and B. The blue (dark-colored) and white ball represent As and Si atoms, respectively. (Lower Panel) Corresponding energetics (in eV) along the As_2I_2^0 (solid line) and As_2I_2^+ (dashed line) diffusion pathway

For the As_2I_2 dissociation, three possible sets, $\text{As}_2\text{I} + \text{I}$, $\text{AsI} + \text{AsI}$, and $\text{As} + \text{AsI}_2$, can be expected. To evaluate the relative ease of the dissociation reactions, we looked at their endothermicities based on the formation energy differences between As_2I_2 and its dissociation products. In the neutral state, the $\text{As}_2\text{I}_2 \rightarrow \text{AsI} + \text{AsI}$ reaction has the highest endothermicity of 2.13 eV, followed by the $\text{As}_2\text{I} + \text{I}$ and $\text{As} + \text{AsI}_2$ cases of 1.65 eV and 0.95 eV endothermicities, respectively. Considering more stable ionized products in intrinsic conditions, the endothermicity of the $\text{As}_2\text{I}_2 \rightarrow \text{As}^+ + \text{AsI}_2^+$ reaction is lowered even further comparing to its neutral case. Given the diffusion barriers of I, AsI and AsI_2 are quite comparable (see above), we expect the As_2I_2 dissociation to occur predominantly by releasing the mobile AsI_2 component; $\text{As}_2\text{I}_2 \rightarrow \text{As} + \text{AsI}_2$.

Fig. 3.8 shows the predicted viable route for As_2I_2 dissociation into As and AsI_2 , along with its corresponding energy variation. The [(a) \rightarrow (b)] transition steps for As_2I_2 diffusion and dissociation are identical; for structures (a) and (b), only the viewing perspective is different in Fig. 3.7 and 3.8. In a subsequent transformation [(b) \rightarrow (c)], As_{II} and Si_{A} move to adjacent sites causing the $\text{As}_{\text{I}}\text{-As}_{\text{II}}$ bond to break and As_{I} remains interstitial. As_{II} shares one lattice site with two Si atoms (Si_{A} and Si_{C}), a similar structure to AsI_2 . In transition step (c) to (d), As_{II} migrates to the next lattice site forming AsI_2 configuration with neighboring Si_{C} and Si_{D} , and As_{I} enters to the lattice site and bonds with four neighboring Si atoms. From (d) to (e), AsI_2 diffuses farther away from As_{I} , and again as the total energy is comparable to that of the fully separated configuration, structure (e) is taken as the final dissociation stage. In order to obtain the lowest dissociation pathway, we included possible charge variations for the dissociation products, such as As^+ and AsI_2^+ . The first step occurs in the same manner with the dissociation step [(a) \rightarrow (b)] and the second step [(b) \rightarrow (c)] follows the neutral charge state.

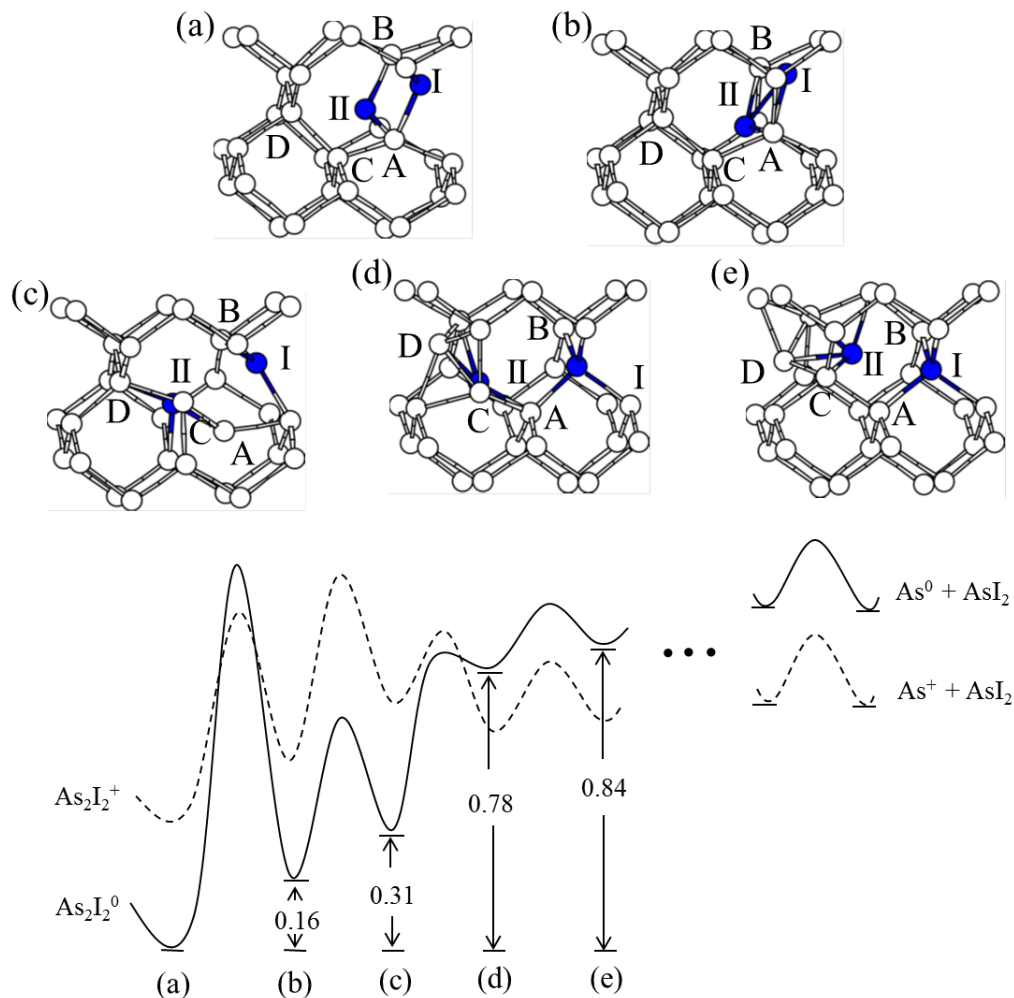


Figure 3.8 (Upper Panel) The dissociation pathway for As_2I_2 [(a)-(a')]. The As atoms are labeled I and II, while Si atoms involved are labeled A-D. The blue (dark-colored) and white ball represent As and Si atoms, respectively. (Lower Panel) Corresponding energetics (in eV) along the As_2I_2^0 (solid line) and As_2I_2^+ (dashed line) dissociation pathway

However, once the substitutional As is ionized, the pathway for the positive charge state ($\text{As}^+ + \text{AsI}_2^0$) is energetically more favorable than that of the neutral state ($\text{As}^0 + \text{AsI}_2^0$) and doubly positive state ($\text{As}^+ + \text{AsI}_2^+$). Although AsI_2^+ is more favorable than AsI_2^0 in the intrinsic region, it is energetically unfavorable for AsI_2^+ and As^+ to be in

close distance due to electrostatic repulsion. Therefore, AsI_2 is more likely to remain at neutral state when separated from the substitutional As^+ . The energies of states (b), (c), (d) and (e) are 0.16 (0.15), 0.31 (0.32), 0.78 (0.25) and 0.84 (0.28) eV higher than that of state (a) for the neutral (positive) state, respectively. Besides the dissociation in the short range, the long range dissociation is also taken into account to determine the overall barriers for As_2I_2 and As_2I_2^+ , which are 1.15 eV and 0.98 eV, respectively as shown in Fig. 3.8. If charge variation is allowed, $\text{As}_2\text{I}_2^0 \rightarrow \text{As}^+ + \text{AsI}_2^0$ becomes the favorable route for the dissociation by crossing a barrier of 0.93 eV under intrinsic conditions.

3.7 SUMMARY

First principles calculations for the structure and dynamics of the AsI , As_2I , AsI_2 , and As_2I_2 were presented. For AsI , the DFT-GGA calculations predict the diffusion barrier to be 0.21 eV and dissociation barriers to be 0.74 eV if charge variations are allowed during AsI dissociation ($\text{AsI}^0 \rightarrow \text{As}^+ + \text{I}^0$). It was found that for As_2I , the diffusion and dissociation involve the same rate-limiting step (breaking As-As bond), which requires considerable energy of 1.30 eV (this barrier can be reduced by 0.15 eV if charge variation is allowed under intrinsic conditions). Once the barrier of 1.30 eV is overcome, the As_2I can continue diffusing or dissociate with equal probability. For AsI_2 , it is calculated that this complex favors the positive charge state (AsI_2^+) under intrinsic condition. So, its diffusion and dissociation occur more favorably in the positive charge state by overcoming a barrier of 0.35 eV and 0.84 eV, respectively. Finally, for As_2I_2 , the first transition step involving rotation of two As and the adjacent Si atoms determines the overall diffusion and dissociation energy, similar to As_2I case.

The rate-limiting step requires of 1.07 eV in the neutral state, while charge variation from neutral to positive lowers the energy barrier to 0.93 eV.

Considering overall diffusion and dissociation energy barriers for all four As-I complexes, it can be expected that AsI and AsI₂ would be important diffusing species for As diffusion profiles. On the other hand, for As₂I and As₂I₂, their contributions to As diffusion profiles might be much less than AsI and AsI₂, since their diffusion and dissociation are as equally likely to occur with sizable energy barriers.

Chapter 4: Prediction of Defect Mediated N₂O Formation from N₂ and O₂ in Amorphous Silica

4.1 INTRODUCTION

Continuous scaling of metal-oxide-semiconductor devices has led to the use of ultrathin (less than 3 nm) layers of SiO₂ as a gate dielectric material. However, as the thickness of the SiO₂ layer has decreased, several concerns regarding diffusion of dopants and high defect densities in the SiO₂ layer have appeared. In particular, boron (B) penetration from the heavily *p*-doped poly-silicon gate electrode through the thin SiO₂ layer into the Si substrate has been recognized as a major concern^[40], which may not only deteriorate the gate dielectric quality but also degrade the device performance.

It is now well known that B diffusion is suppressed by incorporation of N into the SiO₂ layer or by using Si oxynitride films for the gate dielectric.^[41] However, Si oxynitride films prepared using thermal nitridation suffer from reliability degradation stemming from nitrogen-enhanced negative bias temperature instability (NBTI), which is caused by nitrogen atoms at the interface of the SiO₂ film and Si substrate.^[42] Plasma nitridation has recently been recognized as a better method, since it can introduce nitrogen atoms near the surface of SiO₂ films.^[43-45]

In plasma nitride films, a peculiar XPS peak was observed, which is not found in oxynitride films generated by thermal nitridation and also, additional migration of atomic N towards the SiO₂/Si interface was detected after O₂ post-annealing.^[43,44] Since N atoms at the SiO₂/Si interface are undesirable due to nitrogen-enhanced NBTI, atomic N migration toward the interface during O₂ post-annealing should be prevented. However, efforts to mitigate this problem have been hampered by a lack of mechanistic understanding of the plasma nitridation and O₂ post-annealing process. Thus, this work

based on first principles calculations was performed to clarify these underlying mechanisms.

Various nitriding species, such as N_2 , N_2^+ , N and N^+ , exist in the plasma gas source, and it has been observed that these energetic charged ions are neutralized when approaching the surface of a semiconductor or an insulator.^[46] The neutralization process, so called resonance neutralization, occurs as electrons tunnel from the substrate to charged ions and populate a resonant level in the ions.^[47] The charge exchange between the plasma ions (N^+ and N_2^+) and SiO_2 surface leads to neutralized particles (N and N_2) and holes trapped in SiO_2 . Since the oxygen vacancy defects [$\equiv Si-Si \equiv$, where \equiv indicates a Si-O bond (dimer configuration)] are dominant hole traps in SiO_2 , it can be expected that holes generated during resonance neutralization are likely trapped in oxygen vacancies, which can only occur during plasma nitridation. This implies that positively charged oxygen vacancies might be involved in reaction with neutralized nitriding species (N and N_2) or O_2 molecules introduced during O_2 annealing.

In this chapter, we first examined various configurations of positively charged oxygen vacancies by performing *ab initio* molecular dynamics simulation, since hole trapped dimer configuration can easily convert into other oxygen vacancy related defects. Then, we further investigated the possible interactions between oxygen vacancy related defects and N_2 (O_2) molecules. Finally, we demonstrated the oxygen vacancy mediated reaction between N_2 and O_2 , which might result in formation of N_2O molecules during high temperature O_2 post annealing.

4.2 CALCULATION METHODS

The calculations reported herein were performed on the basis of spin-polarized density functional theory within the generalized gradient approximation^[31], as implemented in the well-established Vienna *ab initio* Simulation Package (VASP).^[32] The projector augmented wave (PAW) method with a planewave basis set was used to describe the interaction between ion cores and valence electrons.^[48] During geometry optimization (energy minimization), all atoms were fully relaxed using conjugate gradient method until residual forces on constituent atoms becomes smaller than 5×10^{-2} eV/Å. In geometry optimization, we employed a planewave cutoff energy of 408 eV and a $(2 \times 2 \times 2)$ k-point grid in the scheme of Monkhorst-Pack for the Brillouin zone sampling.^[33] Reaction pathway and barriers were determined using the nudged elastic band method with 6-8 intermediate images for each elementary step.^[34]

4.3 POSITIVELY CHARGED OXYGEN VACANCY: STRUCTURAL TRANSFORMATION, ENERGETICS, AND MIGRATION

We first constructed ten independent model structures of bulk *a*-SiO₂, each of which contains 33 SiO₂ units. For each *a*-SiO₂ supercell, one single O vacancy ($\equiv\text{Si}-\text{Si}\equiv$) was created by removing a bridging O atom. The Si-Si bond distances of the neutral O vacancies vary between 2.30 and 2.35 Å. Removal of an electron from each of the neutral O vacancies, followed by structural relaxation, results in a significant increase in the Si-Si bond distance to 2.46-2.71 Å. To examine possible reconfigurations of the hole trapped O vacancies in the dimer configuration, we performed *ab initio* MD simulations in the canonical NVT ensemble at 1000K. During 15 picoseconds of simulation, four out of ten dimer structures remained unchanged while

two underwent reconfiguration into the back puckered configuration and four into the front puckered configuration.

4.3.1 Positively charged dimer configuration

While the hole trapped (positively charged) dimer configuration is unstable and tends to pucker with back oxygen in crystalline SiO_2 (α -quartz)^[49], it is predicted to be stable in a - SiO_2 .^[50] Also, experiments have suggested that positively charged dimers are E'_δ centers in a - SiO_2 ^[50-52] although there are still controversies concerning their microscopic structures.^[53,54] At the end of our MD simulations, four (out of ten) positively charged oxygen vacancies remained as dimers, as shown in Fig. 4.1. Due to hole trapping, the Si-Si bond has one shared electron in between, resulting in weakened bond strength as indicated by the elongated Si-Si distance (increased from 2.30-2.35 to 2.4-2.7 Å).

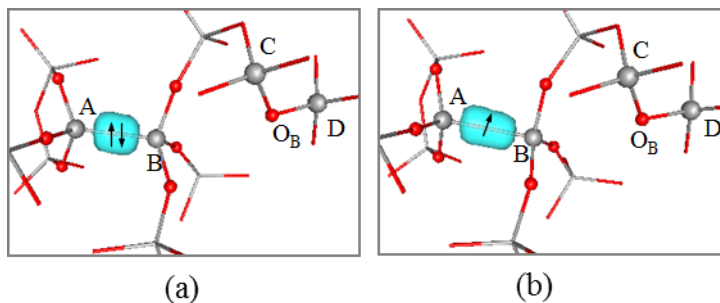


Figure 4.1 (a) neutral and (b) positively charged Si-Si dimer configuration (indicated as A and B). The isosurfaces of Wannier functions (blue colored) show the paired ($\uparrow\downarrow$) and unpaired (\uparrow) electron density for the neutral [(a)] and positively charged [(b)] state, respectively. The gray and red colored balls represent Si and O atoms, respectively.

When an electron is added, the neutral dimer with paired electrons is spontaneously restored. However, if the electron is localized at one Si atom ($\equiv\text{Si}\cdot$ and $+\text{Si}\equiv$) and there is available oxygen nearby, Si^+ can pucker with the bridging oxygen and undergo further structural transformation.

4.3.2 Back puckered configuration

Due to the electrostatic attraction between the Si^+ and back bridging O atom, the empty sp^3 orbital of Si^+ is filled by the oxygen lone electron pair, and results in a back puckered configuration. Our MD simulations identified two stable back puckered configurations, and based on these, two different pathways are suggested. Fig. 4.2 shows the structural transformation routes via hole and subsequent electron trapping. The positively charged dimer configuration [(b1)] relaxes into a back puckered configuration [(c1)] in which the unpaired electron residing on Si_A points toward Si_B (which is positively charged and interacts with the back bridging O_B). Configuration [(c1)] has been reported by earlier studies^[50,51,55], and it is similar to the FFY model proposed by Feigl, Fowler, and Yip for the E_1' center in α -quartz.^[50,56,57] The state (c1) is predicted to be 0.29 eV less favorable than B1. Despite the seeming unfavorability, such structural transformation is possible owing to the flexible of the amorphous network. Contrarily, it has also been reported that on average, E_γ' centers are about 0.6 eV lower than E_δ' centers.^[50] The discrepancy is not unexpected considering our values are obtained from a single amorphous structure, which may have prevented the energy variation in a - SiO_2 from being properly accounted for.^[58] When an electron is trapped in [(c1)], initially it goes to an unpaired electron on Si_A , resulting in a trivalent Si_A with a lone electron pair, and a dipole formed between the negatively charged Si_A and positively

charged Si_B . This metastable dipole can easily collapse into the original neutral dimer configuration [(d1)].^[50]

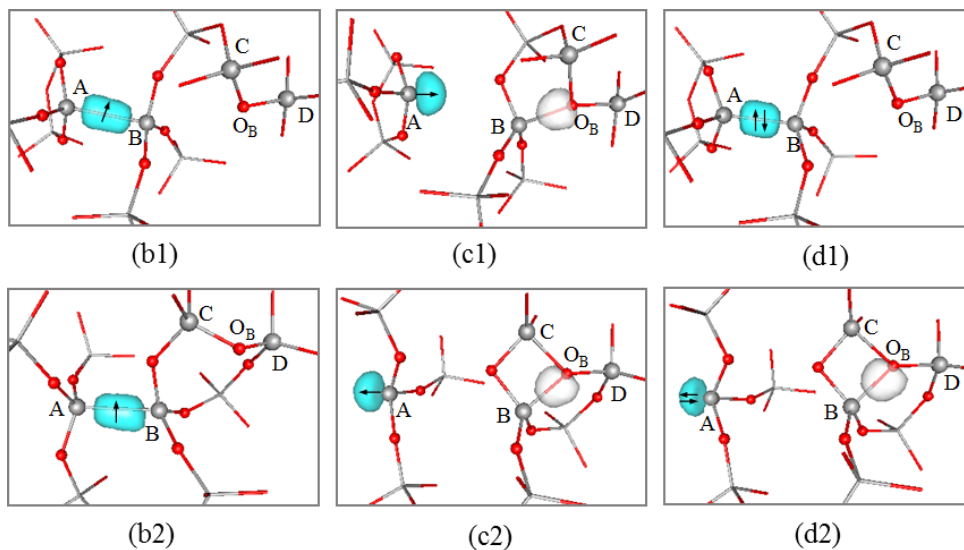


Figure 4.2. Two predicted paths for transformation of positively charged dimers [(b1) and (b2)] to back puckered configurations [(c1) and (c2)] and configurations after trapping one additional electron are shown in (d1) and (d2), respectively. The blue-colored isosurfaces show the unpaired (\uparrow) and paired ($\uparrow\downarrow$) electron and the white isosurfaces show the lone pair of the O_B atom which forms a dative covalent bond with the positively charged Si atom. The gray and red colored balls represent Si and O atoms, respectively.

Next, another back puckered configuration [(c2)] is considered, in which the unpaired electron residing on Si_A points away from the positively charged Si_B ; [(c2)] is called a back projected puckered configuration as suggested by Griscom and Cook.^[59] To convert a positively charged dimer into this configuration, a sufficiently large void space for Si_A is required, and a high-energy barrier (~ 1.5 eV) for this transformation was predicted.^[51] Our calculations estimated that the energy of state (c2) is 0.18 eV higher than that of (b2). Although [(c2)] may seem slightly unfavorable compared to [(b2)],

we find that once formed, [(c2)] was stabilized and did not revert back to [(b2)]. When [(c2)] is recharged by accepting one electron, a lone electron pair is formed on Si_A pointing in the opposite direction of Si_B and O_B. While the energy state of such configuration [(d2)] is 3.47 eV higher than that of [(a) in Fig. 4.1], the unfavorable directionality and distance inhibits the interaction between Si_A and Si_B, and hence the unlikelihood of [(d2)] returning to the original neutral dimer configuration. Note that this outcome is different from what was demonstrated in pathway one; here, no significant structural change can be expected going from [(c2)] to [(d2)] with one trapped electron.

4.3.3 Front puckered configuration

Our AIMD simulations show that Si atom of a positively charged dimer can also interact with a front bridging oxygen as has been previously speculated.^[60] Hereafter, this configuration is called 'front puckered' to distinguish it from the back puckered one. A similar structure has been reported as the forward-oriented configuration.^[58] Comparatively, there are more accessible front-bridging O sites than the favorable back-bridging ones; the later only amounts to about 10% of the total bridging O sites.^[61]

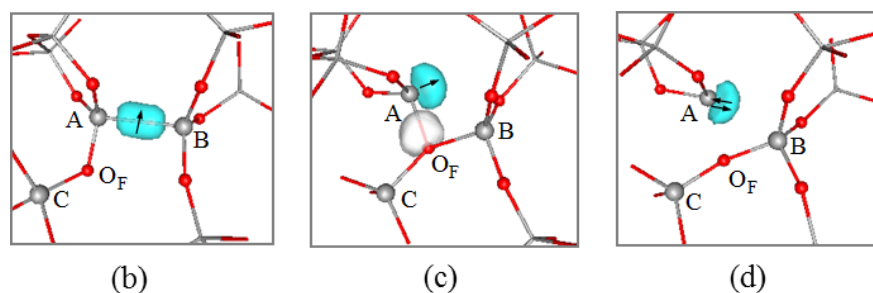


Figure 4.3 Predicted path for the transformation of a positively charged dimer [(b)] to a front puckered configuration [(c)] and configuration after trapping one additional electron is shown in (d). The blue-colored isosurfaces show the unpaired (\uparrow) and paired ($\uparrow\downarrow$) electron and the white isosurfaces show the lone pair of the O_F atom which forms a dative covalent bond with the positively charged Si atom.

Figure 4.3 demonstrates the structural transformation of a front puckered configuration upon hole trapping and subsequent electron capturing. From configurations [(b)] to [(c)], Si_B on the positively charged dimer interacts with the front bridging O atom (O_F), leading to the formation of a front puckered configuration, in which an unpaired electron resides on Si_A and a positive charge is trapped in Si_B. Although a dative bond is originally formed between Si_B and O_F, the positive charge is not strictly localized on Si_B but partially distributed over Si_A, Si_B and Si_C, as pointed out in Ref. [60]. When the E' center [(c)] is neutralized by trapping an electron, the accepted electron is paired with the electron residing on Si_A, and the dative bond between Si_A and O_F is broken, leading to the formation of divalent Si that has two Si-O bonds and a lone pair of electrons in a sp^2 orbital [(d)], also known as ODC(II).^[60] Such structural conversion between [(c)] and [(d)] has been suggested experimentally in *a*-SiO₂ where the trace of E' center measured via EPR signals start to appear just upon the bleaching of ODC(II) optical signals.^[62] It is worth pointing out that the divalent Si can further undergo conversion to an O vacancy in the dimer configuration by breaking a neighboring Si-O bond.^[63]

Overall, the transformation mechanism shown in Fig. 4.3 is consistent with the interconversion mechanism proposed by previous theoretical studies, in which the front puckered configuration can form from a divalent Si upon ionizing radiation.^[60] All front puckered configurations follow the same transformation pathway with only slight energy variation at each state due to the amorphous nature of the oxide. The energies at (c) vary from -0.7 to 0.7 eV with respect to the positively charged dimer state; these values are in good agreement with the calculations performed on *a*-SiO₂ clusters.^[58] For state (d), there are also energy variations between 0.84 eV and 2.30 eV with respect to the neutral dimer configuration.

4.3.4. Migration of positively charged oxygen vacancy

The puckered configuration can possibly undergo further transformation involving migration of the positively charged Si. A previous study suggested possible migration of the positively charged Si (E_1' center) in α -quartz through continuous back-puckering with a barrier of ~ 0.6 eV.^[64] A similar mechanism can be expected in a -SiO₂; such transformation was observed in one of the front puckered configurations, as depicted in Fig. 4.4, where structures (a)-(c) each represents a local minimum. During the transition from (a) to (b), the partially localized positive charge on Si_B is transferred to Si_C, which in turn, forms a new dative bond with O_{B1}. From (b) to (c), the positive charge migrates from Si_C to Si_E, which then puckers with O_{B2}, resulting in a large separation distance from Si_B. The transformation described above can only occur if the back-oxygen is available near the positively charged Si atom; given the favorable back-oxygen roughly amounts to 10% of the total bridging oxygen sites^[61], such transformation through continuous back-puckering is expected to take place only occasionally.

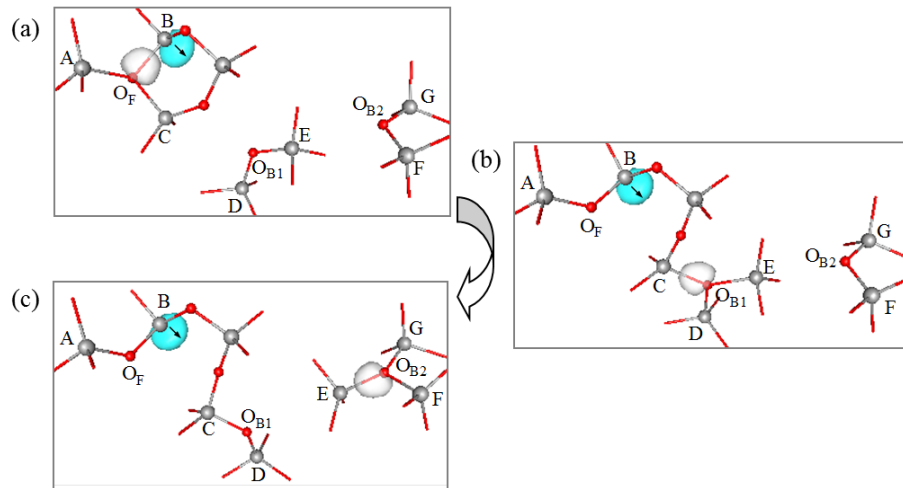


Figure 4.4 Predicted migration pathway for the puckered configuration.

The total energy at each state tends to decrease along the transformation; the relative energies with respect to that of the initial positively charged dimer configuration are predicted to be 0.65, 0.76 and -0.49 eV for states (a), (b) and (c), respectively. The pathway proposed above is also consistent with the previous theoretical study, in which the transformation from ionized ODC(II) to E' center (equivalent to Fig. 4.4(a)→(c)) is identified as nearly barrierless.^[65]

4.4 INTERACTION BETWEEN POSITIVELY CHARGED OXYGEN VACANCY AND MOLECULAR N₂

4.4.1 Positively charged dimer configuration

We looked at the possibility of N₂ insertion into a positively charged dimer which has a Si-Si bond distance of 2.5–2.7 Å. Two possible configurations were considered.

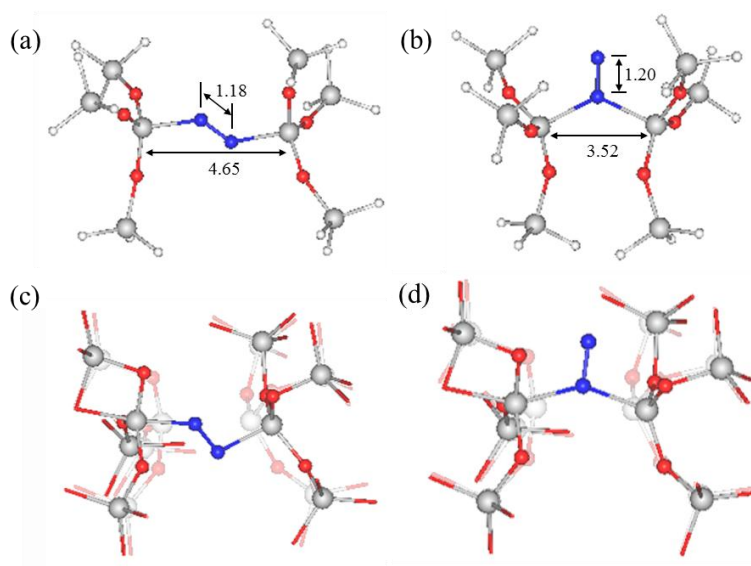


Figure 4.5 N₂ insertion into a positively charged dimer configuration: cluster model calculation [(a) and (b)] and *a*-SiO₂ bulk calculation [(c) and (d)]. The gray, red, blue, and white colored balls represent Si, O, N, and H atoms, respectively. All distances are given in Å.

First, as depicted in Fig. 4.5 (a), N₂ is inserted by breaking a Si-Si bond and forming new Si-N bonds at both N ends, which is hereafter indicated as (Si-N=N-Si)⁺ where '-' and '=' represent single and double bonds, respectively. Second, as depicted in Fig. 4.5 (b), one N is bonded to both Si atoms and forms two Si-N bonds, (Si-[N=N]-Si)⁺. From our cluster model calculations for configurations illustrated in Fig. 4.5 (a) and (b), the N₂ binding energies are predicted to be 0.74eV and 0.31eV while the N-N (Si-Si) bond distances are increased to 1.18 (4.65) Å and 1.20 (3.52) Å from 1.11 (2.35) Å, respectively. Note the binding energies calculated here do not account for the strain from the neighboring network since the cluster model is almost strain free. Therefore, we also looked at the formation of (Si-N=N-Si)⁺ and (Si-[N=N]-Si)⁺ in an *a*-SiO₂ matrix, as illustrated in Fig. 4.5 (c) and (d). The N₂ binding energies are predicted to be -0.80/-2.30 eV and -0.98/-1.20 eV for (Si-N=N-Si)⁺ and (Si-[N=N]-Si)⁺ in two independent *a*-SiO₂ samples each of which consists of 33 SiO₂ units with an O vacancy. Unlike in the cluster cases, the considerable negative binding energies suggest that N₂ incorporation into a hole trapped dimer would be energetically unfavorable in bulk *a*-SiO₂. This is mainly attributed to the strain imposed by the neighboring silica network as the dimer is significantly stretched upon N₂ insertion. The overall energy gain by the formation of new Si-N bonds is not enough to compensate for the strain effect.

4.4.2 Si dangling bond type

Next, we analyzed the interaction between N₂ molecules and dangling bond type defects. In the cluster model, we performed calculations using (H₃Si-O)₃-Si• and (H₃Si-O)₃-Si⁺, which are assumed to mimic ≡Si• and ≡Si⁺, as shown in Fig. 4.6 (a) and (b) where • and + represent a dangling bond and a positive charge, respectively.

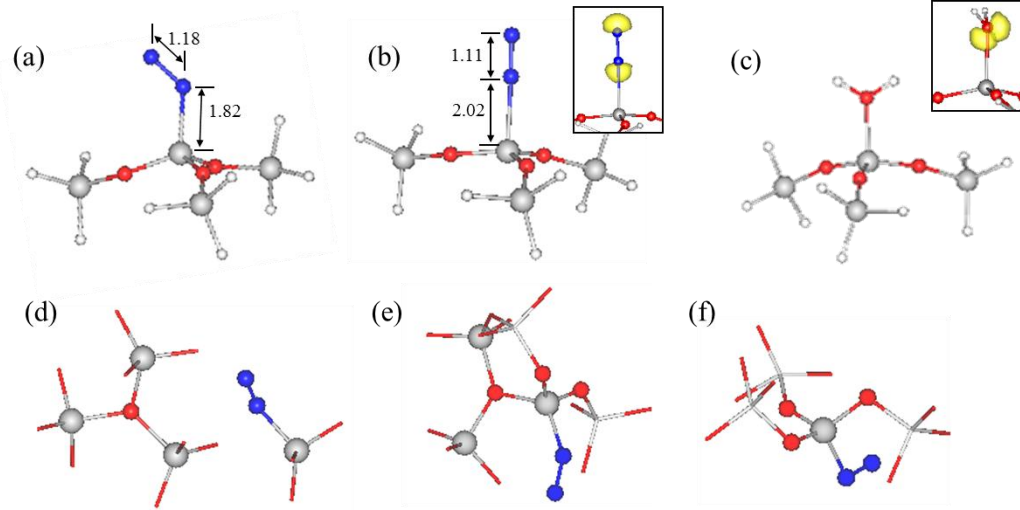


Figure 4.6 Interaction of N_2 molecule with (a) $\equiv\text{Si}\cdot$ and (b) $\equiv\text{Si}^+$, and interaction of H_2O molecule with (c) $\equiv\text{Si}^+$ from cluster model calculations. N_2 interaction with (d) a back puckerd, (e) front puckerd, and (f) isolated E' center in the bulk system. All distances are given in Å.

In Fig. 4.6 (a), the N-N bond distance increases from 1.11 Å for triple bond to 1.18 Å. According to the Bader charge analysis, the charge associated with Si decreases by $0.7e$ while that of the N bonded with the Si increases by $0.7e$. The other N remains its intrinsic value, $5.0e$, indicating that $0.7e$ is transferred from Si to the bonded N atom. In the $(\text{H}_3\text{Si-O})_3\text{-Si-N=N}$ configuration, due to the charge transfer between Si with an unpaired electron and N_2 , the antibonding state of N_2 is partially occupied and results in an increase in N_2 bond distance by 0.07 Å. In Fig 4.6 (b), the N-N bond distance is 1.11 Å, the same as in N triple bond. The lonepair electrons of N pointing towards the Si^+ form a dative Si-N bond [see inset of Fig 4.6 (b)], which is much weaker than a normal Si-N bond. The binding energies of N_2 with $\equiv\text{Si}\cdot$ and $\equiv\text{Si}^+$ are 0.14 eV and 0.53 eV, respectively. Unlike the isolated defects predicted by the

cluster models, defects are more likely to interact with the surrounding SiO₂ network in the bulk structure. To demonstrate this, a cluster model was generated for ≡Si⁺ interacting with H₂O, which is suitable to represent the dative bond formation between Si and O as shown in Fig. 4.6 (c). The binding energy of one of the lone pair electrons from H₂O with ≡Si⁺ and is 1.83 eV [see inset of Fig. 4.6 (c)] while that with ≡Si• is highly unfavorable. Similarly, using the cluster model, the binding energy between ≡Si⁺ and the bridging O in SiO₂ linkage is predicted to be 2.09 eV. Because the O atom in H₂O and SiO₂ is nucleophilic, it bonds easily with electrophilic reagents, such as ≡Si⁺ rather than ≡Si•. Note that the much higher binding energies and therefore higher energy gains are observed for ≡Si⁺/H₂O and ≡Si⁺/SiO₂ compared to ≡Si⁺/N₂. Thus, the interaction between ≡Si⁺ and N₂ is energetically less favorable (only ~0.5 eV of energy gain) to take place in the bulk structure.

As most ≡Si⁺ are likely to be consumed by binding with nearby bridging O atoms, only ≡Si• is left available to interact with N₂. Fig. 4.6 (d)-(f) show the N₂ incorporated structures obtained from the puckered, forward oriented, and isolated E' center in the bulk system. The highest binding energy between N₂ and ≡Si• among those three configurations is only 0.3 eV. Occasionally, it is observed that the binding energy is higher in bulk than in the cluster model (0.14 eV), which can possibly be attributed to the energy gain from the overall stabilization as the dangling bond is terminated by N₂; nevertheless, the probability of binding is expected to be low. Furthermore, we also examined the possibility of the puckered configuration forming a positively charged N₂ linkage, the same as shown in Fig. 4.5 (c). However this structure is even less favorable than what is shown in Fig. 4.6 (d).

In summary, the binding energy calculations conclude that it is unlikely for N₂ to bind with defects in amorphous silica; instead, it tends to stay as a free molecule. Our

result is in good agreement with the recent experimental observations. The XPS spectra for the plasma nitride silica^[43-45,66] shows a distinct peak at 403 eV in addition to the main peak for the Si₃≡N configuration at 398 eV. This additional peak at 403 eV was identified as interstitially trapped N₂ molecule by Chung et al. using N K-edge spectra of SiON film.^[66] Given the gas phase N₂ molecule peak at 410 eV, this peak shift to 403 eV is attributed to the N₂ interaction with the surrounding amorphous oxide.^[67] Such effect is confirmed by another experimental results that the vibrational frequency of interstitially trapped N₂ (2325 cm⁻¹) is slightly lower than that of the gas phase N₂ (2330 cm⁻¹).^[68]

4.5 INTERACTION BETWEEN POSITIVELY CHARGED OXYGEN VACANCY AND MOLECULAR O₂

4.5.1 Positively charged dimer configuration

We evaluated the possibility of O₂ insertion into a positively charged dimer via similar insertion and bonding mechanisms as proposed in Section 4.4.1. Two possible configurations are illustrated in Fig. 4.7 (a) (Si-O-O-Si)⁺ and (b) (Si-[O-O]-Si)⁺. The O₂ binding energies calculated from our cluster models are 3.25eV and 2.59eV while the O-O (Si-Si) bond distances are increased from 1.24 (2.35) Å to 1.39 (4.23) Å and 1.37 (3.47) Å for (a) and (b), as shown in Fig. 4.7. The higher binding energy observed in O₂ as opposed to N₂ insertion is attributed to the larger energy gain from Si-O formation (4.68 eV for Si-O; 3.68 eV for Si-N) and the smaller energy loss associated with breaking O₂ double bonds (O=O → O-O, ΔE = 3.65 eV; N≡N → N=N, ΔE = 5.43 eV). The formation of (Si-O-O-Si)⁺ and (Si-[O-O]-Si)⁺ in an *α*-SiO₂ matrix was also evaluated as illustrated in Fig. 4.7 (c) and (d).

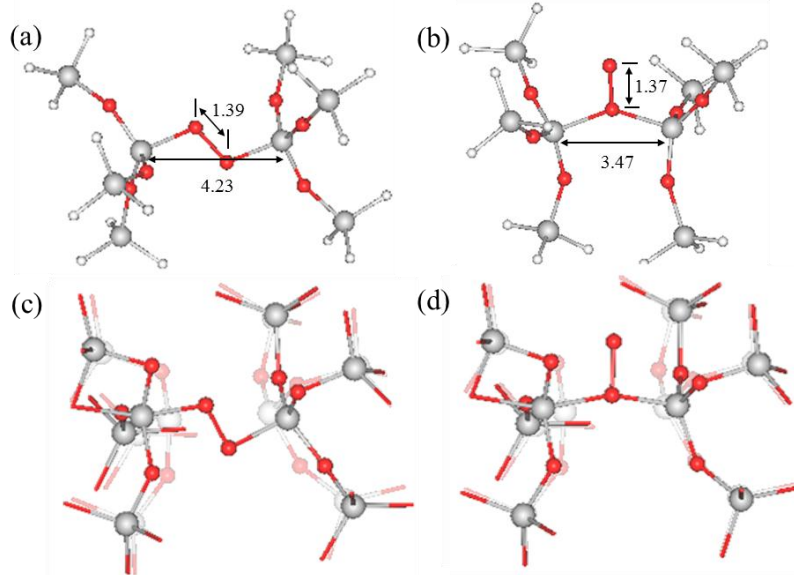


Figure 4.7 O_2 insertion into a positively charged dimer configuration: cluster model calculation [(a) and (b)] and $a\text{-SiO}_2$ bulk calculation [(c) and (d)]. The gray, red, and white colored balls represent Si, O, and H atoms, respectively.

For two independent $a\text{-SiO}_2$ samples, the O_2 binding energies for $(\text{Si-O-O-Si})^+$ and $(\text{Si-[O-O]-Si})^+$ are calculated to be 0.65/2.23 eV and 1.40/1.50 eV. In both cases, the positive binding energy suggests such formation in $a\text{-SiO}_2$ is energetically favorable; the formation energy gain is sufficient to compensate for the strain energy loss induced by the surrounding SiO_2 network. Previous study shows that O_2 insertion into the neutral dimer is a favorable exothermic reaction, where a peroxy linkage is formed by overcoming the 0.3 eV energy barrier.^[69] In the positive dimer case, O_2 insertion is presumably easier due to the weaker Si-Si bond.

4.5.2 Si dangling bond type

The reaction of O_2 with $\equiv Si^\bullet$ and $\equiv Si^+$ was studied using cluster models as shown in Fig 4.8 (a) and (b). The O_2 binding energies at the $\equiv Si^\bullet$ and $\equiv Si^+$ sites were estimated to be 2.59 eV and 0.30 eV, respectively. For the $\equiv Si^\bullet + O_2$ case [Fig. 4.8 (a)], the Bader analysis predicted charge transfer from the trivalent Si to the adsorbed O_2 is approximately $0.8e$. The transferred electron occupying the O_2 antibonding state ($1\pi_g$) causes an increase in the bond length from 1.24 Å to 1.36 Å. For the $\equiv Si^+ + O_2$ case [Fig. 4.8 (b)], O_2 forms a dative bond with the $\equiv Si^+$ by sharing one of the O lonepair electrons pointing towards the $\equiv Si^+$ [see inset of Fig 4.8(b)].

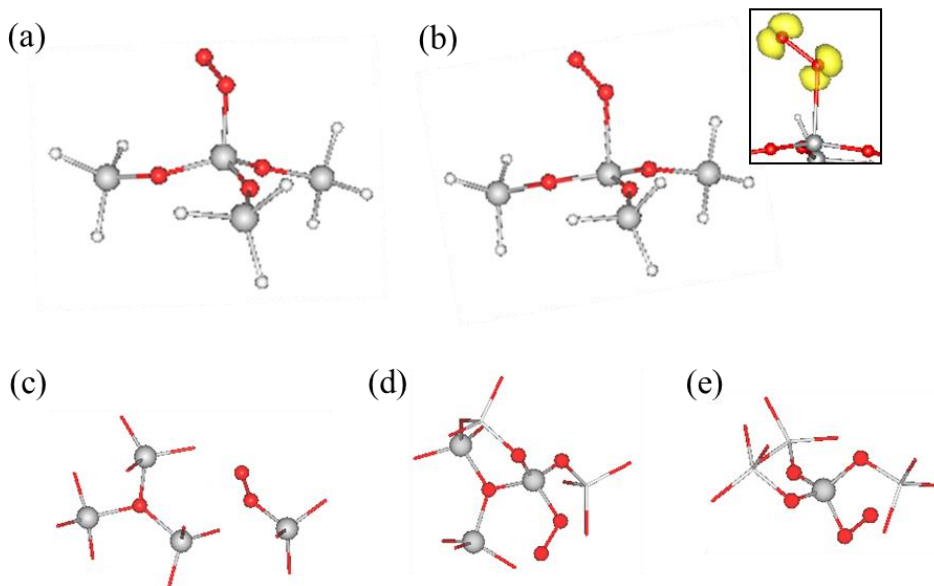


Figure 4.8 Interaction of O_2 molecule with (a) $\equiv Si^\bullet$ and (b) $\equiv Si^+$ from cluster model calculations. O_2 interaction with (c) a back pucker, (d) front pucker, and (e) isolated E' center in the bulk system.

Since no charge transfer is involved, the O-O distance is the same as that of a O₂ molecule. Next, we performed calculations to assess the interaction between O₂ and Si• in back puckered, front puckered, and isolated E' center configurations in bulk *a*-SiO₂. Positive binding energies (larger than 1 eV) were found for all three cases, suggesting favorable formation of the peroxy radical (POR, ≡Si-O-O•), which is consistent with the experimental observation that as O₂ is introduced, the optical signal coming from E'_γ center decreases and that of POR increases, indicating the occurrence of Si• + O₂ → ≡Si-O-O• reaction. It is worth mentioning that since O-O bond strength in POR is weaker than the Si-O bond, thermal transformation from ≡Si-O-O• to ≡Si-O• + O has been observed at high temperature (>650 K)^[70], and it is possible that the released atomic O can insert into the adjacent Si-O-Si network, resulting in Si-O-O-Si linkage. The interaction between ≡Si+ and O₂ in bulk *a*-SiO₂ is not discussed because of the beforementioned reasons in Section 4.4.2.

4.6 OXYGEN VACANCY MEDIATED REACTION BETWEEN N₂ AND O₂

Recall the result summarized in Section 4.4 and 4.5. N₂ tends to stay as interstitial molecule in bulk *a*-SiO₂, whereas O₂ easily adsorbs to hole trapped O vacancy defects and forms charged/neutral peroxy linkage (≡Si-O-O-Si≡) or peroxy radical (≡Si-O-O•). Given the charged peroxy linkage and peroxy radical, we further examined the reaction with interstitially trapped N₂.

4.6.1 Peroxy linkage

The oxygen atom from the peroxy linkage (≡Si-O-O-Si≡) can leave the initial site, hop to the next Si-O-Si network and form a new linkage by overcoming the diffusion

activation energy, which is 1.28 eV as predicted by our cluster model and 0.8~2.2 eV by the bulk model accounting the variation of the local structure.

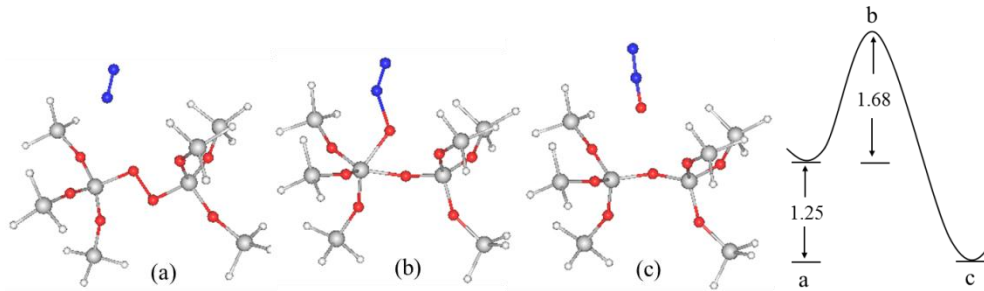


Figure 4.9 Predicted reaction path for formation of a N_2O molecule from a peroxy linkage ($\equiv\text{Si-O-O-Si}\equiv$) and N_2 molecule. The corresponding energy pathway (in eV) is shown.

Recall the result summarized in Section 4.4. N_2 tends to stay as interstitial molecule in bulk $\alpha\text{-SiO}_2$. Thus, during O hopping, N_2 (if nearby) can interact with the atomic oxygen released from the peroxy linkage and form N_2O ($\text{Si-O-O-Si} + \text{N}_2 \rightarrow \text{Si-O-Si} + \text{N}_2\text{O}$); the reaction and energy pathway are shown in Fig. 4.9. As N_2 approaches the peroxy linkage [Fig. 4.9 (a)], it forms a O-N-N chain with the dangling atomic oxygen [Fig. 4.9 (b)]; the weakened Si-O bond distance is increased by 1.88 Å, and the N-N bond distance is increased by 0.01 Å. The O-N-N chain can easily detach from the five-fold coordinated Si and form N_2O , and the perfect Si-O-Si network is restored as shown in Fig. 4.9 (c). The reaction is exothermic by 1.25 eV and the overall activation energy estimated by the cluster model is 1.68 eV; however, this number may increase for reaction taken place in the bulk structure due to the effect of the surrounding network.

4.6.2 Peroxy oxygen radical

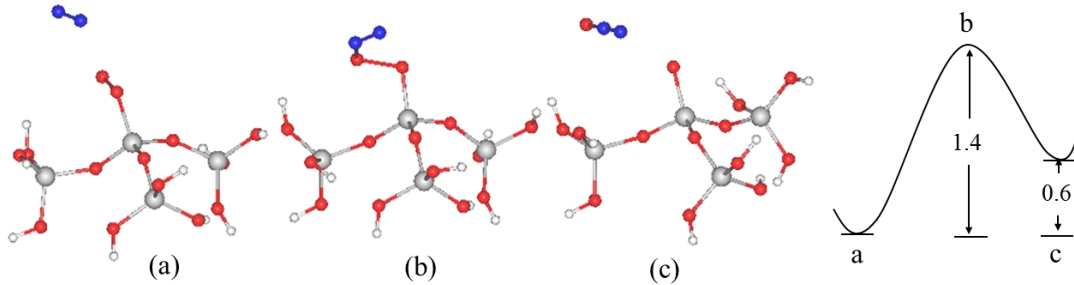


Figure 4.10 Predicted reaction path for formation of a N_2O molecule from a peroxy oxygen radical ($\equiv\text{Si-O-O}\cdot$) and N_2 molecule. The corresponding energy pathway (in eV) is shown.

The reaction and energy pathway for N_2 and POR interaction are shown in Fig. 4.10. As the POR is highly reactive, it can bond with N_2 as shown in Fig. 4.10 (b); in the O-O-N-N chain, the O-N bond distance is 1.40 Å (close to its single bond value), and the O-O and N-N bonds are 0.21 Å and 0.05 Å longer than their original lengths. Since the O-O bond is significantly weakened from the interaction with N_2 , N_2O can break free and leave O behind as shown in Fig. 4.10 (c). The remaining structure, $\equiv\text{Si-O}\cdot$, is called NBOHC (Non-Bridging Oxygen Hole Center). The energy barrier from (a) to (c) is 1.4 eV, which is significantly smaller than the minimum energy required for the formation of N_2O from N_2 and O_2 with 5.4 eV endothermicity.^[71] The reduced activation energy is attributed to $\equiv\text{Si}\cdot$, serving as reaction-assisting defects in $\alpha\text{-SiO}_2$; the same mechanisms are also observed for metal oxo-complexes.^[72] As predicted by the cluster model calculation, N_2O formation can easily occur if N_2 and POR are in close proximity. However, in the bulk $\alpha\text{-SiO}_2$ structure, we have to consider the effect from the

surrounding SiO₂ network, which can impede the preferential approach of N₂ and increase the activation barrier. Based on the reaction pathways shown in Fig. 4.9 and Fig. 4.10, we obtained viable routes for defect assisted N₂O formation from N₂ and O₂. Given that N₂O is a nitride precursor, our speculation provides a possible explanation to the experimental observation that with N₂ trapped interstitially in the oxynitride film, post-annealing in O₂ may lead to further nitridation near Si/SiO₂ interface.

Chapter 5: Formation, Structure, and Bonding of Boron-Vacancy Pairs in Graphene: A First Principles Study

5.1 INTRODUCTION

Graphene, a honeycomb shaped single layer of graphite, has been of great recent interest in science and engineering due to its unique chemical and physical properties. Graphene, carbon nanotubes, and other graphitic carbon nanostructures have been extensively researched for their potential applications in electronics, photonics, hydrogen storage, sensing, and batteries.^[73-81] Of particular importance is to understand how to tune the electronic structure of graphene-based materials through introduction of chemical impurities and/or creation of defects, to obtain their desired physical and chemical properties for any targeted applications.

Boron is one of the most important substitutional dopants for carbon-based materials because of their comparable atomic size with carbon. Boron has one less valence electron than carbon, which can allow for a substantial modification of the electronic and magnetic properties of graphitic systems.^[76,82] Substitutional B in graphene has been experimentally observed through techniques such as X-ray adsorption spectroscopy (XPS) and high-resolution scanning tunneling microscopy (STM).^[83,84] The presence of B in carbon nanostructures allows the selective sensing of harmful NO and NO₂ gases, better Li storage as a battery anode, and enhanced H storage.^[74-80] The effects of B incorporation have also been studied for potential electronics applications.^[85] In addition, graphene often consists of a large number of vacancy defects that can modify the electronic structure to a large extent; for instance, they are known to induce magnetism in otherwise non-magnetic grapheme.^[86-88] Vacancies have been observed

and characterized using advanced microscopy techniques such as transmission electron microscopy (TEM).^[89] It has been shown that single vacancies may undergo migration in graphene with moderate activation energy^[90,91], thereby allowing the vacancy and immobile substitutional dopants to possibly meet. Despite the importance, only a few studies have been performed on the nature and formation of dopant-vacancy complexes in graphene. The structure of some dopant-vacancy pairs has been examined in graphite^[92], however, there is still much to be learned from the study of dopant-defect interactions in graphene.

In this chapter, we present the formation, structure, and electronic properties of boron-vacancy complexes in graphene based on spin-polarized density functional theory (DFT) calculations. First, we look at the atomic and electronic structures of B-doped and undoped graphene sheets, for the sake of reference. Then, we examine possible atomic configurations for a BV pair, and how the BV pairing modifies the electronic structure of graphene as compared to substitutional B and single V cases. Finally, we calculate the viable routes and energy barriers of BV pairing (or dissociation) that occurs through V migration. The improved understanding could offer insight into how to tune the properties of graphene by engineering defects and impurities.

5.2 CALCULATION METHODS

The calculations reported herein were performed on the basis of DFT within the generalized gradient approximation (GGA-PW91)^[31], as implemented in the Vienna Ab-initio Simulation Package (VASP).^[32] The projector augmented wave (PAW) method with a planewave basis set was used to describe the interaction between ion cores and valence electrons.^[48] We used a 112-atom rectangular graphene sheet with dimensions

of $17.0882 \times 17.2654 \text{ \AA}^2$; here, the GGA-optimized lattice constant of 2.467 \AA was employed, which is slightly larger than the experimental value of 2.461 \AA . Periodic boundary conditions were employed in all three directions with a vacuum gap of 10 \AA in the vertical (z) direction to separate the system from its periodic images. During geometry optimization (energy minimization), all atoms were fully relaxed using conjugate gradient method until residual forces on constituent atoms becomes smaller than $3 \times 10^{-2} \text{ eV/ \AA}$. In geometry optimization, we employed a planewave cutoff energy of 408 eV and a $(3 \times 3 \times 1)$ k-point grid in the scheme of Monkhorst-Pack for the Brillouin zone sampling.^[33] To obtain accurate electron density of states (DOS) and charge densities, a gamma centered $(6 \times 6 \times 1)$ k-point mesh was used; the DOS were calculated using the tetrahedron method with Blöchl corrections.^[93] The spin interpolation formula proposed by Vosko *et al.*^[94] was used to estimate magnetic moments. Reaction pathways and barriers were determined using the climbing-image nudged elastic band method (*c*-NEBM) with 6-8 intermediate images for each elementary step.^[34]

5.3 SUBSTITUTIONAL BORON

For the sake of reference, first we calculated how the atomic and electronic structure of graphene changes when one C is replaced with B. The substitutional B exhibits a planar sp^2 -like configuration. As shown in Fig. 5.1 (upper panels), the B-C bond distance of 1.49 \AA [(a)] is greater than the C-C bond distance of 1.42 \AA in the pristine graphene [(b)], which is consistent with STM images reported for B-doped graphite [84]. The longer B-C bond is partly attributed to the larger size of B compared to C; note that the covalent radii of B and C are 0.82 \AA and 0.77 \AA , respectively.^[95] Figure 5.1 (lower panels) shows the electronic structures of B-doped and intrinsic

graphene. The B-doped and undoped graphene sheets turn out to have no net magnetic moment. For pristine graphene [(a)], the valence and conduction bands touch and both bands exhibit conical band dispersion near the Dirac point, where the Fermi level is located. For the B-doped case [(b)], the Fermi level shifts down into the valence band due to hole injection into the π -electron system of graphene; as such, the Fermi level position is a function of B concentration.

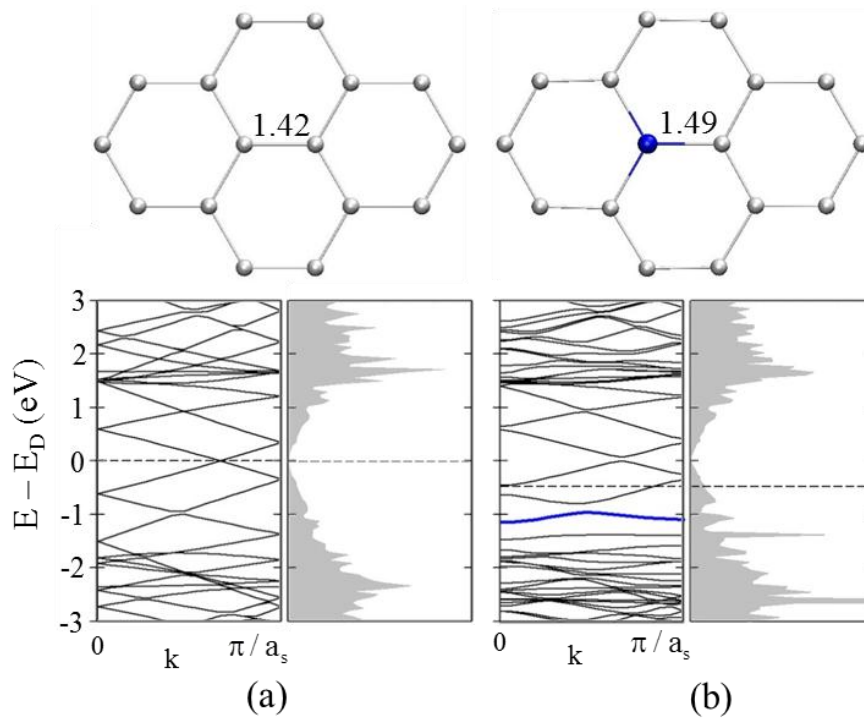


Figure 5.1. Optimized configurations (upper panels) and corresponding electronic band structure and total density of states (DOS) (bottom panels) of (a) pristine and (b) 0.9% boron-doped graphene sheets. Grey and black (blue) balls represent C and B atoms, respectively, and the C-C and C-B bond lengths indicated are given in Å. In each band structure and DOS plot, the Dirac energy (E_D) is set to 0 eV while the horizontal dotted line indicates the Fermi level position. In (b) the B impurity level is indicated by a thick (blue) solid line.

The B p_z orbital is partially filled by the transferred charge, while the B impurity level (thick blue solid line in Fig. 5.1(b)) is located below the Fermi level. Our results are overall in good agreement with previous theoretical studies of B-doped graphene sheets and nanoribbons.^[82,83,96]

5.4 SINGLE VACANCY

Upon removal of one C atom from an intrinsic graphene sheet, each of the three neighboring atoms has one localized sp^2 dangling bond. As illustrated in Fig. 5.2 (a), the following symmetry-lowering lattice relaxation causes two neighboring atoms to form a weak covalent bond (as demonstrated by Wannier function (WF) analysis^[97] in the inset of Fig. 5.2). The remaining unsaturated C atom protrudes out of plane by 0.15Å, due in part to the repulsion between the unpaired and paired electrons. A single vacancy may undergo migration through the transition state as shown in Fig. 5.2 (b); our calculation predicts the migration barrier to be 1.42 eV, within the range 0.9-1.6eV of previous calculations.^[90-92,98] As shown in the electron density of states (DOS) [Fig. 5.3 (a)], the (unpaired) sp^2 dangling bond state is located at 0.4 eV below the Fermi level, and the quasilocalized p_z states caused by the single atom vacancy appear at the Fermi level. The contour plot in Fig. 5.3 (b) illustrates the difference between the majority (up) and minority (down) spin densities of states as shown in the DOS plot [Fig. 5.3 (a)]. Substantial spin differences occur in the localized sp^2 dangling bond state and quasilocalized p_z states, giving rise to ferromagnetism. The total magnetic moment is predicted to be 1.30 μ_B (for 0.9% vacancy concentration), in good agreement with previous studies^[86,87] while the magnetic momentum is likely a function of vacancy concentration.

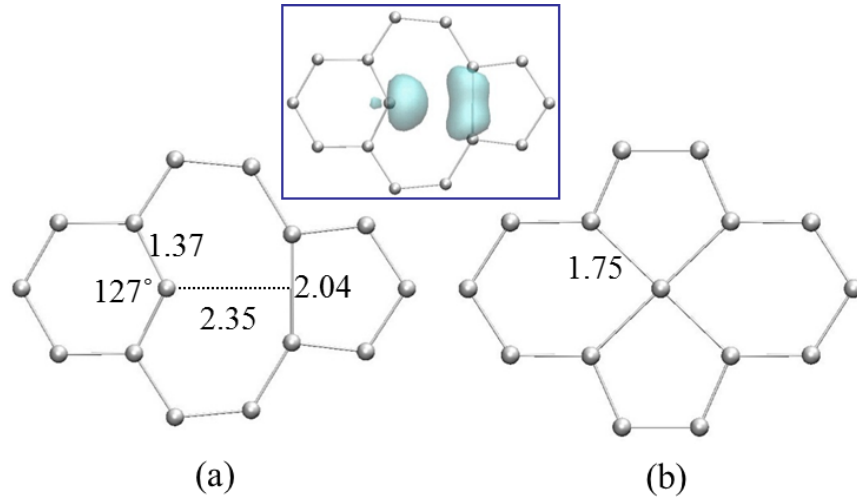


Figure 5.2. (a) Local minimum and (b) (fourfold-coordinated) local maximum configurations of a single atom vacancy; C-C bond lengths indicated are given in Å. In the inset, the unpaired and paired electrons are represented by maximally-localized Wannier functions (with an isosurface value of $0.95 \text{ electron}/\text{Å}^3$), which were calculated using the CPMD package.^[97]

Our calculations also show that the magnetic momentum is sensitive to the weak C-C bond length, although the total energy variation is insignificant with the bond length. As illustrated in Fig. 5.3 (c), when the sp^2 dangling bond is saturated by a hydrogen atom, the C-C bond distance slightly decreases from 1.99 Å to 1.91 Å . The dangling bond termination likely leaves all spins paired; according to our calculations, the anti-ferromagnetic and ferromagnetic ($\approx 0.37 \mu_B$) states are energetically nearly degenerate.

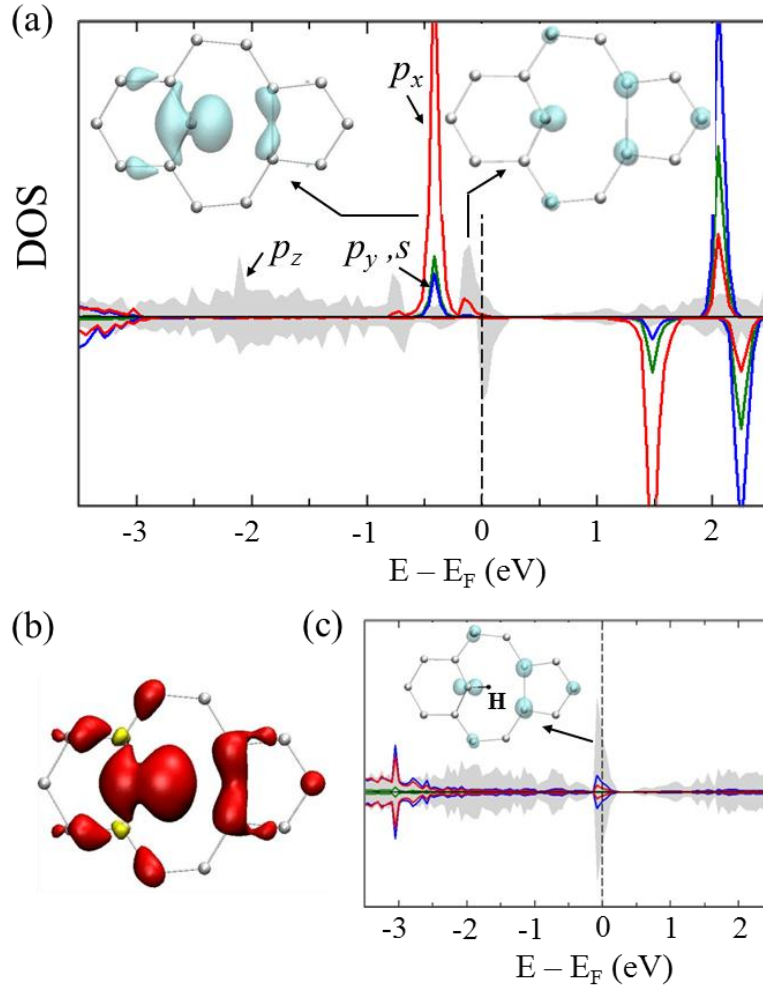


Figure 5.3. Density of states projected onto the s , p_x , p_y and p_z states of the three C atoms surrounding the vacancy site; (a) without and (c) with H termination of the unsaturated sp^2 dangling bond. The shaded grey area represents the p_z states, and the red, blue, and green solid lines indicate the p_x , p_y , and s states, respectively. Band-decomposed charge densities near the Fermi level (E_F) are also plotted with an isosurface value of $0.04 \text{ electron}/\text{\AA}^3$ (based on the total density of states, not shown); (a) $-0.50 \text{ eV} < E - E_F < -0.30 \text{ eV}$ (mainly corresponding to the sp^2 dangling bond state) and $-0.20 \text{ eV} < E - E_F < 0 \text{ eV}$ (mainly the p_z states due to vacancy creation) and (c) $-0.15 \text{ eV} < E - E_F < 0 \text{ eV}$. (b) Spin density difference between the majority (spin up) and minority (spin down) states in (a) [$= \rho(\uparrow) - \rho(\downarrow)$]; the black (red) and grey (yellow) colors indicate the regions with excess majority and minority spin electrons, respectively. The isosurface value is set to $0.02 \text{ electron}/\text{\AA}^3$.

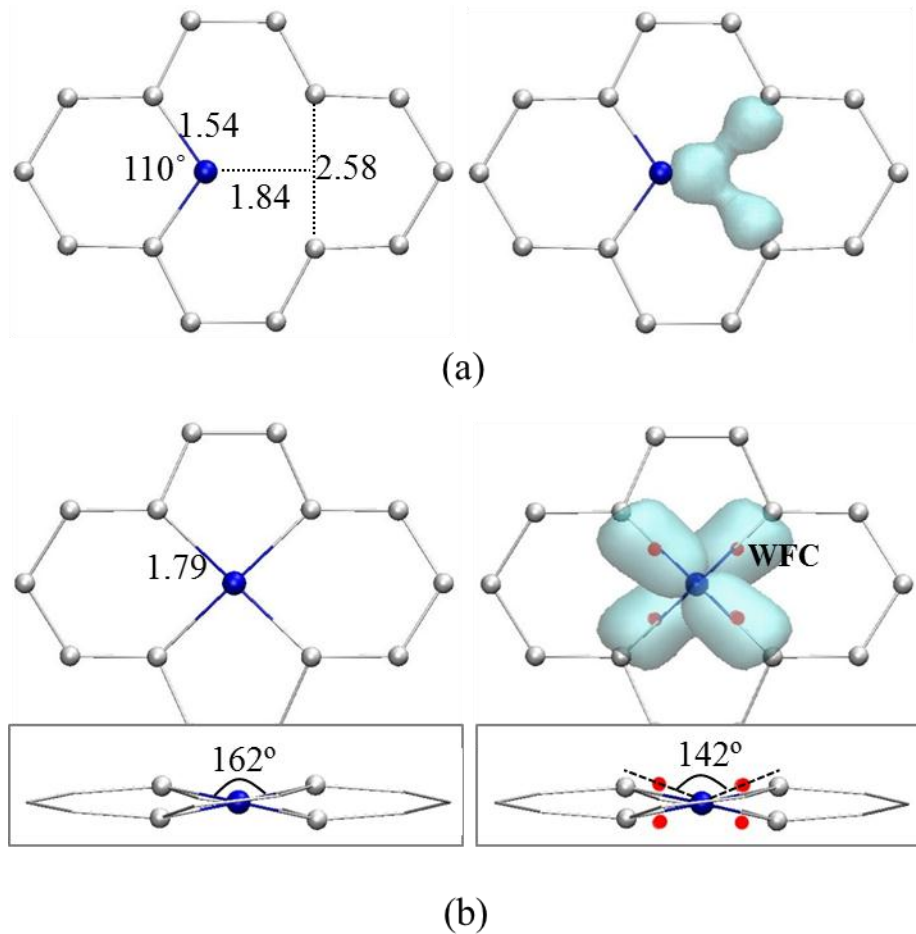


Figure 5.4 Optimized configurations of a BV pair for (a) twofold B and (b) fourfold B states. Grey and black (blue) balls represent C and B atoms, respectively, and the bond lengths indicated are given in Å. The bonding interactions between the B and neighboring C atoms are also represented by maximally-localized Wannier functions (with an isosurface value of $0.95 \text{ electron}/\text{Å}^3$) (right panels). Insets in (b) show the side views of the fourfold-state configurations; small black (red) balls represent Wannier Function Centers (WFCs).

5.5 BORON-VACANCY PAIR

5.5.1 Formation of BV pair

If a mobile vacancy meets with a substitutional B, a BV pair can be formed. As shown in Fig. 5.4 (a) (left panel), when a vacancy is placed adjacent to substitutional B, the distance between two unsaturated C atoms is significantly elongated to 2.58 Å as compared to the vacancy case (1.99 Å). For the BV geometry, the energy gain from pairing is predicted to be 2.21 eV with respect to B and single V. The large C-C distance implies that there is no bonding interaction between them; instead, the C atoms interact with the B atom while they all remain in-plane, as demonstrated by analysis of WFs [Fig. 5.4(a) (right panel)]. Looking at the electron DOS in Fig. 5.5(a), the B sp^2 orbital is fully filled, and it is likely mixed with the partially filled C sp^2 orbitals. The filling of the B sp^2 orbital is somewhat analogous to adduction of an electron donor molecule (such as carbon mono oxide and nitrogen) to the twofold B in a six-membered aromatic ring (such as C_5H_5B where B is highly unstable due to electron deficiency).^[99] The partially saturated sp^2 states of the undercoordinated C atoms are located at the Fermi level, along with the quasilocalized p_z states around the vacancy site, where majority spin electrons exist in excess as demonstrated by the spin density difference plot [inset in Fig. 5.5(a)]. The net magnetic moment is predicted to be about $1.0\mu_B$.

Our calculation predicts that the twofold B state may undergo conversion to the more stable fourfold state with a small energy barrier (≈ 0.06 eV) and a sizable exothermicity (≈ 0.33 eV) [see Fig. 5.4(b)]. As stated earlier, for V the fourfold state [Fig. 5.2(b)] is the saddle point between two adjacent local minima with a saddle-minima energy difference of 1.42 eV. In the fourfold state, the B atom is likely to accept electron, resulting in hole states in graphene [see Fig. 5.5(b)]. Similar to the $[BH_4]^-$ anion, the fourfold B tends to favor a tetrahedral (sp^3) structure as opposed to square-

planar^[100]; however, due to the rest of the in-plane C lattice, a perfect tetrahedron (having C-B-C angles of 109°) is highly unlikely to form.

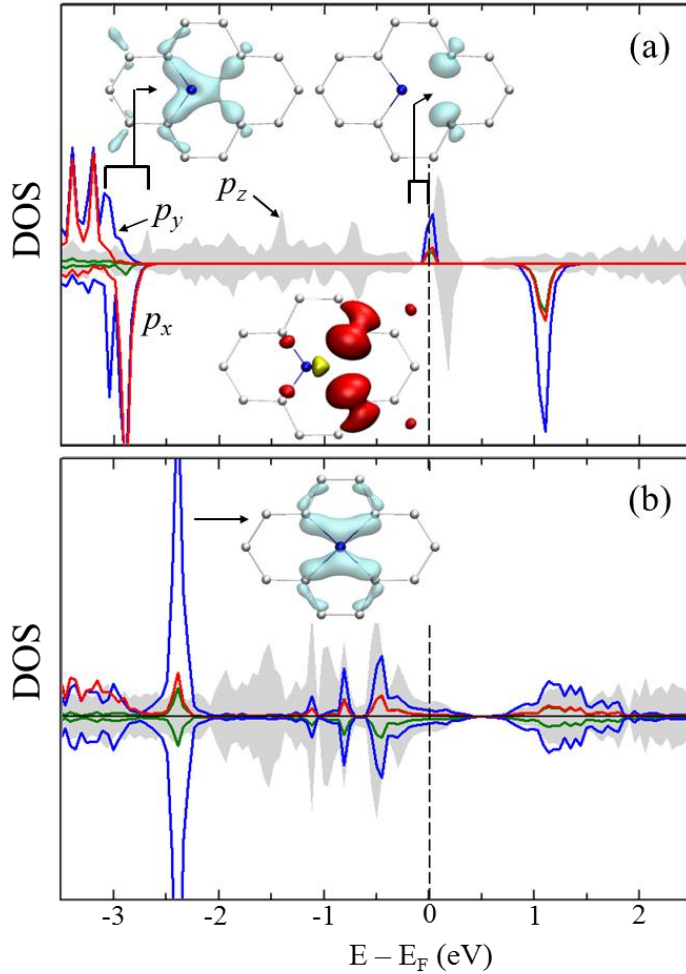


Figure 5.5. Density of states projected onto the s , p_x , p_y and p_z states of the B and nearest C atoms for (a) twofold B and (b) fourfold B states. The shaded grey area represents the p_z states, and the red, blue, and green solid lines indicate the p_x , p_y , and s states, respectively. Band-decomposed charge densities for selected states (as indicated) are also plotted with an isosurface value of 0.09 electron/Å³ (based on the total density of states, not shown). Inset in (a) shows the difference between the majority (up) and minority (down) spin states [$= \rho(\uparrow) - \rho(\downarrow)$] near the Fermi level; the black (red) and grey (yellow) colors indicate the regions with excess majority and minority spin electrons, respectively. The isosurface value is set to 0.03 electron/Å³.

Instead, the fourfold B adopts a distorted tetrahedral configuration where the neighboring C atoms are displaced by $\pm 0.27 \text{ \AA}$ perpendicular to the graphene plane, resulting in C-B-C angles of 162° and WFC-B-WFC angles of 142° . As shown in LDOS [Fig. 5.5(b)], the structural distortion leads to a distinct splitting in the B p_x , p_y and p_z states, instead of sp^3 hybridization as typically seen for a tetrahedron structure. The four B-C bonds are equal in length (1.79 \AA) because of resonance, slightly longer than a single B-C bond (1.65 \AA). Our calculation shows that the fourfold BV structure is nonmagnetic. This suggests that the interconversion between the twofold and fourfold states, which appears to rather easily occur (with moderate barriers of $0.06/0.39\text{eV}$) at elevated temperatures, would induce magnetic moment oscillations (approximately between $1 \mu_B$ to $0 \mu_B$).

5.5.2 B + V \leftrightarrow BV

We examined dissociation of a BV pair by the departure of the mobile V from the B site; in the absence of B, the V migration barrier is predicted to be 1.42 eV , as stated earlier. Figure 5.6 shows variations in the total energy and barrier of V migration in terms of the location of V with respect to B. V migration from site $1'$ to site 2 ($1' \rightarrow 2$) is predicted to occur by crossing a barrier of 1.63eV with a return barrier of 0.56eV . From site 2, the V can further migrate along two different paths (either to site 3 or $3'$) or in the return direction. Although site 3 and $3'$ are comparable in energy, the barrier for $2 \rightarrow 3$ (2.63 eV) is 0.64eV higher than the barrier for $2 \rightarrow 3'$ (1.99 eV). This can possibly be explained by looking at the associated lattice strain (or strain energy) around B. In the $2 \rightarrow 3$ and $2 \rightarrow 3'$ transition states, the average distance between the B atom and the three adjacent C atoms is 1.47 \AA for $2 \rightarrow 3$ and 1.53 \AA for $2 \rightarrow 3'$. When the V is in site 2, the average C-B distance is 1.57 \AA , which indicates that the $2 \rightarrow 3$ transition would require

larger (compressive) lattice strain. The resulting larger strain energy might be responsible for the higher energy barrier in the 2→3 migration. From site 3, the V can move to site 4 with a barrier of 1.90 eV or to site 2' with a barrier of 2.07 eV (note that the transition 3→2' is equivalent to 3→2 due to symmetry). From site 3', the V can move to site 4' with a barrier of 1.53 eV or to site 4'' with a barrier of 1.83eV.

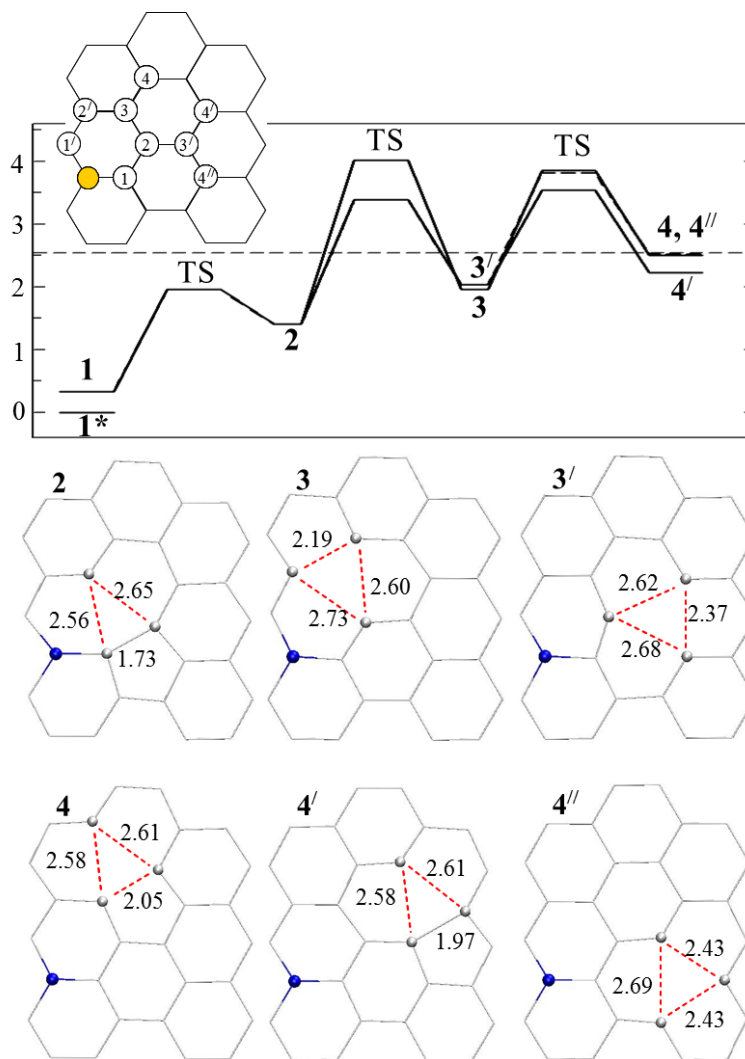


Figure 5.6. Energy variation (in eV) in terms of vacancy location with respect to B, together with corresponding atomic configurations. For the BV pair, 1* refers to the fourfold B state [Fig. 5.4(b)] while 1 and 1' represent the twofold state [Fig. 5.4(a)]. The bond lengths indicated are given in Å.

Once the V is in site 4'', it can migrate back to site 1 continuing on the same circular path or following the reverse direction with the same energy barriers for each step. Sites 4, 4', and 4'' are almost equivalent in energy to the case of completely separate B and V, which means that the V does not feel much effect from the B atom. The results also suggest that if a V in sites 3, 3', or closer would preferentially migrate toward the substitutional B to form a BV pair, rather than move away from the B site. According to the result, one could also expect V-assisted B diffusion via a ring mechanism in which a V moves around a hexagonal ring to the opposite direction (e.g., 1 → 2 → 3 → 2' → 1'); however, the BV pair diffusion tends to be unlikely at moderate temperatures considering the high overall barrier (= 4.03 eV).

5.5.3 BV + V → BV₂

Finally, we looked at how an additional V interacts with the immobile BV pair. As shown in Fig. 5.7(a), when an additional V meets a BV pair to form a BV₂ complex, it can rearrange into the most stable pentagon-octagon-pentagon (5-8-5) structure, as also predicted for a di-vacancy [Fig. 5.7(b)].^[91,101] In the configuration, B prefers to be in a site of greater tensile strain because of its larger size compared to C. The energy gain for BV₂ is calculated to be 6.68 eV with respect to BV and single V. Although further Stone-Wales type rearrangement into another V₂ configuration (consisting of three pentagons and three heptagons), has been predicted to be more energetically favorable than the 5-8-5 configuration, we did not consider the 5-5-5-7-7-7 configuration for BV₂ because of a high energy barrier for the 5-8-5 → 5-5-5-7-7-7 conversion (e.g., ~5.2eV for V₂).^[91] It is now well established that single vacancies can diffuse and coalesce into stable vacancy clusters.^[90,91,101,102] Similarly, our study also demonstrates that B-

multivacancy clusters can be formed by aggregation of single vacancies, suggesting that substitutional B can possibly act as an anchor for vacancy clusters.

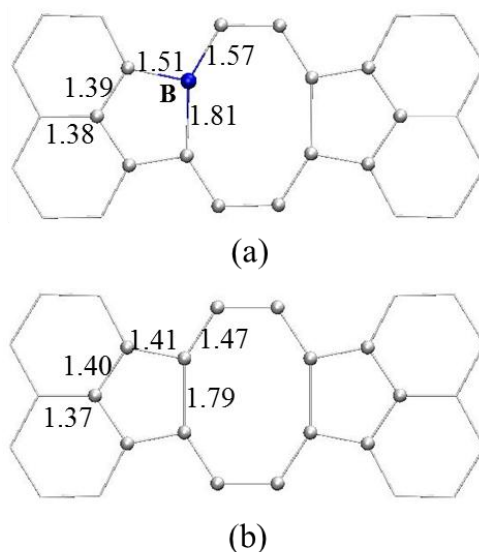


Figure 5.7 Minimum energy configurations of (a) BV₂ and (b) V₂. The bond lengths indicated are given in Å.

5.6 CONCLUSIONS

Based on spin-polarized DFT calculations, we present the formation, structure, and bonding of a BV pair and the effect of BV pairing on the electronic structure of graphene, with comparisons to substitutional B and single V. Our calculations show that a mobile V (with a migration barrier of 1.42 eV) can be trapped by substitutional B to form a BV pair with an exothermicity of 2.44 eV. The B in a BV pair energetically prefers to be fourfold coordinated, rather than twofold coordinated, by adopting a tetrahedral configuration with neighboring C atoms, but highly distorted due to the rest of the in-plane C lattice. However, the moderate energy difference of 0.33 eV between the

fourfold and twofold states may allow their interconversion and consequently magnetic momentum oscillations; the net magnetic momentums of the twofold and fourfold states are predicted to be about $1 \mu_B$ and $0 \mu_B$, respectively. Similar to substitutional B, the fourfold BV pair is likely to accept electron, resulting in hole states in graphene. By looking at the migration pathways and energetics of a single V in the vicinity of substitutional B, we find that a vacancy migrating within a few lattice steps of B is likely to migrate closer to the B and becomes trapped. In addition, when an additional V meets a BV pair to form a BV_2 complex, it can undergo rearrangement into the pentagon-octagon-pentagon (5-8-5) geometry; the predicted exothermicity of the $BV + V \rightarrow BV_2$ combination reaction is 6.68 eV. This study suggests that substitutional B would serve as an anchor for vacancy clusters.

Chapter 6: Boron-Vacancy Pairing and Its Effect on the Electronic Properties of Carbon Nanotubes

6.1 INTRODUCTION

Over the years considerable efforts have been undertaken to take advantage of the unique electrical, mechanical, and thermal properties of carbon nanotubes (CNTs) for the development of energy storage and conversion devices, sensors, and transistors.^[103-106] It is well known that the electronic properties of CNTs are determined by the tube diameter and chirality. In addition, many attempts have been made to tailor their electronic properties by introducing various chemical impurities.^[107-109]

Boron is one of the most important substitutional dopants for sp^2 -bonded carbon materials because of their comparable atomic size with carbon. Boron has one less valence electron than carbon, which can allow for a substantial modification of the electronic and magnetic properties of graphitic systems.^[82,107,110,111] The substitutional doping of boron in CNTs may allow the selective sensing of NO_2 and NH_3 gases, better Li storage as a battery anode, and enhanced H storage.^[112-114] Besides dopants, earlier high-resolution transmission electron microscopy (HR-TEM) measurements have provided evidence of the existence of vacancy-related defects^[115,116] that modify the electronic structure of CNTs to a large extent. The effects of vacancy defects and substitutional dopants on the electrical conductance of CNTs have been rather well studied.^[117-119] However, single vacancies may undergo migration in a CNT with moderate activation energy,^[115,120] possibly leading to the formation of dopant-vacancy complexes that would cause a different electrical behavior from their “pure” counterparts (vacancies and dopants). Despite the importance, some fundamental aspects of the

nature and formation of dopant-vacancy complexes and their influence on the electrical properties of CNTs remain unclear.

In this chapter, using combined density-functional theory (DFT) and nonequilibrium Green's function (NEGF) calculations we examine the formation, structure, and stability of a boron-vacancy pair in armchair CNTs with different diameters, and how the boron-vacancy pairing modifies the CNTs' electronic and charge transport properties with comparisons to isolated vacancy and boron cases. The improved understanding could offer insight into the tailoring of the properties of CNTs through impurity doping and defect engineering.

6.2 CALCULATION METHODS

All the geometry optimization and energy calculations reported herein were performed on the basis of the spin-polarized DFT within the Perdew-Burke-Ernzerhof (PBE) generalized gradient approximation (GGA),^[121] as implemented in the Vienna *ab-initio* Simulation Package (VASP).^[32] The projector augmented wave (PAW) method with a planewave basis set was used to describe the interaction between ion cores and valence electrons.^[48] An energy cutoff of 408 eV was applied for the planewave expansion of the electronic eigenfunctions. CNT structures were modeled using periodic boundary conditions in all three directions; each supercell contains a CNT with 10 unit cells (corresponding to 24.7 Å long according to the DFT-GGA-PBE) in the tube axis and has a vacuum space of 10 Å (perpendicular to the tube axis) between the (periodic image) tubes to avoid their unphysical interactions. All atoms were fully relaxed until residual forces on constituent atoms became smaller than 3×10^{-2} eV/Å.

For Brillouin-zone integration, we employed a $(1 \times 1 \times 3)$ k -point mesh in the scheme of Monkhorst-Pack.^[33]

The electronic transport properties were investigated using the fully self-consistent DFT-based NEGF method, as implemented in the TranSIESTA code.^[122] As illustrated in Fig. 6.1, the calculation system is composed of a central scattering region and two semi-infinite electrodes.

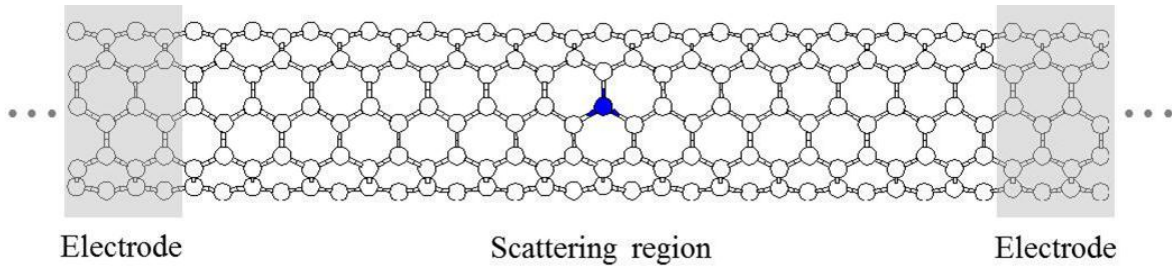


Figure 6.1 Model CNT system employed in electronic transport calculations, consisting of a central scattering region and two semi-infinite electrodes (shaded in grey). Impurities and defects are placed at the center of the scattering region; shown here is a (5,5) CNT with a substitutational boron (in blue).

For a defective system, a defect or impurity was introduced in the scattering region which should be made long enough to screen the defect-induced scattering potential; in our calculations, the axial lengths of the scattering region and each electrode were set to 34.58 \AA and 4.94 \AA (corresponding to 14 units and 2 units), respectively. The electron conductance through a CNT at energy E and external bias V can be expressed by the product of the conductance quantum (per spin) $(=e^2/h)$ and the transmission probability, i.e., $G(E,V) = 2g_0 T(E,V)$.^[123] Within the framework of NEGF, $T(E,V)$ is given by $T(E,V) = \text{Tr}[\Gamma_L(E,V)G^R(E,V)\Gamma_R(E,V)G^A(E,V)]$,^[124] where G^R (G^A) represents the retarded (advanced) Green's function of scattering region and coupling

matrix Γ_L (Γ_R) between the left (right) electrode and the scattering region is the imaginary parts of the lead self-energy.^[125] Here, the spin-polarized DFT calculations were performed within the GGA-PBE, with double ξ -plus-polarization (DZP) basis sets and a real space mesh cutoff of 200 Ry.

6.3 STRUCTURE AND ENERGETICS OF BORON, VACANCY, AND BORON-VACANCY PAIR

We first determined minimum-energy configurations for a substitutional B (B_s), a vacancy (V), and a B_s - V pair in armchair (n,n) CNTs with different tube diameters ($5.6 \text{ \AA} \leq D \leq 9.6 \text{ \AA}$), and also examined how the thermal stability of a B_s - V pair with respect to B_s and V varies with tube diameter.

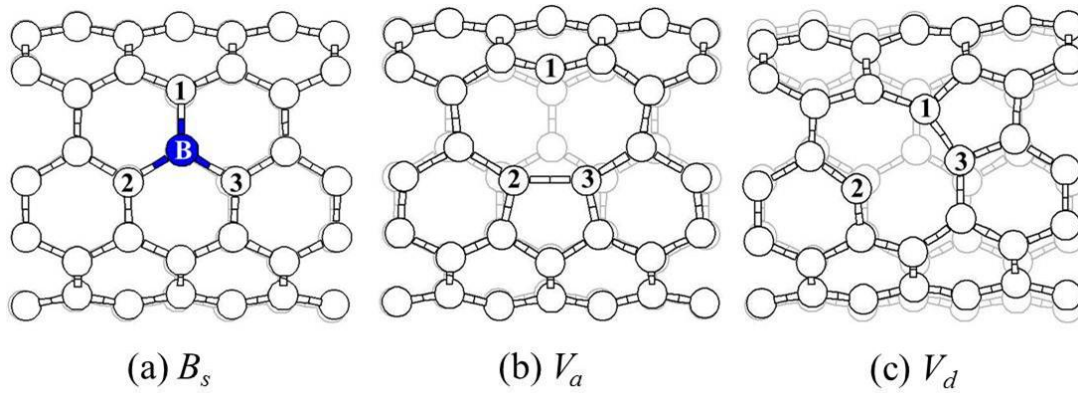


Figure 6.2 Fully relaxed configurations for substitutional B [(a); B_s] and single V with a weak C-C bond along the axial [(b); V_a] and the diagonal [(c); V_d] direction in (5,5) CNT; Each background lattice (in light grey) represents the pristine (5,5) CNT, for comparison. White and black (blue) balls represent C and B atoms, respectively.

Substitutional boron (B_s). — For a small-diameter CNT, the substitutional B atom is displaced outward from the tube wall, due primarily to its larger covalent radius compared to C. For the (5,5) CNT [Fig. 6.2(a)], the outward displacement is predicted to be about 0.2 Å, and the B-C bond lengths are $d_{B-C1} = 1.52\text{Å}$ and $d_{B-C2} = d_{B-C3} = 1.51\text{Å}$ in the radial and diagonal directions, respectively; note that the B-C bond lengths are greater than 1.43Å as predicted for the C-C bond length in the pristine (5,5) CNT, in good agreement with previous studies.^[110,111]

Single vacancy (V). — For a single vacancy, removal of one lattice C atom yields three unsaturated C atoms. Successive symmetry-lowering lattice relaxation causes two adjacent C atoms to form a weak covalent bond while the remaining C atom has one dangling bond. The weak C-C bonding can occur in two different orientations, one along the tube axis [$C2-C3$, Fig. 6.2(b)] and the other diagonal with respect to the tube axis [$C1-C3$, Fig. 6.2(c)]^[126]; the former and latter configurations are referred to as V_a and V_d , respectively, throughout the paper.

In an armchair CNT, the C-C bond preferentially forms in the diagonal direction due to a lesser structural constraint in the radial direction compared to the axial direction [119,126]; note that for the (5,5) CNT (with a diameter of $D \approx 6.9\text{Å}$) the C-C bond in the diagonal direction ($d_{C1-C3}=1.55\text{ Å}$) is shorter than that in the axial direction ($d_{C2-C3}=1.74\text{ Å}$). For the tube curvature, our DFT-GGA calculations predict the V_a and V_d formation energies to be 6.57 eV and 5.57 eV, respectively, in good agreement with previous calculations.^[119,126] Here, the vacancy formation energy is given by:

$$E_f(V) = E_V - (N - 1) \times E_{CNT}/N, \quad (1)$$

where E_V and E_{CNT} represent the total energies of the N -atom CNT with a vacancy and the pristine CNT, respectively.

Substitution B and vacancy pair (B_s-V). — Figure 6.3 shows possible B_s-V configurations we examined. A single V can be placed at two different places adjacent to B_s ; one at the radial [site 1 in Fig. 6.2(a)] and the other at the diagonal direction [site 2 (or 3) in Fig. 6.2(a)]. Our calculations show that the B atom would be either two, three, or fourfold coordinated. If the vacancy is located at site 1 [Fig. 6.2(a)], the B atom would have twofold coordination with the weak bond formation between two unsaturated C atoms in the axial direction ($C4-C9$) [$B_s(Di)-V_a$, Fig. 6.3(a)], threefold coordination with the formation of a weak B-C bond ($B-C4$) in the diagonal direction [$B_s(Tr)-V_a$, Fig. 6.3(b)], or fourfold coordination with the B atom moving radially to a more central location and bonding with all four neighboring C atoms [$B_s(Te)-V_a$, Fig. 6.3(c)]. Among these three structures, the threefold $B_s(Tr)-V_a$ turns out to be the most energetically favorable configuration in the (5,5) CNT.

The relative formation energies of the $B_s(Di)-V_a$, $B_s(Tr)-V_a$ and $B_s(Te)-V_a$ pairs with respect to B_s are predicted to be 6.10 eV, 4.48 eV, and 4.58 eV, respectively; the formation energy is given by

$$E_f(B_s-V) = E_{BV} - (E_B - E_{CNT}/N), \quad (2)$$

where E_{BV} , E_B , and E_{CNT} are the total energies of the N -atom CNTs with a B_s-V pair, a B_s , and no defect/impurity, respectively. If the vacancy is located at site 2 [Fig. 6.2(a)], the B atom would be twofold or fourfold coordinated. In the twofold configuration, a weak C-C bond ($C5-C6$) is formed in the diagonal direction [$B_s(Di)-V_d$, Fig. 6.3(d)]. Unlike the $B_s(Tr)-V_a$ case, the threefold B configuration [$B_s(Tr)-V_d$] is unstable and spontaneously transforms to the energetically more favorable fourfold configuration [$B_s(Te)-V_d$, Fig. 6.3(e)].

In the $B_s(Te)-V_d$ case, the B atom moves diagonally to bond with all four neighboring C atoms; two of the B-C bonds ($B-C1$ and $B-C6$) are approximately in the

radial direction and the remaining two ($B-C3$ and $B-C5$) are approximately in the axial direction. In the distorted tetrahedral structure, the radial B-C bonds ($d_{B-C1} = d_{B-C6} = 1.64\text{\AA}$) are noticeably shorter than their axial counterparts ($d_{B-C3} = d_{B-C5} = 1.83\text{\AA}$). The relative formation energies for $B_s(Di)-V_d$ and $B_s(Te)-V_d$ are 4.55eV and 3.94eV, respectively.

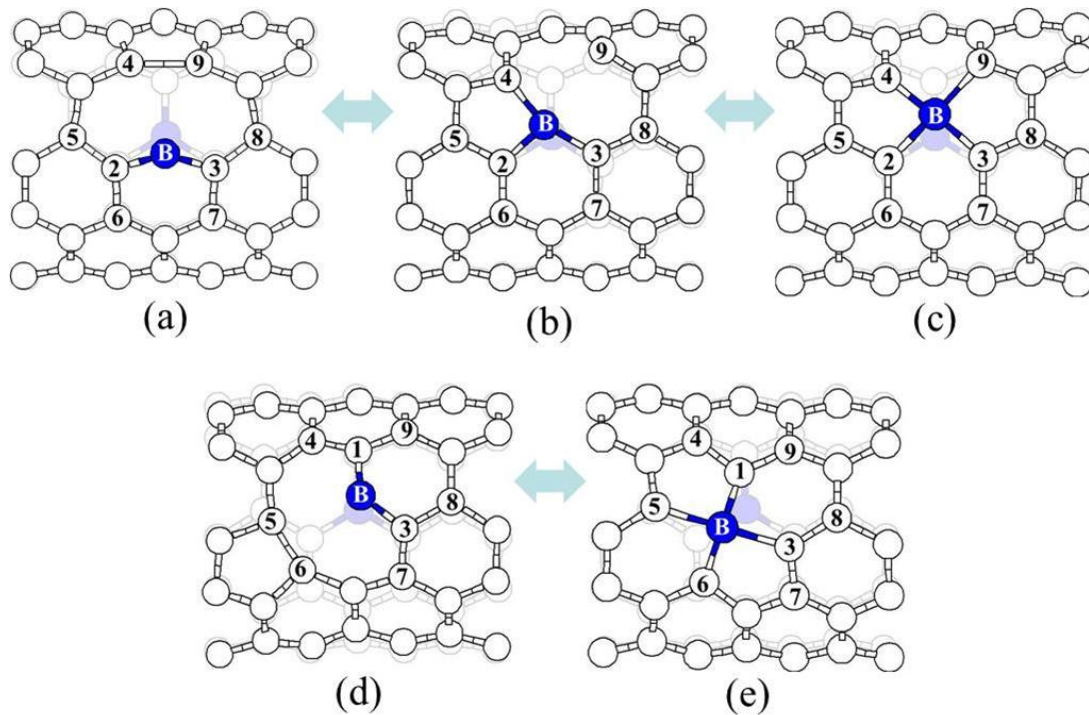


Figure 6.3 Fully relaxed configurations for a B-V pair in different minimum-energy configurations. (Upper panels) a single V is located at $C1$ [in Fig. 6.2(a)]; the B atom could be twofold [(a), $B_s(Di)-V_d$], threefold [(b), $B_s(Tr)-V_d$], or fourfold [(c), $B_s(Te)-V_d$] coordinated. (Lower panels) a single V is located at $C2$ [in Fig. 6.2(a)]; the B atom could be twofold [(d), $B_s(Di)-V_d$] or fourfold [(e), $B_s(Te)-V_d$] coordinated. Each background lattice (in light grey) represents a (5,5) CNT with substitutional B. White and black (blue) balls represent C and B atoms, respectively.

According to the calculation results, the fourfold $B_s(Te)-V_d$ configuration tends to be the lowest-energy structure for a BV pair in the (5,5) CNT. Taking the formation energies of $B_s(Tr)-V_d$ (=3.94 eV) and V_d (=5.57 eV) (i.e., for the most stable B_s-V and V configurations), the energy gain from the B_s-V pairing with respect to fully separated B_s and V is estimated to be 1.63 eV. Given its high stability, the formation of $B_s(Tr)-V_d$ is very likely when B_s and V coexist in a CNT.

CNT diameter effect. — We examined how the structure and stability of B_s , V , and B_s-V are affected by the tube diameter for (n,n) armchair CNTs ($4 \leq n \leq 7$, corresponding to $5.6 \text{ \AA} \leq D \leq 9.6 \text{ \AA}$).

Table 6.1 Selected C-C and C-B bond lengths (d) and C-B-C bend angles (\angle) for relaxed B_s , V , B_s-V geometries for different tube sizes [(n, n) CNTs; $n = 4-7$, corresponding to $D = 5.6-9.6 \text{ \AA}$]. For comparison, the corresponding bond lengths and bend angles in flat graphene (Gr) are also listed. The bond lengths and bend angles are given in \AA and degree ($^\circ$), respectively. See Figs. 6.2 and 6.3 for the atom labels.

(n,n) D	B_s			$B_s(Di)-V_a$		$B_s(Tr)-V_a$			$B_s(Te)-V_a$		$B_s(Di)-V_d$		$B_s(Te)-V_d$	
	d_{B-C1} d_{B-C2}	V_a $dc2-c3$	V_d $dc1-c3$	$dc4-c9$	$\angle_{C2-B-C3}$	d_{B-C4} d_{B-C9}	d_{B-C2} d_{B-C3}	$\angle_{C2-B-C9}$ $\angle_{C3-B-C4}$	$dc5-c6$	$\angle_{C1-B-C3}$	d_{B-C1} d_{B-C3}	$\angle_{C1-B-C6}$ $\angle_{C3-B-C5}$		
(4,4) 5.6	1.53 1.51	1.68	1.53	1.70	137	1.63 2.60			1.55	116	1.63 1.83	125 164		
(5,5) 6.9	1.52 1.51	1.74	1.55	1.83	139	1.66 2.50	1.81 1.66	168 163	1.57	119	1.64 1.83	131 162		
(6,6) 8.2	1.52 1.51	1.78	1.57			1.68 2.41	1.81 1.67	166 163	1.59	119	1.65 1.83	137 161		
(7,7) 9.6	1.51 1.50	1.80	1.58			1.69 2.32	1.80 1.68	164 163	1.60	120	1.66 1.82	140 160		
Gr ∞	1.49	1.99				$d_{B-C} = 1.79$					$\angle_{C-B-C} = 162$			

Table 6.1 summarizes the variations in selected C-C/C-B bond lengths and C-B-C bend angles with the CNT diameter, together with the graphene case (infinite diameter limit) for comparison. As the tube diameter increases, the C-C bond distance d_{C1-C3} in V_d increases from 1.53 Å to 1.58 Å, in good agreement with other calculation result.^[126] For B_s , the B-C distances remain relatively constant with tube diameter.

For the B_s-V pair, the diameter dependence of bond lengths and bend angles varies with its geometry. Looking at the B_s-V_a case, the twofold $B_s(Di)-V_a$ configuration is only stable for small diameter tubes ($n = 4, 5$) and easily converts to the fourfold $B_s(Te)-V_a$ configuration for larger diameters ($n \geq 6$). It is worth noting that for the (5,5) tube the $B_s(Di)-V_a$ configuration [Fig. 6.3(a)] yields a large C-B-C bend angle ($\angle_{C2-B-C3} = 139^\circ$) and a short B-C bond length ($d_{B-C2} = d_{B-C3} = 1.41$ Å); it has structural similarity with borabenzene ($\angle_{C-B-C} = 143^\circ$ and $d_{B-C} = 1.43$ Å from our calculations) in which the B atom is highly unstable and acts as a Lewis acid center.^[99] As the tube diameter increases, the axial bond (d_{C4-C9}) weakens, thereby allowing the electrophilic B to bond with the two C atoms to be fourfold coordinated in tubes with $n \geq 6$. In the threefold $B_s(Tr)-V_a$ configuration, the length of weak B-C bonds [d_{B-C4} in Fig. 6.3(b)] increases from 1.63 Å ($n = 4$) to 1.69 Å ($n = 7$) with increasing the tube diameter; at the same time, the distance between the B and twofold-coordinated C (d_{B-C9}) decreases from 2.60 Å to 2.32 Å. As d_{B-C9} decreases, the strain energy required to form the fourth B-C bond decreases relative to the energy gained through the B-C bond formation. Thus, like the twofold $B_s(Di)-V_a$ case, the threefold $B_s(Tr)-V_a$ becomes unfavorable with tube diameter, as compared to the fourfold $B_s(Te)-V_a$, and cannot exist stably in a nearly flat geometry (the graphene limit). On the other hand, the fourfold $B_s(Te)-V_a$ structure is hardly formed for small diameter nanotubes ($n < 5$). In the $B_s(Te)-V_a$ case [see Fig. 6.3(c)], it is energetically favorable for the two of the four B-C bonds ($B-C3$ and $B-C4$) to be shorter than the other two ($B-C2$

and $B-C9$). This symmetry breaking results in an energy gain from the formation of the two stronger bonds relative to the strain energy associated with the lattice distortion. As the tube diameter increases, the length of the short B-C bonds (d_{B-C3} and d_{B-C4}) increases while that of the longer B-C bonds (d_{B-C2} and d_{B-C9}) remain nearly unchanged; all B-C bond lengths become equal ($=1.79 \text{ \AA}$) in the flat graphene sheet.^[127]

For the case of B_s-V_d , the C-C bond length (d_{C5-C6}) of the twofold $B_s(Di)-V_d$ [see Fig. 6.3(d)] increases from 1.55 \AA to 1.60 \AA as the tube diameter increases from $n = 4$ to $n = 7$. In spite of the elongation, the C-C bond in the diagonal direction [$C5-C6$ in Fig. 6.3(d)] tends to be stronger than that in the axial direction [$C4-C9$ in Fig. 6.3(a)]. As such, the twofold structure likely exists stably for $n > 5$ even though the B-C distances (d_{B-C5} and d_{B-C6}) get shorter; in the flat graphene sheet, however, the increased B-C interaction leads to its transformation with no significant barrier ($\sim 0.06 \text{ eV}$) into the more stable fourfold $B_s(Te)-V_d$ structure.^[127] For the fourfold $B_s(Te)-V_d$ structure, the distorted tetrahedral configuration is likely maintained in large-diameter CNTs; the length of the radial B-C bonds (d_{B-C1} and d_{B-C6} in Fig. 6.3(e)) increases from 1.63 \AA ($n = 4$) to 1.66 \AA ($n = 7$) while that of the axial B-C bonds (d_{B-C3} and d_{B-C5}) remains nearly unchanged at 1.83 \AA . Even in graphene, the fourfold B tends to adopt a distorted tetrahedral configuration where the neighboring C atoms are displaced by $\pm 0.27 \text{ \AA}$ perpendicular to the graphene plane.^[127] This might be attributed to the tendency that the fourfold B favors a tetrahedral (sp^3) structure as opposed to square-planar (sp^2)^[100]; however, due to the rest of the in-plane C lattice, a perfect tetrahedron (having C-B-C angles of 109°) is highly unlikely to form.

Figure 6.4(a) summarizes the calculated formation energies of V and B_s-V at various configurations in terms of tube diameter.

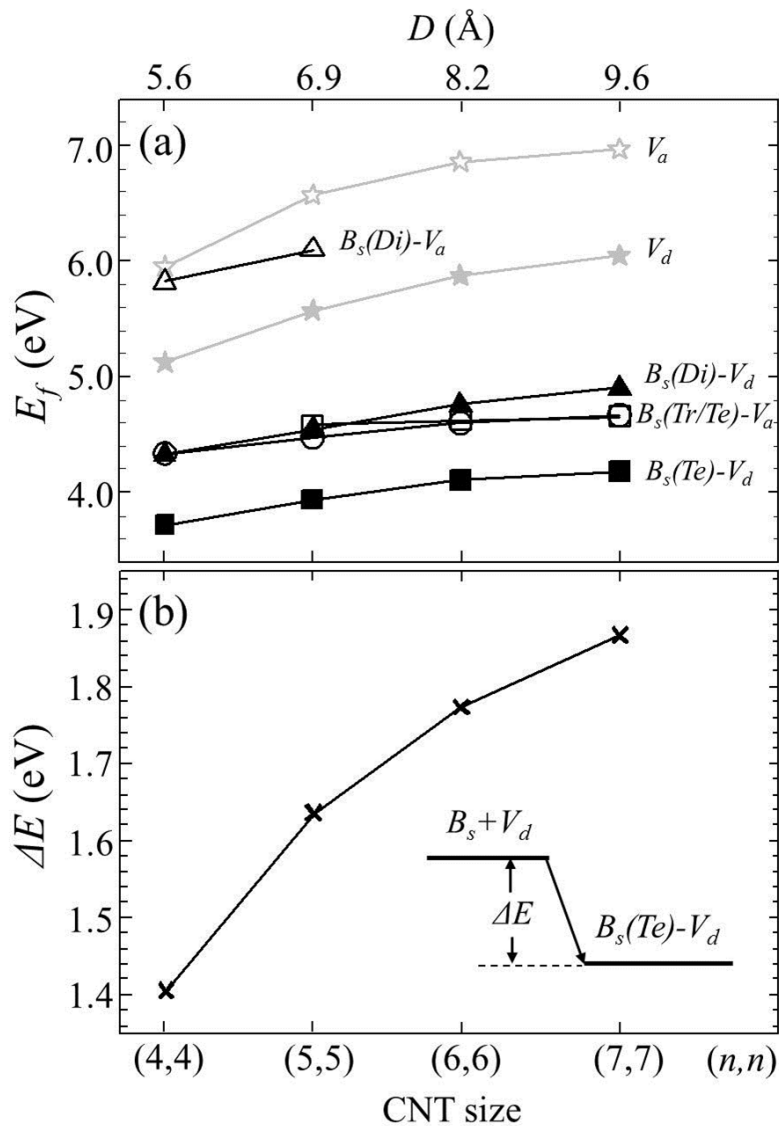


Figure 6.4. (a) Relative formation energies (E_f) with respect to substitutional B for single V and B_s -V pair in different configurations (refers to Figs. 6.2 and 6.3 for the V and B-V labels) and (b) binding energies (ΔE) for $B_s(Te)-V_d$ with respect to fully separated B_s and V_d , as a functions of tube size [(n,n) = tube index, D = diameter].

For all tube diameters examined, the fourfold $B_s(Te)-V_d$ remains the most energetically favorable, while the formation energies increase monotonically with tube diameter. For a single V, the weak C-C bond is stretched with tube diameter (approaching 1.99 Å in graphene as opposed to 1.42 Å for a C-C bond in pristine graphene), leading to the increase of the vacancy formation energy. A similar effect is observed with the BV pair; however, in the $B_s(Te)-V_d$ configuration, the weakening of the shorter B-C bond is less significant. Consequently, the $B_s(Te)-V_d$ formation energy increases less rapidly with tube diameter compared to the single V case, and thus the binding energy of the $B_s(Te)-V_d$ pair increases and can be as high as 2.5 eV in graphene [see Fig. 6.4(b)].

6.4 ELECTRONIC STRUCTURE AND TRANSMISSION

We now turn to examine how the B_s-V pairing modifies the electronic and charge transport properties of CNTs, as compared to the B_s and V cases which have been well studied in the past decade.^[117-119] Figures 6.5-6.7 show calculated spin-polarized conductances for (5, 5) armchair CNTs with B_s , V_d , and $B_s(Te)-V_d$, respectively; in each plot, the corresponding conductance of an defect-free (5, 5) CNT is also presented as a broken line.

In a pristine armchair CNT, two energy bands originating from the π and π^* states intersect at the Fermi level (E_F),^[117] rendering two conducting channels and consequently inducing a conductance (per spin) of $2g_0$ ($= 2e^2/h$) in the vicinity of E_F [i.e., $E_F - 1.5\text{eV} < E < E_F + 1.2\text{eV}$ in the (5, 5) CNT]. The presence of defects or impurities leads to a reduction in conductance due to resonant backscattering. For B_s (in Fig. 6.5), while the up and down spin states are nearly degenerate, the conductance per spin drops from $2g_0$ to g_0 at $E_F - 1.0\text{eV}$ and $E_F - 1.4\text{eV}$ and remains unchanged above E_F .

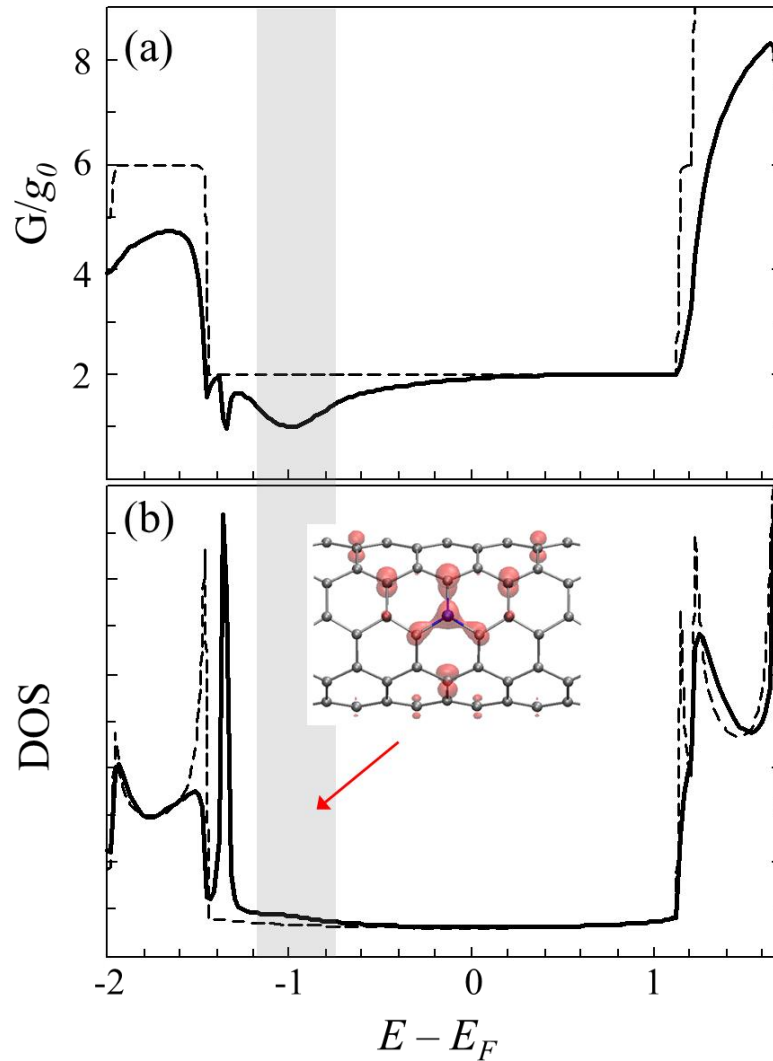


Figure 6.5 (a) Calculated spin-polarized conductance and (b) total DOS for (5,5) CNT with a B_s . Here, the spin-up and spin-down states are degenerate. The inset [in (b)] shows the band-decomposed charge density (with isosurface value of 0.003) within $-1.22 \text{ eV} < E - E_F < -0.74 \text{ eV}$ (shaded in grey), responsible for the corresponding broad dip as shown in (a); C and B atoms are indicated by grey and black (blue) balls, respectively. For comparison, the conductance and total DOS of pristine (5,5) CNT are also presented as broken lines.

The conductance dips are attributed to the quasibound states induced by the B impurity as demonstrated by the electron density of states (DOS) [Fig. 6.5(b)] and the corresponding band-decomposed charge densities (that clearly show the existence of the loosely bound π states in the vicinity of B) [see inset of Fig. 6.5(b)].

Our calculations predict that the minimum-energy configuration of V_d has a finite net magnetic moment ($\mu \approx 0.69 \mu_B$). While the spin states are no longer degenerate, the conductance in Fig. 6.6(a) shows dips at $E_F - 1.4\text{eV}$, $E_F - 1.2\text{eV}$, and $E_F - 0.1\text{eV}$ for the majority spin and $E_F - 1.4\text{eV}$, $E_F - 1.0\text{eV}$, and $E_F + 0.9\text{eV}$ for the minority spin. As stated earlier, the single V structure has an unsaturated C atom while two adjacent C atoms form a weak covalent bond; the σ -orbital on the unsaturated atom is rather strongly localized in nature. The localized σ -orbital and quasilocalized π -orbitals are responsible for the relatively narrow and wide dips, respectively, as can be seen in the DOS and band-decomposed charge density plots [Fig. 6.6(b)].

Upon the formation of the most favorable $B_s(\text{Te})-V_d$ pair that has zero net magnetic moment, the conductance [in Fig. 6.7(a)] exhibits similarity to the B_s case [in Fig. 6.5(a)] while most of the vacancy features likely disappear. This is not surprising considering that the fourfold coordinated B atom likely acts like an acceptor, leading to perturbation of the nearby π states which may cause the wide dip at $E_F - 0.9\text{ eV}$ [see Fig. 6.7(a)]. Unlike the B_s case, an additional narrow dip occurs at $E_F + 1.1\text{ eV}$. The conductance drop is likely attributed to the σ states of the four C neighbors as demonstrated by the DOS and corresponding band decomposed charge density analysis [Fig. 6.7(b)]; Note that the highly distorted tetrahedral BC_4 structure may inhibit the formation of complete single covalent B-C bonds through sp^3 hybridization, as pointed out by a recent theoretical study.^[127]

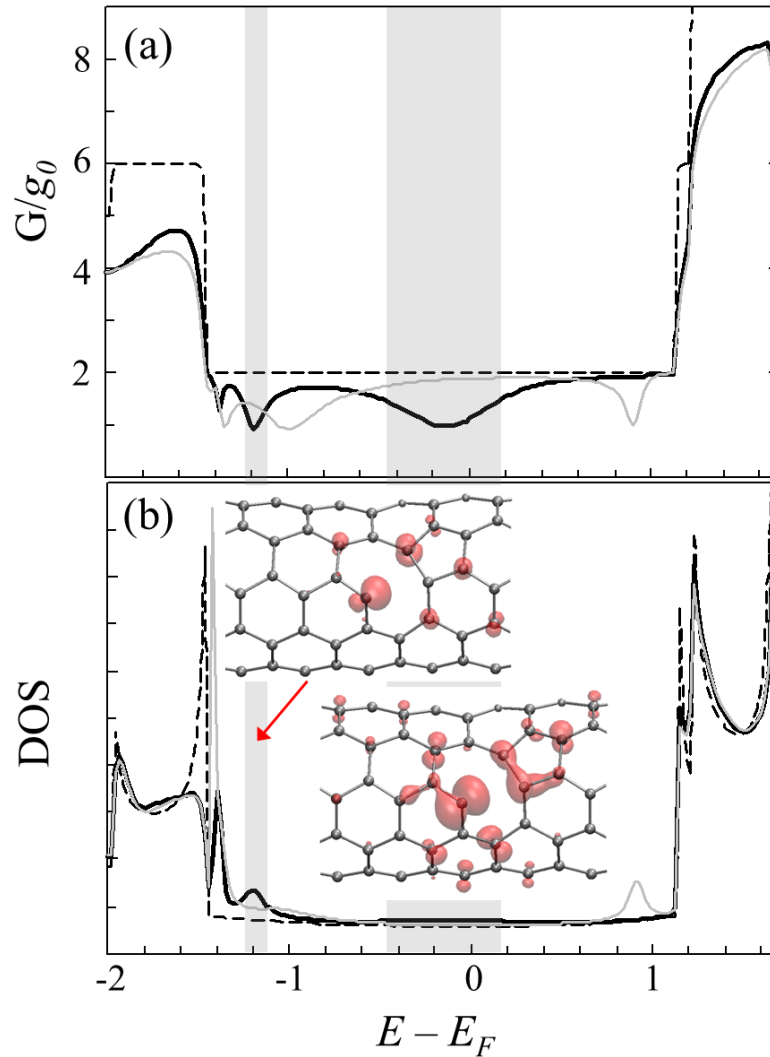


Figure 6.6 (a) Calculated spin-polarized conductance and (b) total DOS of (5,5) CNT with a V_d . The black and grey solid lines indicate the majority (spin-up) and minority (spin-down) states, respectively. The insets [in (b)] show the band-decomposed charge density (for the majority state with isosurface value of 0.003) within $-1.26\text{eV} < E - E_F < -1.07\text{eV}$ and $-0.50\text{ eV} < E - E_F < 0.17\text{eV}$ (shaded in grey), causing the corresponding narrow and broad conductance dips [(a)]. For comparison, the conductance and total DOS of pristine (5,5) CNT are also presented as broken lines.

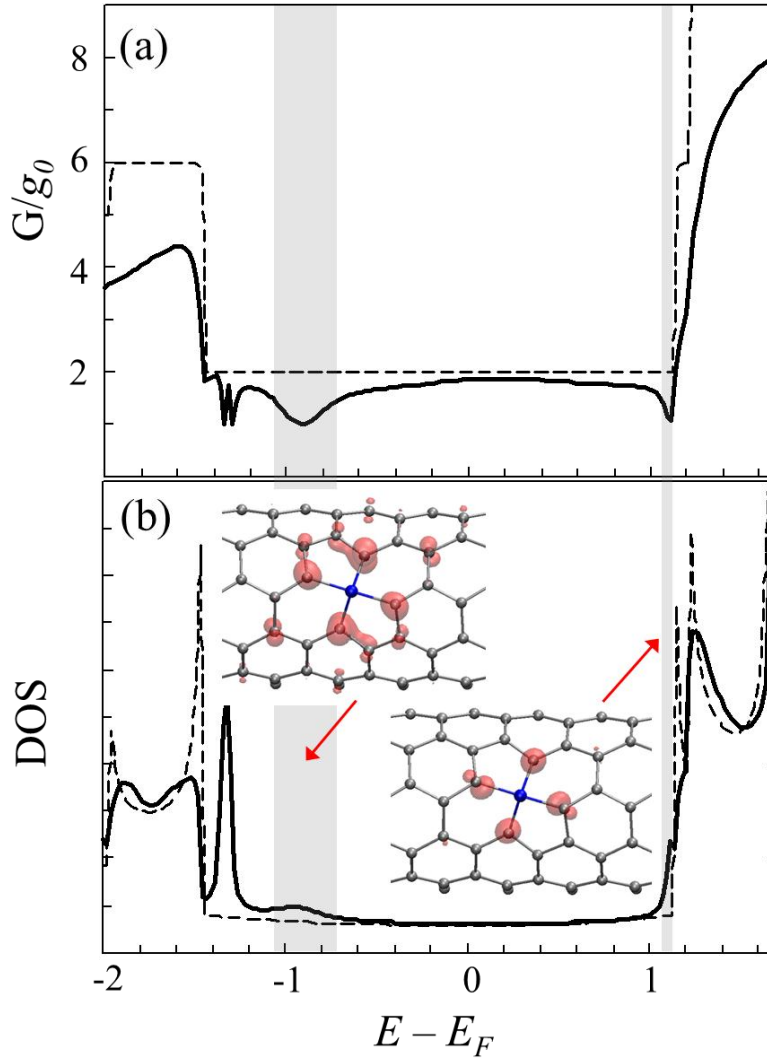


Figure 6.7 (a) Calculated spin-polarized conductance and (b) total DOS of (5,5) CNT with a B-V in the $B_s(Te)-V_d$ configuration. Here, the spin-up and spin-down states are degenerate. The insets [in (b)] show the band-decomposed charge density (with isosurface value of 0.003) within $-1.08\text{eV} < E - E_F < -0.69\text{eV}$ and $1.05\text{eV} < E - E_F < 1.13\text{eV}$ (shaded in grey), causing the corresponding broad and narrow conductance dips [(a)]; C and B atoms are indicated by grey and black (blue) balls, respectively. For comparison, the conductance and total DOS of pristine (5,5) CNT are also presented as broken lines.

6.5 CONCLUSIONS

DFT-GGA calculations were performed to examine the formation, structure, and stability of a boron-vacancy (B-V) pair in armchair (n, n) CNTs with different diameters ($n = 4-7$, corresponding to $D = 5.6-9.6\text{\AA}$). While the B atom in a B-V pair can be two, three, or fourfold coordinated, the fourfold state that saturates the V dangling bonds turns out to be energetically more favorable than the others. The fourfold B tends to adopt a distorted tetrahedral configuration, attributed to its tendency to favor a tetrahedral (sp^3) structure as opposed to square-planar (sp^2). For a small (5,5) tube, the energy gain due to B-V pairing with respect to fully separated B and V is predicted to be 1.63 eV. The B-V formation energy increases with tube diameter, but less rapidly than the single V case; as a consequence, the binding energy of a B-V pair increases and can be as high as 2.5 eV in flat graphene. The high binding strength suggests B-V pair formation to be very likely when B and V coexist in CNTs. The structural changes of B, V, and B-V with tube diameter are described in detail. Using NEGF combined with DFT, we also examined the influence of B-V pairing on the charge transport properties of CNTs with comparisons to the isolated B and V cases. For substitutional B, conductance dips appear at $E_F - 1.0\text{eV}$ and $E_F - 1.4\text{eV}$ due to loosely bound π states in the vicinity of B; whereas a single V defect induces conductance drops at $E_F - 1.4\text{eV}$, $E_F - 1.2\text{eV}$, and $E_F - 0.1\text{eV}$ for the majority spin and $E_F - 1.4\text{eV}$, $E_F - 1.0\text{eV}$, and $E_F - 0.9\text{eV}$ for the minority spin, while localized σ -orbital and quasilocalized π -orbitals are responsible for the relatively narrow and wide dips. Upon B-V formation, the vacancy features mostly disappear while the B features are preserved, suggesting possible ‘pseudo-annihilation’ of V defects, particularly for charge transport, in B-doped CNTs. The fundamental findings would assist in better understanding the effect of impurities and defects on the electronic properties of CNTs.

Chapter 7: Defect-assisted Covalent Binding of Graphene to an Amorphous Silica Surface: A Theoretical Prediction

7.1 INTRODUCTION

Graphene, a two-dimensional hexagonal allotrope of carbon, exhibits unique physical and chemical properties^[128]; its discovery has opened up interesting possibilities for various future technical applications. While production of large-area high-quality graphene sheets is technically very challenging, recently developed transfer printing methods allow for precise patterning of graphene.^[129,130] In this approach, a stamp is used to cut and exfoliate graphene sheets from highly oriented pyrolytic graphite and then place them onto a substrate of interest. Amorphous silica (*a*-SiO₂) is an important support for graphene in various applications^[128,131]; however, the *a*-SiO₂ surface frequently needs to be modified to assist graphene detachment from the stamp and binding onto the *a*-SiO₂ support. Earlier experiments demonstrated that oxygen plasma treatment or chemical functionalization can enhance the interaction of graphene with *a*-SiO₂.^[129] Graphene sheets are also deposited on the defect-free SiO₂ surface^[130], but the weakly physisorbed graphene can easily be removed by solvent washing or sonification.^[132] In addition to immobilizing it, the properties of graphene would be modified by the graphene-SiO₂ binding interaction.

Despite its importance, the interaction between graphene and *a*-SiO₂ is not yet clearly understood, particularly in the presence of defects and chemical functional groups on *a*-SiO₂. While direct characterization of the interfacial interaction currently appears to be rather limited, computational approaches can serve as a power tool. Even so, there have been only a few theoretical studies that mainly focus on crystalline SiO₂ (*c*-

SiO₂).^[133-135] Considering that *a*-SiO₂ might show distinctly different surface properties from *c*-SiO₂ in association with surface defects and strained Si-O bonds, it is necessary to examine the nature of the *a*-SiO₂ surface and the effects of surface modifications on the interaction with graphene.

In this chapter, we present the reaction between graphene and *a*-SiO₂ that contains a dioxasilirane group (DOSG) on the surface, based on density functional theory (DFT) calculations. The existence of DOSG has also been evidenced by experiments^[136]; earlier studies^[137-140] suggested that DOSG can be created by the adduction of molecular O₂ onto the terminal Si of a silylene center, while the silylene center is well known to be an important surface defect in *a*-SiO₂.^[141,142] Minimum energy paths and energetics for the O₂ adduct and graphene binding reactions are determined using a combination of cluster and periodic slab DFT calculations. Modifications in the electronic structure of the DOSG-bound graphene as compared to a free-standing graphene are also examined by calculating electronic density of states.

7.2 CALCULATION METHODS

The calculations reported herein were performed on the basis of DFT within the generalized gradient approximation (GGA-PW91^[31]), as implemented in the Vienna Ab-initio Simulation Package (VASP).^[32] For some selected cases, GGA-PBE^[121] and LDA^[13] calculations were also performed to look at the effect of exchange-correlation functions, as stated later. The projector augmented wave (PAW) method with a planewave basis set was used to describe the interaction between ion cores and valence electrons.^[48] We used a 60-atom rectangular graphene sheet with dimensions of 12.8163×12.3325 Å² in slab calculations and a 72-atom hexagonal graphene sheet in

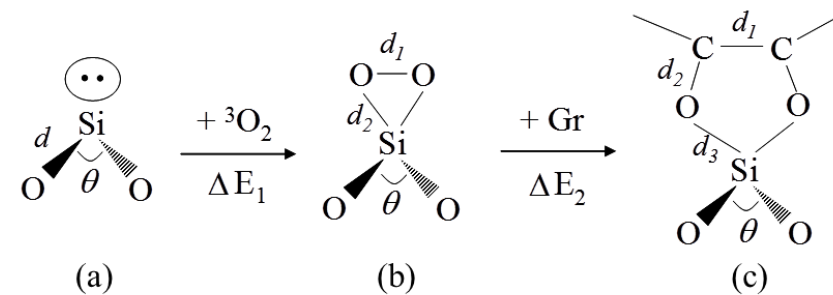
cluster calculations; here, the GGA-optimized lattice constant of 2.467 Å was employed, which is slightly larger than the experimental value of 2.461 Å. The silylene defect on the *a*-SiO₂ surface was modeled using both slab and cluster models. For the slab-model approach, we constructed three *a*-SiO₂ slabs with a thickness of about 10 Å using combined Metropolis Monte Carlo and DFT calculations; each slab consists of 36 SiO₂ units with a silylene center (corresponding to a missing O atom) on the top surface. The slab's lateral (*x* and *y*) dimensions were adjusted to match corresponding graphene dimensions. Further details regarding the construction of *a*-SiO₂ slabs can be found in Refs. [141] and [143]. Periodic boundary conditions were employed in all three directions with a vacuum gap of 8-10 Å in the vertical (*z*) direction to separate the graphene/*a*-SiO₂ system from its periodic images. During geometry optimization (energy minimization), all atoms were fully relaxed using a conjugate gradient method until residual forces on constituent atoms become smaller than 4×10^{-2} eV/Å. In geometry optimization, we employed a planewave cutoff energy of 408 eV and a (3×3×1) k-point grid in the scheme of Monkhorst-Pack for the Brillouin zone sampling^[33], and the increased k-point mesh size up to (12×12×1) to refine the calculations of corresponding electron density of states (DOS) and partial charge densities. A higher cutoff energy of 450 eV and a k-point mesh of (7×7×1) were used for grid-based Bader charge analysis.^[144] The convergence of the atomic and electronic structure calculations was also carefully checked with respect to supercell size. Reaction pathways and barriers were determined using the climbing-image nudged elastic band method (*c*-NEBM)^[34] with 6-8 intermediate images for each elementary step.

7.3 RESULTS AND DISCUSSION

The illustration above Table 7.1 shows a defect-assisted mechanism that we propose for the covalent binding of graphene to the surface of *a*-SiO₂. If a silylene center [(a); (\equiv Si-O)₂Si, where – represents a Si-O bond] exists on *a*-SiO₂, O₂ may easily adsorb on the active silylene site (SS) and form a dioxasilirane group (DOSG) [(b); (\equiv Si-O)₂Si<O₂]. Then, the DOSG may react with two adjacent C atoms in the graphene sheet and form a pentagon ring [(c); (\equiv Si-O)₂Si<(O-C)₂ (indicated as DOSG/Gr hereafter)]. In this work, three independent *a*-SiO₂ slabs (each of which has a SS on the surface) were constructed to consider the strain effects associated with the disordered structure of *a*-SiO₂. For comparison, we also performed cluster calculations that can minimize the strain contribution.

Table 7.1 summarizes the geometric parameters and reaction energies predicted by our GGA-PW91 calculations. Our slab (cluster) calculations predict the overall reaction to be exothermic by 3.96-4.13 (4.34) eV, suggesting that graphene can be strongly bound to the chemically modified *a*-SiO₂ surface by forming Si-O-C linkages. Here we should point out that the DFT slab calculations underestimate the dispersion interaction between the graphene and SiO₂ substrate, and moreover the cluster approach neglects the graphene-SiO₂ interaction; according to the GGA-PW91, the graphene-SiO₂ interaction energy is predicted to be of the order of 1 meV/Å² at the distance of 3.4 Å, which is smaller than half tens meV/Å² as estimated for the corresponding van der Waals interaction.^[131] As such, ΔE_2 values (in Table 7.1) are somewhat underestimated as a result of the tendency of the DFT-GGA calculation to underestimate the long-range dispersion interaction. Next, we discuss each reaction step in detail.

Table 7.1 Optimized geometrical parameters for (a) silylene site (SS), (b) dioxasilirane group (DOSG), and (c) DOSG/graphene (DOSG/Gr) and calculated total energy changes for the SS + O₂ (ΔE_1) and DOSG + Gr (ΔE_2) reactions from cluster and periodic slab DFT-GGA (PW91) calculations. In the slab calculations, three independent slab models were employed. The distances (d) and angles (θ) are given in Å and degree (°), respectively. The energy values (ΔE_1 , ΔE_2) are in eV; the negative sign indicates energy gain during the reaction.



	(a)		(b)		(c)		ΔE_1	ΔE_2
	d	θ	d_1/d_2	θ	$d_1/d_2/d_3$	θ		
SLAB A	1.69	112.3	1.64/1.64	116.3	1.59/1.50/1.64	114.6	-3.16	-0.80
SLAB B	1.69	111.5	1.64/1.64	116.5	1.60/1.50/1.63	115.6	-3.20	-0.93
SLAB C	1.68	106.7	1.64/1.64	112.5	1.58/1.50/1.63	111.5	-3.14	-0.85
Cluster	1.65	102.6	1.63/1.65	107.9	1.60/1.49/1.65	108.2	-3.30	-1.04

Figure 7.1 (left panels) shows the minimum energy configurations of SS, DOSG, and DOSG/Gr determined using SLAB B (see Table 7.1), together with corresponding optimized model clusters (right panels).^[97] For the SS [(a)], the Si-O bond distance and the O-Si-O bond angle slightly vary 1.68-1.69 Å and 107-112° in the slab calculations, while 1.65 Å and 103° in the cluster calculation. The divalent Si in the singlet state has one lone pair which is aligned along the bisector of the O-Si(:)-O angle. Due to the repulsion between the lone electron pairs on Si and O, the Si-O bond tends to be slightly

elongated compared to the calculated mean Si-O bond length of 1.63 Å in bulk *a*-SiO₂. Given that Si prefers *sp*³ hybridization rather than *sp*² hybridization, we can expect that the planar silylene center is highly reactive.^[140]

An O₂ molecule may readily react with the active divalent Si in SS and form a DOSG [Fig. 7.1(b)]; that is, O₂ (triplet) + SS (singlet) → DOSG (singlet). Previous studies^[139,145-147] suggest that the O₂ adduct reaction would follow three steps. Firstly, one end of the O₂ binds to the divalent Si and form a silanone oxide (>Si[•]OO[•], where [•] represents a dangling bond) in which the Si becomes pyramidalized (like a silyl radical, ≡Si[•]) while the Si-bound O₂ (Si-OO[•]) exhibits superoxo (O₂⁻) character. The silanone complex is likely to have triplet diradical character. Secondly, the silanone oxide (>Si[•]OO[•]) undergoes spin conversion to a lower-lying singlet state. Thirdly, subsequent cyclization (or ring closure) leads to the formation of DOSG with a three-membered ring. From our slab (cluster) calculations the overall exothermicity of the O₂ adduction is predicted to be 3.1–3.2 (3.3) eV, consistent with previous theoretical studies that also reported high exothermicities of 2.7–4.1 eV depending on the silylene substituents (such as :SiX₂, X=H, CH₃, Ph).^[138,145,146] In addition, the O₂ adduct reaction tends to occur with no significant activation barrier; for instance, the reaction between SiH₂ and O₂ was observed to occur at 297-600K.^[139]

For the singlet DOSG [(b)], the predicted O-O/Si-O bond distances and O-Si-O bond angle are 1.64 (1.63)/1.64 (1.65) and 113-117° (108°), respectively, from our slab (cluster) calculations, in good agreement with previous calculations.^[138,148] The elongated O-O bond, compared to 1.47Å for peroxy (in HOOH), can be ascribed to the highly strained three-membered ring.^[139,147]

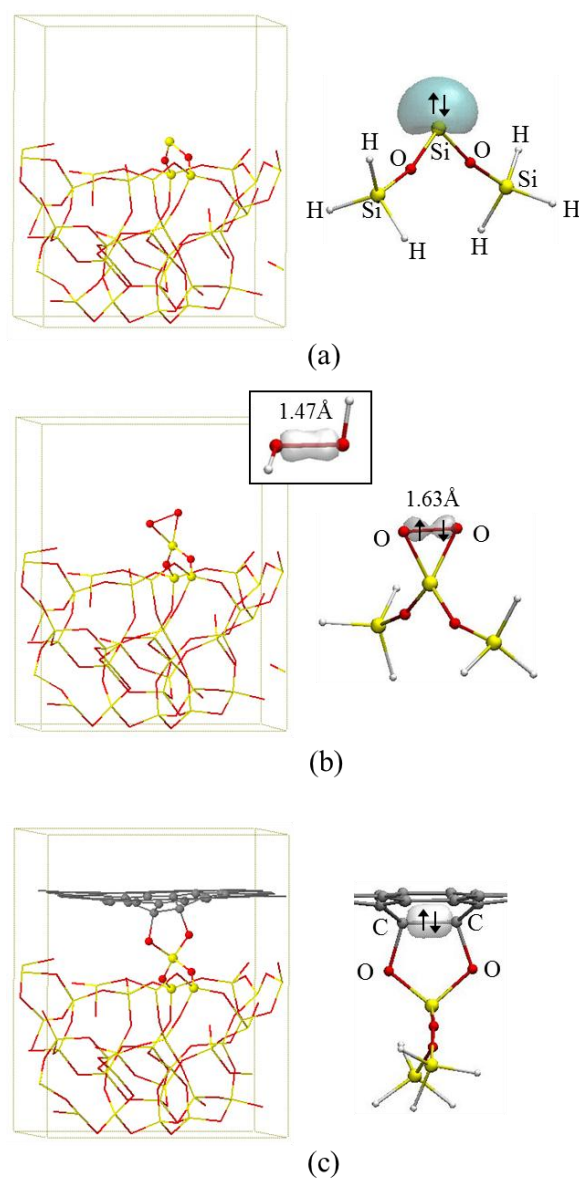


Figure 7.1. Optimized configurations of (a) silylene site (SS), (b) dioxasilirane group (DOSG), and (c) DOSG/graphene (DOSG/Gr) determined using SLAB B (left panels) and model clusters (right panels). The inset in (b) shows a HOOH molecule for comparison. Wireframe represents bulk Si and O atoms in the α -SiO₂ lattice. The lone electron pair in SS [(a)], the O-O bonds in DOSG and HOOH [(b)], and the C-C bond in DOSG/Gr [(c)] are represented by the maximally-localized Wannier functions, which were calculated using the CPMD package. The isosurface values in (a), (b), and (c) are 0.70, 1.94, and 1.40 electron/Å³, respectively. The yellow (light grey), red (dark grey), white (white), and grey balls represent Si, O, H, and C, respectively, as also indicated.

The resulting weakening of the O-O bond is also well demonstrated by the distinctive dumbbell shaped isosurface of the corresponding Wannier function [see Fig. 7.1(b)], as compared to the case of HOOH [inset in Fig. 7.1(b)]. We also estimated atomic charges in DOSG using Bader charge analysis with special care for convergence with respect to charge density grid. The result clearly demonstrates charge transfer to the attached O₂ (approximately 0.8e per O atom), suggesting that the DOSG might have the character of singlet biradicals.^[147]

Next we examined the reaction of DOSG with graphene. As shown in Fig. 7.1(c), a DOSG can be chemically bound to graphene by forming two C-O-Si linkages, resulting in a pentagonal ring analogous to the ethylene reaction with DOSG.^[139] This reaction involves rupture of a π bond in graphene and formation of two C-O bonds; the sp^3 -like C atoms are pulled down by ≈ 0.9 Å and the C-C-O and C-O-Si bond angles are respectively 107° and 113° (from our cluster calculations). As listed in Table 1, the C-C bond length of 1.60 Å is slightly greater than the calculated value of 1.55 Å for a C-C single bond in the tetrahedral diamond lattice.

Figure 7.2 shows a viable route that we have identified for the DOSG + Gr \rightarrow DOSG/Gr reaction using the cluster approach, together with an energy variation along the reaction coordinate. Here, the O₂>Si(OSiH₃)₂ cluster (as shown in Fig. 7.1) was used to mimic the DOSG. Given the singlet initial (A) and final (E) states, the reaction is assumed to occur on the singlet potential energy surface according to the spin conservation rule.^[146] Initially, the graphene was placed 3.3 Å above the O-O dimer of DOSG, close to a typical van der Waals distance. In the initial state [(A)], the DOSG-Gr interaction energy is predicted to be 0.05eV with respect to the fully separated DOSG cluster and graphene sheet [(FS)], while the O-O bond is slightly elongated compared to the isolated DOSG case.

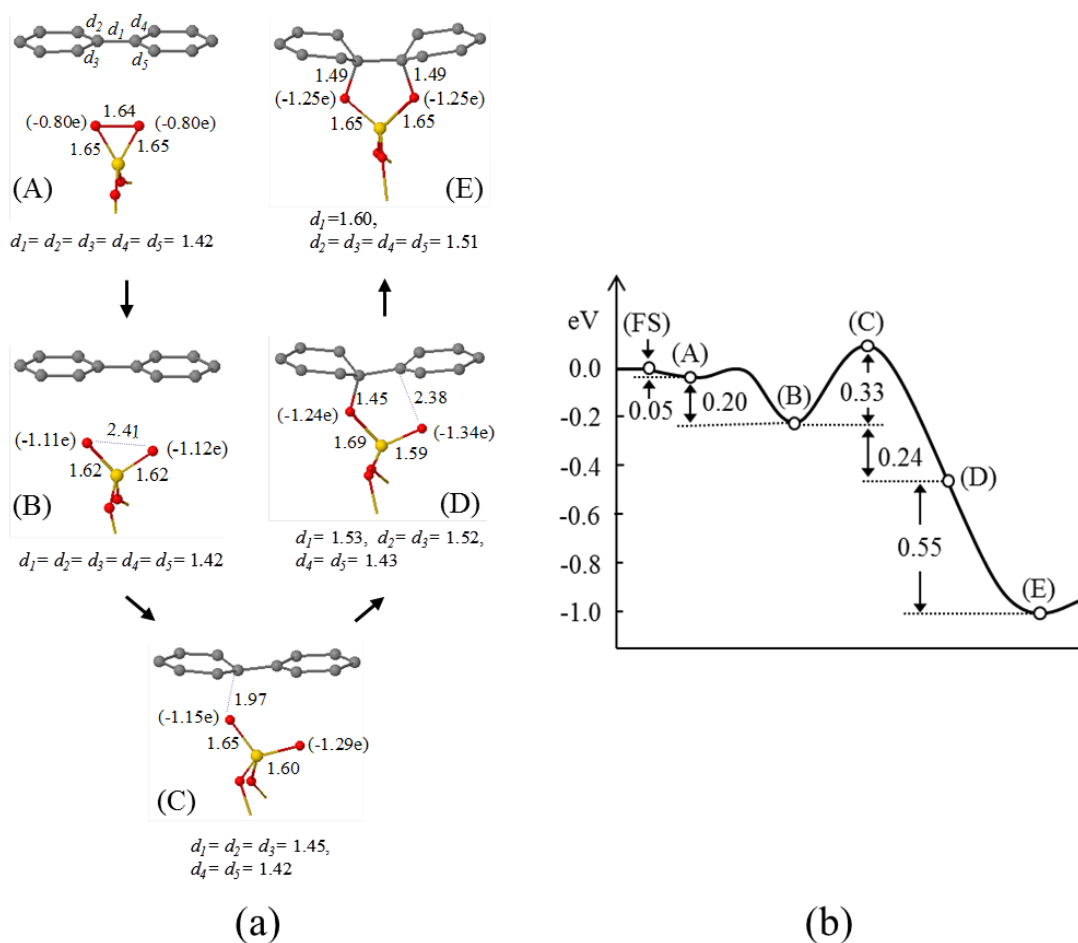


Figure 7.2. (a) Predicted reaction pathway for DOSG binding to graphene and (b) energy variation (in eV) along the reaction coordination from cluster DFT-GGA (PW91) calculations. The selected bond distances are given in Å, and the electronic charges of two terminal O atoms in DOSG are indicated in parenthesis. The yellow (light grey), red (dark grey), white, and grey balls represent Si, O, H, and C, respectively.

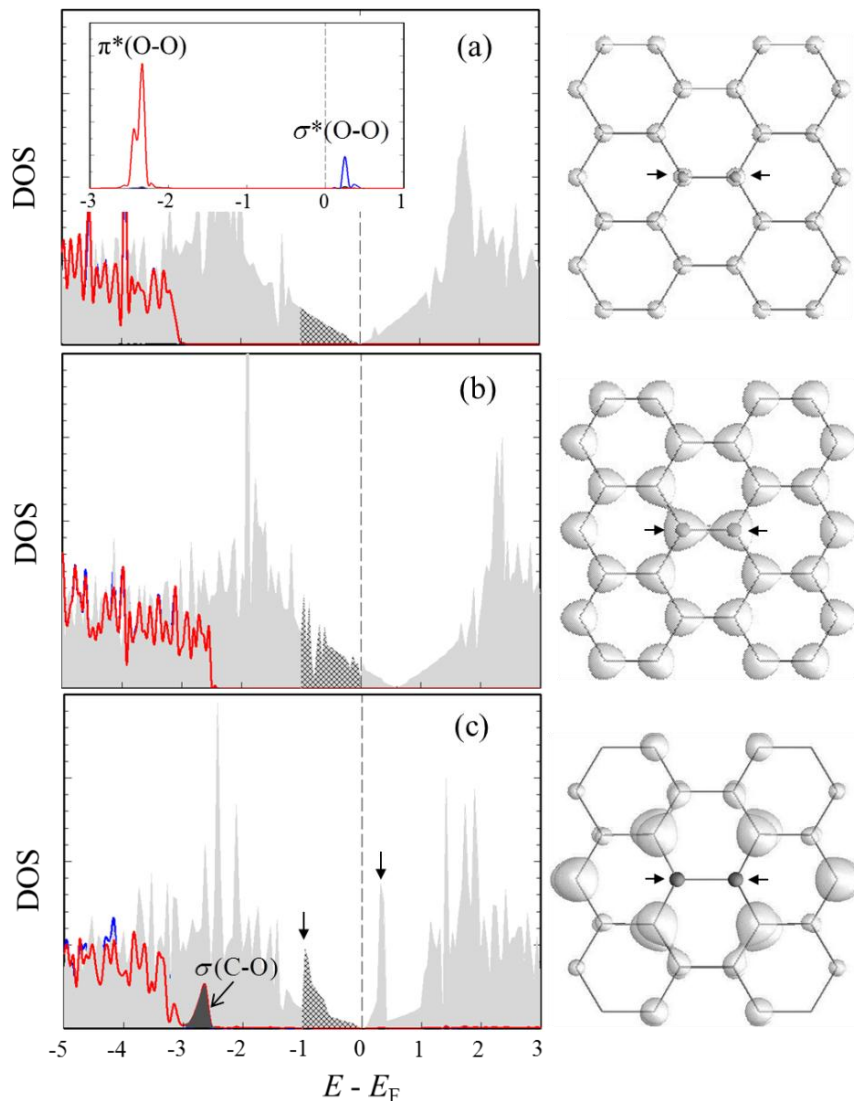


Figure 7.3. (Left panels) Electronic density of states (DOS) and (right panes) isosurfaces of decomposed charge densities corresponding to $E_F - 1 \text{ eV} < E < E_F$ (hatched area) for (a) structure (A), (b) structure (B), and (c) structure (E) in Fig. 7.2. The isosurface value is set to $0.02 \text{ electron}/\text{\AA}^3$. Partial DOS projected on O_2 in DOSG is also presented in the inset of (a), demonstrating that the lowest unoccupied state, $\sigma^*(\text{O-O})$, is located just above the Fermi level of the DOSG + Graphene system. The vertical dotted line indicates the Fermi level position. The grey area represents p_z orbital and the solid (red and blue) lines indicate p_x and p_y orbitals, respectively. The sp^3 C atoms (bonded to DOSG) in graphene are represented by grey balls (also indicated by arrows), while the remaining sp^2 C atoms are by wireframe.

As presented in Fig. 7.3, the electronic density of states (DOS) analysis shows that the lowest unoccupied energy state of DOSG (inset) is located slightly above the valence band edge of pristine graphene [(a)], allowing charge transfer from the graphene sheet to the DOSG. The DOS were calculated using the tetrahedron method with Blöchl corrections.^[149] Our Bader charge analysis predicts the amount of transferred charge to be about $0.3e$ per O atom.

Note that the (transferred) excess charge fills the O₂ 2*p* antibonding orbital, facilitating the O-O bond cleavage [Fig. 7.2 (B)]; in contrast, there exists a sizable barrier in the case of isolated DOSG (e.g., the energy cost for O-O cleavage in H₂Si<O₂ was calculated to about 0.6 eV^[139]). The resulting charge depletion in graphene can be demonstrated by the Fermi level downshift [Fig. 7.3(b)], as typically seen upon hole doping.^[150]

In the following step [(B) → (C)], an O atom in DOSG reacts with a C atom in graphene to form an O-C linkage by crossing a barrier of about 0.33 eV, leading to rupture of a C-C π bond. The barrier was also estimated using the LDA and GGA-PBE; the respective LDA and GGA values are 0.08 eV and 0.36 eV. Subsequently, the second O-C linkage is formed with no additional energy cost [(D) and (E)]. The DOSG + Gr → DOSG/Gr reaction is predicted to be exothermic by 0.79 (0.79, 1.60) eV according to the GGA-PW91 (GGA-PBE, LDA) calculation. It is noteworthy that the LDA has a tendency to underestimate the barrier height and overestimate the binding strength. From our calculations, the moderate activation energy (≈ 0.3 eV) and large exothermicity (≈ 0.8 eV) suggests the feasibility of the DOSG + Gr → DOSG/Gr reaction [(A) → (E)] even at room temperature.

Figure 7.3 also shows how the electronic structure of the DOSG-bound graphene is modified as compared to a free-standing graphene. For a pristine graphene [(a)], the

honeycomb lattice consists of two identical interpenetrating triangular sublattices; each of the C atoms is sp^2 hybridized to form three in-plane σ bonds while their p_z orbitals form π -bonds. The π and π^* bands exhibit a linear dispersion near the Dirac point which is located at the Fermi level. In the DOSG/Gr case [(c)], the sp^3 C atoms (in the C-O bonds) are decoupled from the π -bands, perturbing the π conjugation network in their vicinity. This can be demonstrated by the occurrence of two distinct peaks at -0.9 eV and 0.3 eV in the DOS and corresponding decomposed charge density plots; a similar feature has been predicted upon the adsorption of two impurities on adjacent top sites^[151] or a single impurity (such as S and O) on the bridge site^[152]. The strong C-O bonding state appears about 2.6 eV below the Fermi level. Our calculations also suggest that the DOSG binding results in a possible gap opening (albeit very small) in graphene, and the DOSG/Gr structure is likely to have zero net magnetic moment.

7.4 CONCLUSIONS

The present work demonstrates the possibility of manipulating the nature of the binding interaction of graphene with α -SiO₂ by chemically modifying the α -SiO₂ surface, which might further contribute to tailoring the properties of the supported graphene. If dioxasilirane groups exist on α -SiO₂, our calculations show that graphene can be strongly bound to the modified α -SiO₂ surface by forming Si-O-C linkages (while graphene typically weakly interacts with the defect-free surface via van der Waals forces). Our study also demonstrates that the dioxasilirane group can be easily formed by the adduction of molecular O₂ onto the terminal Si of a silylene center which is an important surface defect in α -SiO₂. The DOSG-graphene binding modifies the graphene electronic properties by perturbing the π conjugation network.

Chapter 8: Structure, Bonding, and Electronic Properties of BiVO₄: A Hybrid Density Functional Theory Study

8.1 INTRODUCTION

Hydrogen is a powerful and clean energy carrier which has about three times more chemical energy than gasoline (123 KJ/g vs. 47 KJ/g) and results in clean by-product (water) when it burns with oxygen. With these merits, hydrogen has been proposed as an alternative energy solution which can replace fossil fuels since the 1970s, due to increasing concerns about environmental pollution, greenhouse gas emissions, and security of energy supply from fossil fuels. Although burning hydrogen for energy generation does not cause any pollution, the same cannot be said of the dominant technology to produce hydrogen, steam reforming from fossil fuels.^[153] Thus, to be a true clean and sustainable energy, hydrogen should be produced from ‘green’ energy sources, such as solar, wind, and geothermal energy.^[154]

Among them, solar hydrogen production by direct water splitting using photocatalysts has attracted significant attention since its first discovery by Fujishima and Honda in the early 1970s.^[155] In their pioneering work, water was split into hydrogen and oxygen under UV irradiation using photoelectrochemical (PEC) cell, in which a titanium dioxide (TiO₂) was used as a photoanode with a platinum cathode. The underlying mechanism for this reaction involves light absorption, photogenerated charge (*e-h*) separation and further migration toward surface reaction sites to oxidize water (i.e. $\text{H}_2\text{O} + 2h \rightarrow 2\text{H}^+ + \frac{1}{2}\text{O}_2$) or reduce proton (i.e. $2\text{H}^+ + 2e \rightarrow \text{H}_2$).^[156] From the first successful water splitting using TiO₂, there have been enormous efforts to find an ideal photoelectrode material for photoelectrocatalytic water splitting.^[157,158]

Metal oxide semiconductors have been recognized as promising photocatalysts for water splitting due to their low production cost and high stability in aqueous environments.^[159,160] Earlier studies mostly focused on binary metal oxides such as TiO₂, Fe₂O₃, and WO₃; they show reasonable photocatalytic performance, but often have inherent limitations.^[160,161] For example, TiO₂ is the most widely used due to its strong redox power, high photocorrosion resistance, and nontoxicity, however its photocatalytic activity is limited to UV radiation due to its large band gap (~3eV).^[162,163] Thus, many PEC researchers have recently turned their attention to ternary metal oxides to expand the search for better visible-light-active photocatalysts for solar-powered water splitting.

Over recent years, bismuth vanadate (BiVO₄) has received much interest as a promising visible-light-active photocatalyst for O₂ evolution in aqueous solutions.^[164-168] BiVO₄ is known to exist in three main crystal structures: tetragonal zircon (*tz*-), tetragonal scheelite (*ts*-), and monoclinic scheelite (*ms*-).^[169] Among them, *ms*-BiVO₄ exhibits the highest photocatalytic activity under visible light irradiation.^[170,171] The lower activity of *tz*-BiVO₄ has been explained by its large band gap (2.9 eV). While *ts*-BiVO₄ and *ms*-BiVO₄ have similar band gaps (2.3eV and 2.4eV, respectively), their main difference is a structural distortion associated with the stereochemically active Bi 6s² lone pair on *ms*-BiVO₄. This implies that correctly describing the monoclinic distortion is important to explain the difference in photocatalytic activity between *ms*-BiVO₄ and *ts*-BiVO₄. Therefore, an important first step in the theoretical investigation of BiVO₄ would be accurate description of structural properties of *ms*-BiVO₄ and *ts*-BiVO₄.

Density functional theory (DFT), the most widely used calculation method for the ground-state electronic structure, is theoretically exact, while for the practical use the exchange-correlation energy in DFT is approximated. Previous DFT calculations have been performed mostly within the local density approximation (LDA) or generalized

gradient approximation (GGA) and shown some satisfying results for solid-state materials. However, DFT calculations within LDA or GGA often result in failure to describe ground state properties of strongly correlated materials, which require more sophisticated functionals for the exchange-correlation energy. A hybrid DFT calculation, in which the fraction of Hartree-Fock (HF) exchange functional is mixed with standard LDA or GGA, has given more accurate description of the structural and electronic properties of metal oxides,^[172] such as ZnO, SrTiO₃, BaTiO₃ and BiFeO₃.^[172-175]

Previous theoretical calculations of BiVO₄ have been performed within standard DFT, which mostly result in difficulties to distinguish *ms*-BiVO₄ from *ts*-BiVO₄. This implies that standard DFT cannot reproduce distinct monoclinic distortion occurred in *ms*-BiVO₄. In this study, we calculate the structural and electronic properties of *ms*-BiVO₄ and *ts*-BiVO₄ based on hybrid DFT calculation. We vary the amount of HF exchange to hybrid functional to obtain optimal degree of HF exchange to properly describe the structural properties of *ms*-BiVO₄. Our hybrid calculation will demonstrate that certain amount of HF exchange results in improvement of description of structural and electronic properties of *ms*-BiVO₄ and *ts*-BiVO₄.

8.2 CRYSTAL STRUCTURE AND BONDING MECHANISM

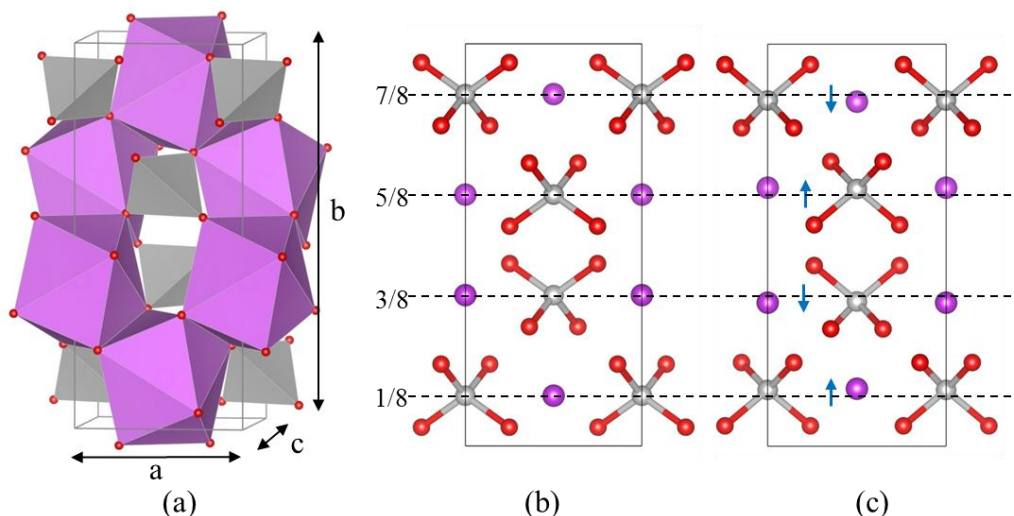


Figure 8.1 Tetragonal scheelite in (a) shows BiO₈ dodecahedra (in purple) and VO₄ tetrahedra (in gray) with a, b, and c axis. Conventional unit cell of (b) tetragonal and (c) monoclinic scheelite BiVO₄. Directions of cation displacement in *ms*-BiVO₄ are indicated by arrows in (c). Purple, silver, and red balls represent Bi, V, and O atoms, respectively. All Bi-O bonds are omitted for clarity.

In the scheelite-type BiVO₄ structure, as illustrated in Fig. 8.1(a), isolated VO₄ tetrahedra (in grey) are corner-connected by BiO₈ dodecahedra (in purple). At ambient conditions, the scheelite-type BiVO₄ structure has been found to exhibit a slight monoclinic distortion, while the crystal structure of many other scheelite-type ABO₄ compounds has tetragonal symmetry (space group $I4_1/a$).^[176 - 180] Earlier experiments^[169,177,178] provided evidence that the monoclinic scheelite structure (*ms*-BiVO₄) may undergo transformation to the tetragonal scheelite structure (*ts*-BiVO₄) at about 255°C or 1.3-1.5 GPa. In *ts*-BiVO₄ [Fig. 8.1(b)], Bi³⁺ and V⁵⁺ cations are located at the centrosymmetric sites of respective BiO₈ and VO₄ polyhedra, giving four

equivalent V-O bonds and two sets of four equivalent Bi-O bonds.^[176,177] In *ms*-BiVO₄ [Fig. 8.1(c)], Bi³⁺ and V⁵⁺ cations are displaced from the centrosymmetric sites along the b-axis (indicated by arrow), lowering the point symmetry of cation sites from *S*₄ to *C*₂.^[176,177] Table 8.1 summarizes the lattice parameters and fractional atomic coordinates as previously reported for *ts*-BiVO₄ and *ms*-BiVO₄.

Table 8.1 Experimental crystallographic parameters for monoclinic (at 4.5K and 295K) and tetragonal (at 566K) BiVO₄ from neutron powder data. The measured atomic fractional positions of all atoms and the bond lengths are also listed. ^aRef. [177], ^bspace group *I2/b* in Ref [177] is transformed to *I2/a*, which makes b-axis unique, ^cnonstandard setting (unique axis b) is used for *ts*-BiVO₄, for easier comparison with *ms*-BiVO₄ having a unique axis-b.

	Monoclinic ^b		Tetragonal ^c
	4.5K ^a	295K ^a	566K ^a
Lattice parameter			
a	5.2146	5.1935	5.147
b	11.7063	11.6972	11.7216
c	5.0842	5.0898	
β	90.394	90.387	
Atomic position			
Bi	(0, 0.636, 0.250)	(0, 0.634, 0.250)	(0, 0.625, 0.250)
V	(0, 0.139, 0.250)	(0, 0.130, 0.250)	(0, 0.150, 0.250)
O1	(0.151, 0.210, 0.510)	(0.147, 0.208, 0.508)	(0.138, 0.203, 0.499)
O2	(0.263, 0.448, 0.381)	(0.261, 0.449, 0.381)	
Bond length			
Bi-O	2.314 × 2, 2.349 × 2	2.354 × 2, 2.372 × 2	2.453 × 4
	2.533 × 2, 2.676 × 2	2.516 × 2, 2.628 × 2	2.499 × 4
V-O	1.74 × 2, 1.75 × 2	1.69 × 2, 1.77 × 2	1.72 × 4

Recent theoretical studies have suggested that the energetically favored monoclinic distortion would be associated with hybridization between Bi 6s, Bi 6p, and O 2p states, as rationalized below.^[159,176] In *ts*-BiVO₄, the coupling between occupied Bi 6s and O 2p states causes bonding and anti-bonding states below the Fermi level. The Bi 6s-O 2p anti-bonding destabilization could be reduced by additional mixing with unoccupied Bi 6p states.^[159,176] The secondary interaction between Bi 6p and Bi 6s (from the anti-bonding state) can only take place in the site with no inversion symmetry, due to symmetry constraints. In *ts*-BiVO₄, the Bi 6s-6p orbital interaction is forbidden since Bi is located in the centrosymmetric site; hence, the Bi lone pair remains spherically symmetric like a pure *s*-atomic orbital and is stereochemically inactive. On the other hand, the off-centrosymmetric distortion in *ms*-BiVO₄ allows the interaction between Bi 6s and Bi 6p states, and thus the Bi lone pair is asymmetrically distributed and becomes stereochemically active.^[181]

8.3 CALCULATION METHODS

The calculations reported herein were performed on the basis of density functional theory (DFT) as implanted in the Vienna *ab-initio* Simulation Package (VASP 5.2).^[32] The projector augmented wave (PAW) method with a planewave basis set was used to describe the interaction between ion cores and valence electrons.^[48] The valence-electron configurations considered are: $5d^{10}6s^26p^3$ for Bi; $3p^63d^34s^2$ for V; and $2s^22p^4$ for O. For each tetragonal and monoclinic scheelite BiVO₄ structure, structural optimization was performed using a conjugated gradient method until residual forces on constituent atoms become smaller than 0.01 eV/Å; here, energy cutoffs of 750eV (cell shape optimization) and 550 eV (atomic relaxation) were applied for the planewave expansion of the electronic eigenfunctions and gamma-centered (4×4×4) Monkhorst-Pack

mesh^[33] of k points was used for the Brillouin zone sampling. To reevaluate corresponding electronic structures, the k-point mesh size was increased up to (6×6×6). All GGA calculations were performed within the Perdew-Burke-Ernzerhof (PBE) generalized gradient approximation (GGA).^[121] In the hybrid functional calculations, a fraction of Hartree-Fock (HF) exchange is added to PBE functional; here, three values for the fraction (α) of HF exchange from 0.10, 0.25 and 0.50 are used. When $\alpha = 0.25$, our hybrid calculation is the same as the screened hybrid functional of Heyd, Scuseria, and Ernzerhof (HSE).^[182] In the HSE functional, the exchange term is split into a short-range and long-range part; to reduce the computational cost, a fraction of HF exchange is only mixed in short-range exchange term, while long-range exchange term is replaced by PBE exchange with no HF exchange. For other values of α , we used the same formula from the HSE functional, but changed the fraction of HF exchange based on chosen α .

8.4 RELATIVE PHASE STABILITY AND LATTICE PARAMETERS: TETRAGONAL VS. MONOCLINIC

We first looked at the relative thermodynamic stability between *ms*-BiVO₄ and *ts*-BiVO₄ as a function of unit cell volume for different exchange correlation (XC) functionals. From a thermodynamic point of view, the relative stability between two systems can be determined by their Gibbs free energy difference ($\Delta G = \Delta E + P\Delta V - T\Delta S$); for a given volume (i.e., $\Delta V = 0$), we simplified the calculations by only considering the difference of internal energy (ΔE) at 0K.

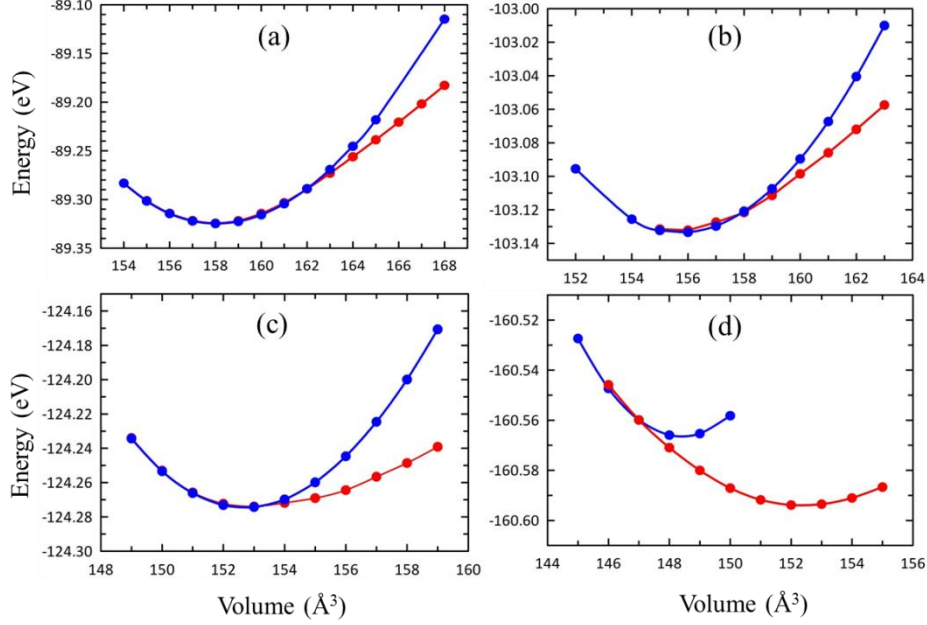


Figure 8.2 The total energy of BiVO_4 (in eV per a primitive unit cell) as a function of the volume (in \AA^3) from (a) PBE, (b) HF10%, (c) HF25%, and (d) HF50% calculations. Two phases, $ts\text{-BiVO}_4$ (blue symbols) and $ms\text{-BiVO}_4$ (red symbols), are considered for each case.

Figure 8.2 shows calculated energy-volume (E - V) curves for PBE [(a)] and hybrid functionals with different fractions of exact HF exchange [(b) HF10%, (c) HF25%, (d) HF50%]. For each volume, starting with the experimental atomic coordinates (as listed in Table 8.1), the cell shapes and fractional coordinates of $ts\text{-BiVO}_4$ and $ms\text{-BiVO}_4$ were allowed to relax under the fixed volume constraint. Above the crossover volume (V_C), there is a continuous transformation from $ts\text{-BiVO}_4$ to $ms\text{-BiVO}_4$ with increasing volume. Given the inverse relationship between pressure and volume, our calculation result clearly demonstrates the occurrence of monoclinic-to-tetragonal phase transition with pressure increase (or volume decrease); this is consistent with the experimental evidence of the pressure-induced second-order phase transition from $ms\text{-BiVO}_4$ to $ts\text{-BiVO}_4$.^[178]

While the phase transition behavior is generally consistent with earlier experimental observations, it is interesting to note the sensitivity of V_C to the HF exchange weight. The relative crossover volume (V_C^*) with respect to the ts -BiVO₄ equilibrium volume (V_0^t), given by $V_C^* = (V_C - V_0^t)/V_0^t$, decreases from 0.032, 0.013, 0.003 to -0.007 with increasing the fraction of HF exchange from 0%, 10%, 25% to 50%, respectively. Here, V_0^t is obtained by fitting a set of the E - V data to a third-order Birch-Murnaghan equation of state.^[183] Recall that the ms -BiVO₄ \rightarrow ts -BiVO₄ transition may occur under compressive stress conditions (1.3-1.5 GPa), according to previous experimental observation.^[178] To comply this, V_C^* needs to be negative, which suggests that hybrid functionals with a sizable fraction of HF exchange would be required to properly evaluate the relative stability between ts -BiVO₄ and ms -BiVO₄.

In Table 8.2, we summarize calculated structural factors (a , b , c and β), bulk moduli (B_0), and equilibrium volumes (V_0) for the ts -BiVO₄ and ms -BiVO₄ phases for different HF exchange fractions. For ms -BiVO₄, only HF25% and HF50% results are reported because PBE and HF10% are not sufficient to yield the respective equilibrium configurations, instead ms -BiVO₄ tends to merge to ts -BiVO₄ (see Fig. 8.2). With increasing the HF exchange weight, the monoclinic angle (β) increases; the β of 90.36° in the HF25% optimized ms -BiVO₄ structure is close to the experimental value of 90.38°, whereas HF50% (β =90.81°) tends to overestimate the lattice distortions.

Table 8.2 Optimized lattice parameters of tetragonal and monoclinic BiVO₄ from corresponding calculations (PBE, HF10%, HF25%, and HF50%). The bond lengths (Bi-O and V-O) are also summarized.

Tetragonal		PBE	HF 10	HF 25	HF 50
Lattice constant	a	5.178	5.155	5.121	5.076
	b	11.784	11.724	11.647	11.521
Bond length (Å)	Bi-O	2.454 × 4	2.444 × 4	2.431 × 4	2.414 × 4
	V-O	2.507 × 4	2.496 × 4	2.481 × 4	2.456 × 4
Vol (Å ³)		158.0	155.8	152.7	148.4
<i>B</i> ₀ (Gpa)		122.1	128.5	138.2	156.4
Monoclinic		HF 25	HF 50		
Lattice constant	a / c	5.183 / 5.074	5.197 / 5.006		
	b	11.711	11.722		
	β	90.36	90.81		
Bond length (Å)	Bi-O	2.378 × 2, 2.384 × 2	2.283 × 2, 2.335 × 2		
	V-O	2.485 × 2, 2.619 × 2	2.527 × 2, 2.729 × 2		
Vol (Å ³)		154.0	152.5		
<i>B</i> ₀ (Gpa)		56.3			

Concomitantly, the difference between *a* and *c* increases with HF exchange fraction, while *a* = *c* and β = 90° in *t*-BiVO₄; note that the monoclinic distortion is associated with the displacement of Bi from the centrosymmetric site, yielding *a* ≠ *c* and β > 90°. In comparison, previous conventional DFT calculations^[159,184,185] yielded β ≈ 90° and *a* ≈ *c* for *ms*-BiVO₄, which is consistent with our calculations from which the *ms*-BiVO₄ structure nearly merges to the *ts*-BiVO₄ structure upon structural relaxation with PBE (see Fig. 8.2). Our calculations also predicts the *B*₀ of *m*-BiVO₄ to be greater than that of *t*-BiVO₄, which is consistent with existing experimental measurement^[178] and also

show that B_0 increases and V_0 decreases with increasing the degree of HF exchange, as also reported by previous hybrid-DFT calculations.

8.5 ELECTRONIC STRUCTURE DESCRIPTION: CONVENTIONAL VS. HYBRID DFT

To gain a better understanding of the XC functional dependence of the structural stability, we investigated how the inclusion of exact HF exchange affects the description of bonding in *ts*-BiVO₄ and *ms*-BiVO₄, through analysis of Bader charges and charge density differences.

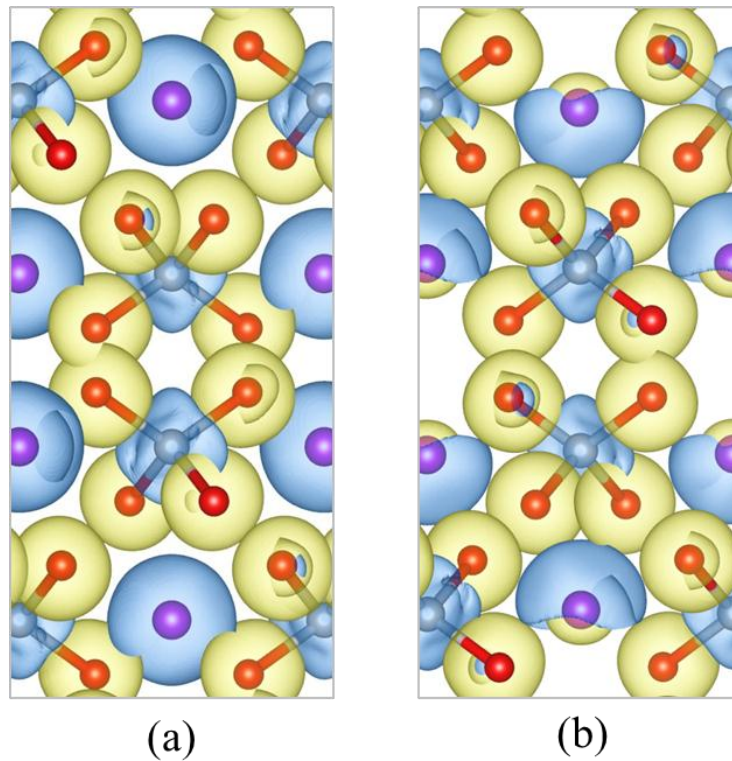


Figure 8.3 Charge density difference ($\Delta\rho = \rho^{\text{HF50}} - \rho^{\text{PBE}}$) isosurfaces ($\pm 0.022e/\text{\AA}^3$) of (a) *ts*-BiVO₄ and (b) *ms*-BiVO₄. Yellow (blue) regions corresponds to an positive $\Delta\rho$ (negative $\Delta\rho$). Purple, silver, and red balls represent Bi, V, and O atoms, respectively. All Bi-O bonds are omitted for clarity.

In Fig. 8.3, the isosurface plots show the differences between the charge densities from the HF 50% and PBE calculations (i.e., $\Delta\rho = \rho^{HF50} - \rho^{PBE}$) for (a) *ts*-BiVO₄ and (b) *ms*-BiVO₄; the HF 50% case was chosen, rather than HF 10% or 25%, to demonstrate more clearly the HF exchange contribution. The blue and pink isosurfaces represent charge gain ($\Delta\rho > 0$) and charge loss ($\Delta\rho < 0$), respectively. Here, we used the BiVO₄ configurations optimized with HF50%. For both *ts*-BiVO₄ and *ms*-BiVO₄, the plots of $\Delta\rho$ clearly demonstrate that the charge gain of O anions is enhanced while the charge on V and Bi cations is more depleted upon the inclusion of exact HF exchange to the PBE functional. The increased charge transfer between the cations and anions is expected to increase the ionicity of BiVO₄. According to the grid-based Bader analysis^[186] we performed (see Table 8.3), in *ts*-BiVO₄ the O charge state is predicted to change from -1.04 (in PBE) to -1.17 (in HF50%) while V/Bi cations become more positively charged (+2.11/2.05 \rightarrow +2.42/2.27); a similar result is obtained for *ms*-BiVO₄. The Bader volume is also found to increase (or decrease) as the charge gain (or loss) is enhanced, which is consistent with the general trend that ionic radius increases (or decreases) with increasing negative (or positive) charge.

Table 8.3 Calculated Bader Charges (Q_B) and Volumes (V_B) of Bi, V, O atoms in *ts*-BiVO₄ and *ms*-BiVO₄ from HF50% calculation. Values in parentheses in table indicate calculated values from PBE calculation at the fixed geometry (obtained from HF50%).

	Q_B	V_B		Q_B	V_B
Bi	+2.27 (+2.05)	15.48 (16.16)	Bi	+2.25 (+2.04)	16.15 (16.80)
V	+2.42 (+2.11)	6.76 (7.23)	V	+2.41 (+2.11)	6.84 (7.32)
O	-1.17 (-1.04)	12.99 (12.70)	O1	-1.09 (-0.97)	13.87 (13.60)
			O2	-1.24 (-1.10)	12.75 (12.46)

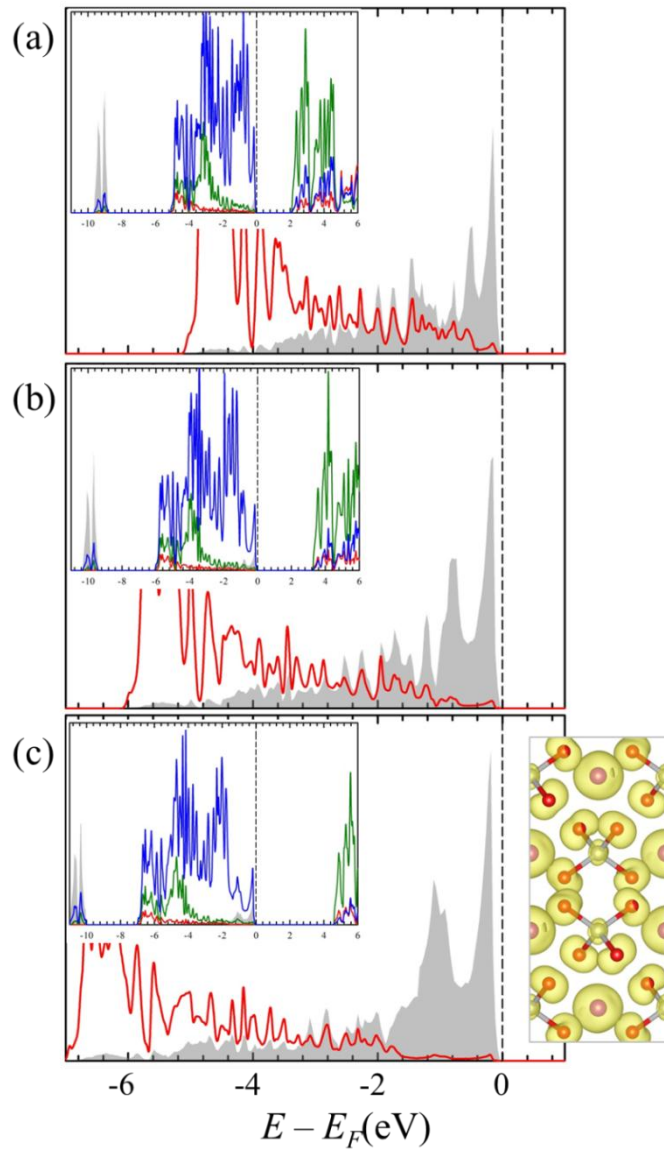


Figure 8.4 Density of states projected onto the Bi 6s (shaded in gray) and Bi 6p (red solid line) states of *ts*-BiVO₄, from (a) PBE, (b) HF25%, and (c) HF50% calculations. In the insets, the blue and green solid lines indicated the O 2p and V 3d states, respectively. The energy zero is set at the top of the valence band and dotted line indicates the Fermi energy (E_F). The right panel [in (c)] show the band-decomposed charge density (with isosurface value of $0.06 e/\text{\AA}^3$) within $-1.40 \text{ eV} < E - E_F < 0 \text{ eV}$. Purple, silver, and red balls represent Bi, V, and O atoms, respectively. All Bi-O bonds are omitted for clarity.

Figure 8.4 shows the electron density of states (DOS) projected onto the atomic orbitals of Bi, V, and O ions for the optimized *ts*-BiVO₄ structures with PBE [(a)], HF 25% [(b)], and HF 50% [(c)]. This analysis clearly shows that the interaction between the filled Bi 6*s* and O 2*p* states gives rise to bonding and antibonding states; the bonding states (8-11 eV below the Fermi level) are dominated by Bi 6*s* states with minor contributions from O 2*p* states, while the antibonding states (near the top of the valence band) are composed mainly of O 2*p* states with minor Bi 6*s* states. Our result is consistent with previous DFT calculations.^[159,176]

As the HF exchange weight is increased, the Bi 6*s* contribution to the top of the valence band becomes more pronounced, indicating a stronger antibonding interaction between Bi 6*s* and O 2*p* states. Note that, in the (high-symmetry) tetragonal phase, there is no noticeable secondary coupling of Bi 6*s* and 6*p* states near the valence band maximum, due to the orbital symmetry constraint as also evidenced by the spherically symmetric (*s*-like) charge distribution of Bi ions (see Fig. 8.4). In addition, we can see that the increase of HF exchange portion leads to a broadening and downshift of the valence band while increasing the band gap, which is a well-known feature of HF/DFT methods^[187]; recall that pure HF tends to overestimate band widths and band gaps.

Figure 8.5 shows the ion-projected valence electron DOS for *ms*-BiVO₄; only HF25% [(a)] and HF50% [(b)] optimized structures were considered as no minimum-energy monoclinic structure was obtained within PBE. Overall, the DOS features are similar to those for *ts*-BiVO₄, except the appearance of Bi 6*p* states at the valence band top (while their intensity is more pronounced with the HF exchange weight).

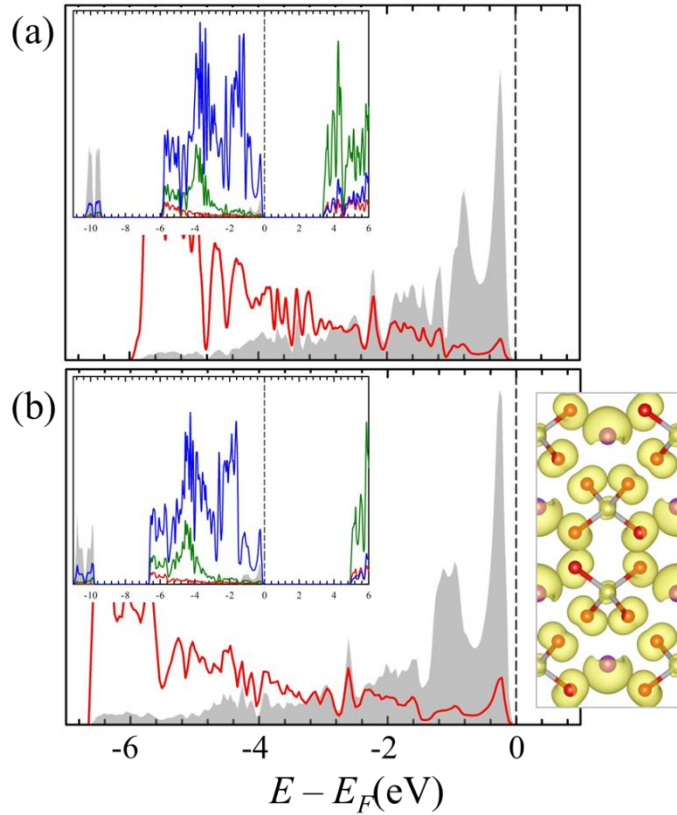


Figure 8.5 Density of states projected onto the Bi 6s (shaded in gray) and Bi 6p (red solid line) states of ms -BiVO₄, from (a) HF25% and (c) HF50% calculations. In the insets, the blue and green solid lines indicated the O 2p and V 3d states, respectively. The energy zero is set at the top of the valence band and dotted line indicates the Fermi energy (E_F). The right panel [in (b)] show the band-decomposed charge density (with isosurface value of $0.06 e/\text{\AA}^3$) within $-1.40 \text{ eV} < E - E_F < 0 \text{ eV}$. Purple, silver, and red balls represent Bi, V, and O atoms, respectively. All Bi-O bonds are omitted for clarity.

This supports the hybridization between Bi 6s–O 2p antibonding states and unoccupied Bi 6p states in the distorted ms -BiVO₄ structure (where the Bi site no longer has inversion symmetry due to its off-center displacement, as mentioned earlier). That is, the symmetry-lowering distortion (also referred to as second-order Jahn-Teller

distortion) stabilizes the occupied antibonding states near the Fermi level by allowing them to mix with the empty conduction-band states at the expense of increased strain energy.^[176] As shown in the inset of Fig. 8.5 (b), the analysis of decomposed Bi $6p_x$, $6p_y$, $6p_z$, and $6s$ orbitals demonstrates that only the p_z orbitals effectively overlap with the s orbitals; this can be explained by the fact that the s orbitals are asymmetrically distributed with lone-pair lobes aligned in the z direction. (Note that orbitals are allowed to interact with each other if they have similar symmetries, according to the Molecular Orbital theory).

Figure 8.6 shows band-structure diagrams calculated for ts -BiVO₄ [(a)] and ms -BiVO₄ [(b)] optimized within HF25%, along two high-symmetry directions (Σ and Δ) (or equivalent directions for ms -BiVO₄) in the Brillouin zone. We also calculated the band structures for PBE/HF50% optimized ts -BiVO₄ and HF50% optimized ms -BiVO₄. The shapes of the bands turn out to be negligibly affected by the xc functional choice, while the band gaps increase considerably with the increase of HF exchange fraction (see Table 8.4). For ts -BiVO₄, according to the above diagram, the valence band has maxima in the Δ directions (which are only about 0.1 eV higher than those in the Σ directions). The conduction band minima (CBM) are located midway along the Σ lines. Similar band characteristics have been also reported for tetragonal scheelite-type PbWO₄ and PbMoO₄.^[179] The results suggest that the minimum direct gap may lie in the Σ direction, and is slightly higher in energy than the lowest indirect gap. As listed in Table 8.4, the PBE values of 2.16/2.11 eV (indirect/direct) are found to be underestimate, but only marginally, the experimental value of 2.34 eV; the degree of gap underestimation is much smaller than that for many other oxides. The predicted gap values increase to 3.25/3.35 eV and 4.52/4.68 eV, respectively, as 25% and 50% of HF exchange are added to the PBE functional.

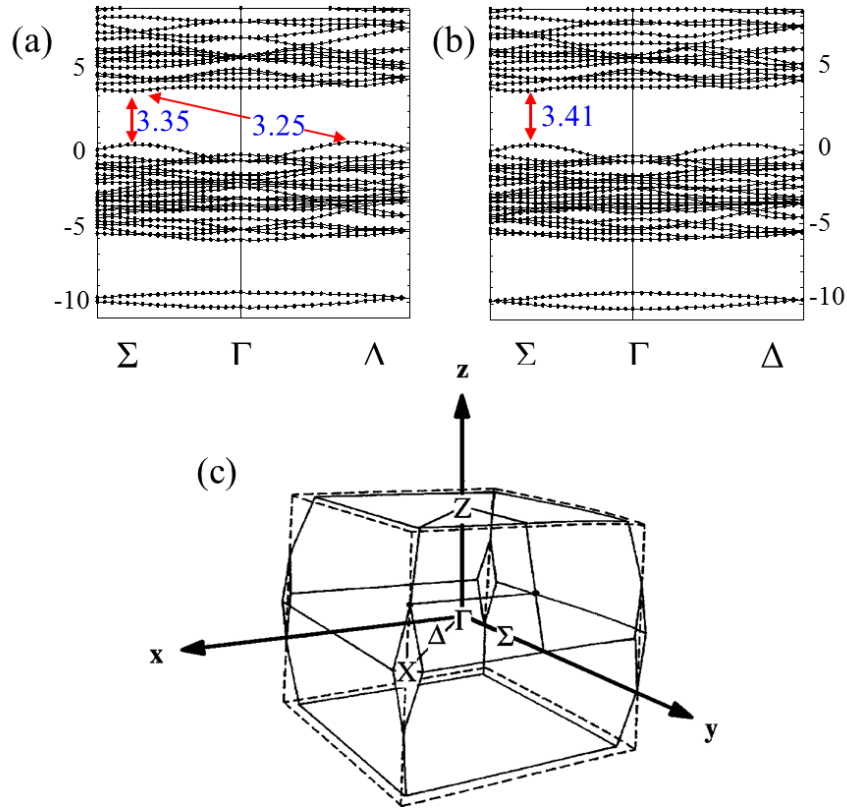


Figure 8.6 Electronic band structure for (a) *ts*-BiVO₄ and (b) *ms*-BiVO₄ from HF25% calculation and (c) Brillouin zone for a body-centered tetragonal crystal structure based on Ref [179]. The energy zero is set at the top of the valence band. The bands are plotted along the Σ (to the Γ point) and Δ direction (from the Γ point). The values of direct and indirect band gap are also indicated.

For *ms*-BiVO₄ [Fig. 8.6 (b)], the valence-band extrema in the Σ and Δ direction appear (nearly) degenerate, while the CBM lie along the Σ directions, implying that the minimum direct band gap lies in the Σ direction.

As summarized in Table 8.4, the predicted direct gap values of 3.41 eV (HF25%) and 4.99 eV (HF50%) for *ms*-BiVO₄ are consistently larger than corresponding 3.25/3.35 eV and 4.52/4.68 eV for *ts*-BiVO₄; this is consistent with previous experiments [i.e, 2.41-2.5 eV (*m*-BiVO₄) vs. 2.34 eV (*t*-BiVO₄)].

Table 8.4 Calculated band gaps of ts -BiVO₄ and ms -BiVO₄ from HF 25% and HF 50%.

	HF 25%			HF 50%		
	E_{gap}	k_v	k_c	E_{gap}	k_v	k_c
ts -BiVO ₄	3.25	Δ	Σ	4.52	Δ	Σ
	3.35	Σ	Σ	4.68	Σ	Σ
ms -BiVO ₄	3.41	Σ	Σ	4.99	Σ	Σ

The band gap widening in ms -BiVO₄ can be mainly attributed to stabilization of the valence-band top (or lowering of the VBM energy) through the coupling of Bi 6s-O 2p antibonding states with Bi 6p states, as discussed earlier. The phase transition is likely to affect negligibly the CBM (dominated by V 3d states with minor contributions from O 2p and Bi 6p). It is also interesting to note that the gap difference between ts -BiVO₄ and ms -BiVO₄ increases with the HF contribution, which is apparently due to the fact that the increased HF weight enhances the mixing of Bi 6s and 6p states and thus lowers the VBM in energy.

Chapter 9: Formation and Transport of Excess Charge Carriers in BiVO₄: A Hybrid Density Functional Theory Study

9.1 INTRODUCTION

Bismuth vanadate (BiVO₄) has received much recent interest as a promising visible-light-active photocatalyst for O₂ evolution in aqueous solutions.^[164-168] BiVO₄ is known to exist in three main crystal structures: tetragonal zircon (*tz*-), tetragonal scheelite (*ts*-), and monoclinic scheelite (*ms*-).^[169] Among them, *ms*-BiVO₄ exhibits the highest photocatalytic activity under visible light irradiation.^[170,171] The lower activity of *tz*-BiVO₄ has been explained by its large band gap (2.9 eV). While *ts*-BiVO₄ and *ms*-BiVO₄ have similar band gaps (2.3eV and 2.4eV, respectively), their main difference is a structural distortion associated with the stereochemically active Bi 6s² lone pair on *ms*-BiVO₄. It has been suggested that the monoclinic distortion might enhance the mobility of photogenerated holes, resulting in the better performance of *ms*-BiVO₄ over *ts*-BiVO₄.^[170,171] However, the photocatalytic activity of *ms*-BiVO₄ is hampered by its low electron mobility.^[188,189] Although experimental attempts to increase the electrical conductivity have achieved some success in improving photocatalytic activities^[167,189], the mechanism underlying the improvements are not well understood. Systematic experimental investigations coupled with solid theoretical studies of the nature and transport of photogenerated charge carriers in BiVO₄ are now needed to further improve the photocatalytic efficiency.

In semiconductor oxides, excess charge carriers strongly interact with the lattice due to the coulomb interaction between charges and ions, and with the interaction charge carriers become self-trapped within lattice distortions that they induce; the quasi-particle (charge and its accompanying lattice distortion) is called a polaron.^[190,191] There are two distinct types of polarons — small and large — depending on the spatial extent of the

lattice distortion; the former localize at the atomic scale and the latter are extended over several lattice sites. Accordingly, the transport mechanisms for small and large polarons are different; small polarons migrate from site to site via a thermally activated hopping process, while large polarons rather follow a band conduction mechanism. The small polaronic hopping of excess electrons or holes has been experimentally observed in several metal oxides including TiO_2 , Fe_2O_3 , WO_3 , and Cu_2O . However, the conduction mechanism of excess charge carriers in $ms\text{-BiVO}_4$ and $ts\text{-BiVO}_4$ is still unclear due to a lack of related experimental and theoretical investigations.

In this chapter, we have investigated the behavior of excess electrons and holes in both $ms\text{-}$ and $ts\text{-BiVO}_4$ phases based on the polaron model as well as the delocalized charge model using hybrid density function theory (DFT) calculations. It has been well known that conventional DFT within the local density approximation (LDA) or generalized gradient approximation (GGA) tends to erroneously favor delocalization of charge carriers due to the self-interaction of the electrons. Hybrid DFT, on the other hand, can more successfully describe the localized nature of excess charge carriers and give better agreement with experimental observation.

9.2 CALCULATION METHODS

The calculations reported herein were performed on the basis of density functional theory (DFT) as implanted in the Vienna *ab-initio* Simulation Package (VASP 5.2).^[32] The projector augmented wave (PAW) method with a planewave basis set was used to describe the interaction between ion cores and valence electrons.^[48] The valence-electron configurations considered are: $5d^{10}6s^26p^3$ for Bi; $3p^63d^34s^2$ for V; and $2s^22p^4$ for O. The lattice parameters for tetragonal and monoclinic BiVO_4 were obtained from

previous calculation. For systems with additional hole (or electron), we used a $2 \times 2 \times 2$ supercell (comprised of 16 BiVO_4 units) and subtracted one electron from (or added one electron to) the intrinsic system; a plane-wave cutoff energy 350eV and a gamma-point were used to calculate geometries, while an increased cutoff energy of 400eV and a gamma-centered $(2 \times 2 \times 2)k$ -point mesh were used to reevaluate total energies for optimized systems and corresponding electronic structures. In the geometry optimization, all atoms were fully relaxed using a conjugate gradient method until residual forces on constituent atoms become smaller than 0.01 eV/ \AA . All GGA calculations were performed within the Perdew-Burke-Ernzerhof (PBE) generalized gradient approximation (GGA).^[121] In the hybrid functional calculations, a fraction of Hartree-Fock (HF) exchange is added to PBE functional; here, two values for the fraction (α) of HF exchange from 0.25 and 0.50 are used. When $\alpha = 0.25$, our hybrid calculation is the same as the screened hybrid functional of Heyd, Scuseria, and Ernzerhof (HSE).^[182] In the HSE functional, the exchange term is split into a short-range and long-range part; to reduce the computational cost, a fraction of HF exchange is only mixed in short-range exchange term, while long-range exchange term is replaced by PBE exchange with no HF exchange. For other value of α , we used the same formula from the HSE functional, but changed the fraction of HF exchange based on chosen α .

9.3 NATURE OF EXCESS HOLE

9.3.1 Structure and stability

For *ts*- BiVO_4 , Fig. 9.1 shows the ion-projected electron density of states (DOS) for delocalized [in (a)] and polaronic [in (b)] hole structures. First, in the delocalized hole model, the Fermi level shifts down into the valence band upon introducing one

excess hole, resulting in the (spin-polarized) hole state at the top of the valence band [see in (a)]. The hole charge is spread over the entire lattice of Bi and O atoms, which can be explained by considering that the top of the valence band is mainly composed of the Bi 6s and O 2p orbitals.

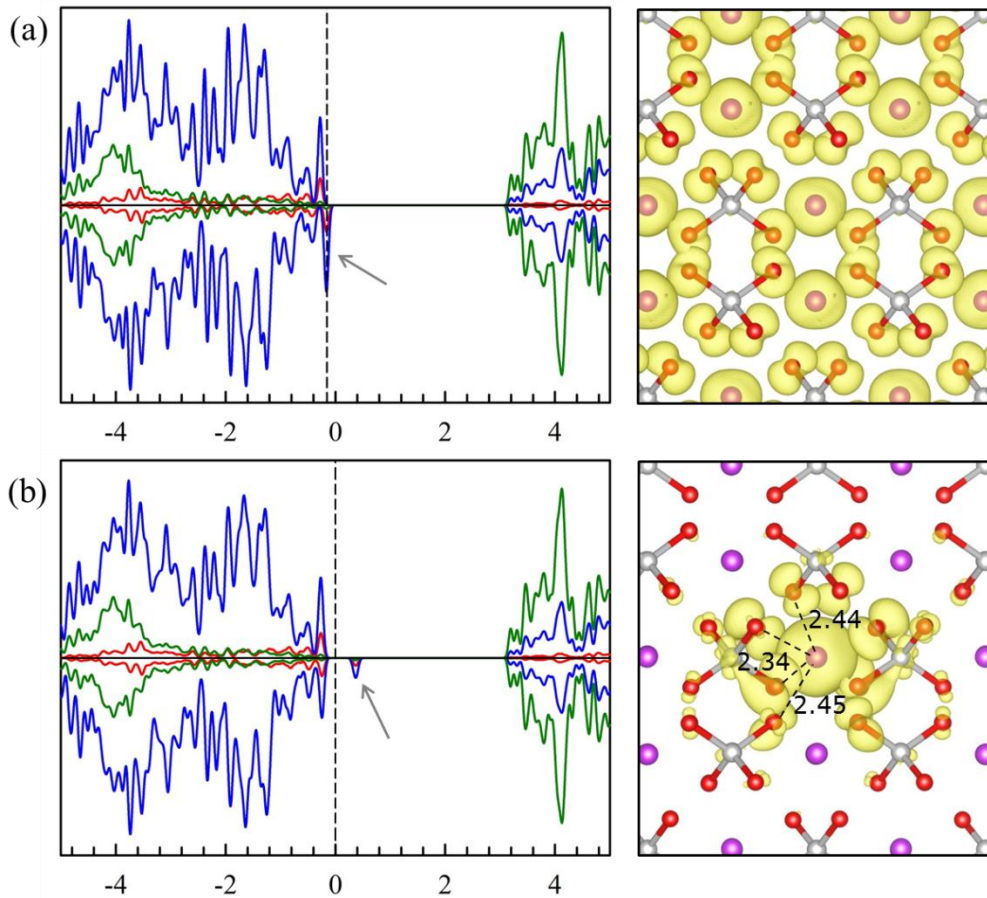


Figure 9.1 Total density of states (DOS) (left panels) and isosurfaces ($0.007 \text{ electron}/\text{\AA}^3$) of band-decomposed excess electron densities (right panels) of (a) delocalized and (b) small polaronic hole state in $ts\text{-BiVO}_4$. In the DOS plots, the red, blue, and green solid lines indicate the s , p , and d states, respectively. The energy zero is set at the top of the valence band and the dotted line indicates the Fermi energy. In the right panels, purple, silver, and red balls represent Bi, V, and O atoms, respectively. All Bi-O bonds are omitted for clarity.

As shown in Fig. 9.1(b), the polaronic hole forms the (spin-polarized) localized state, lying at approximately 0.6eV above the top of the valence band. The excess hole charge occurs predominately on a single Bi atom surrounded by O atoms (in a BiO_8 dodecahedron), implying the formation of a small polaron. Such hole trapping is accompanied by a large lattice distortion around the Bi site as depicted in the inset of Fig. 9.1(b); the Bi-O bonds (2.34/2.45) become shorter than other regular Bi-O bonds (2.43/2.48). That is, by trapping one excess hole, some fraction of the antibonding Bi-O state (consisting of the top of the valence band) is pushed up above the Fermi level, which consequently increases Bi-O bond strength. The spatial charge distribution [see the inset in (b)] also reveals Bi-O antibonding nature, with nodal planes between Bi and O atoms. Similar hole trapping characteristics also have been studied in hole-doped BaBiO_3 using hybrid functionals.^[192]

Overall, the small polaronic hole model is found to be about 0.13eV more stable than the delocalized one in $ts\text{-BiVO}_4$. However, we found that the energy difference between these two models varies depending on the exchange correlation (XC) functional used. At the PBE level, only the delocalized hole model is energetically stable; the polaronic hole model relaxes to the delocalized one by restoring the intrinsic lattice. On the other hand, calculation with 50% HF exchange predicts that the polaronic model becomes more stable (0.5eV in energy) with respect to the delocalized one. The PBE and hybrid results are different because the microscopic description of charge localization strongly depends on the method employed. Previous studies on TiO_2 also show that the nature of excess charge states is strongly affected by the degree of HF exchange in the hybrid functional; the localized state becomes more stable over the delocalized state by increasing the amount of HF exchange.^[193]

Next, we look at the hole state in ms - BiVO_4 . Similar to ts - BiVO_4 [Fig. 9.1(a)], the delocalized hole state exists at the top of the valence band as shown in Fig. 9.2(a).

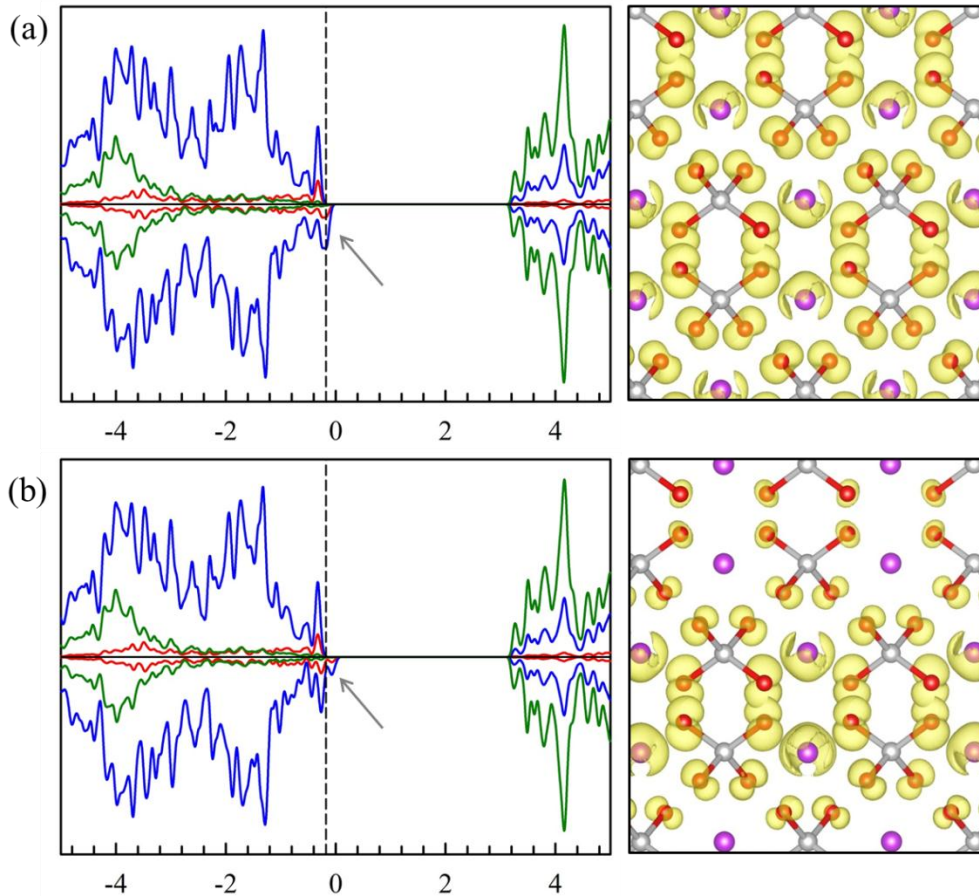


Figure 9.2 Total density of states (DOS) (left panels) and isosurfaces ($0.004 \text{ electron}/\text{\AA}^3$) of band-decomposed excess electron densities (right panels) of (a) delocalized and (b) large polaronic hole state in ms - BiVO_4 . In the DOS plots, the red, blue, and green solid lines indicate the s , p , and d states, respectively. The energy zero is set at the top of the valence band and the dotted line indicates the Fermi energy. In the right panels, purple, silver, and red balls represent Bi, V, and O atoms, respectively. All Bi-O bonds are omitted for clarity.

However, due to additional mixing between the antibonding Bi 6s-O 2p and Bi 6p states in *ms*-BiVO₄, the spatial charge distribution is slightly different from *ts*-BiVO₄. The hole charge appears more in the region where Bi 6s² lone pairs are projecting [see the inset of Fig. 9.2(a)], which leads to alternating layers of hole charge perpendicular to the z-direction (i.e. highly populated/less populated).

For the polaronic hole, the unoccupied state is lying just above the top of the valence band as shown in Fig. 9.2(b), which seems similar to that for the delocalized one in Fig. 9.2(a). However, the polaronic state is accompanied by (slight) structural distortion over a wide spatial range [see the inset of Fig. 9.2(b)]; the shortest Bi-O bond length is decreased to 2.35Å, compared with 2.37Å in the delocalized hole structure, while there are relatively negligible changes in other Bi-O bond lengths. This feature clearly implies the formation of a large polaron, which is also evidenced by the charge distribution in Fig. 9.2(b); the hole charge is extended over a layer, particularly in which Bi 6s² lone pairs exist.

Although the large polaron is different from the delocalized one, the large polaron structure is almost degenerate in energy with the delocalized hole structure (the former is about 10 meV more favorable than the latter), implying both structures are likely to occur. To examine energy dependence on XC functional, we further performed the same calculation with PBE and 50% HF exchange. The PBE calculation only predicts the delocalized hole model, as expected. However, with higher degree of HF exchange (50%), the small polaronic structure with local lattice distortion is preferred by nearly 0.35 eV over the delocalized hole model. Here, the excess hole forms a small polaron rather than a large polaron, which is opposite to that with 25% HF exchange, due to higher tendency of charge localization in 50% HF than 25% HF.

Although the relative stability between the delocalized and polaronic hole structures is strongly affected by degree of HF exchange, the energy difference between them within the same calculation level suggests that the formation of small polarons in *ts*-BiVO₄ is more likely than in *ms*-BiVO₄; within 50% HF calculation, the small polaronic state is 0.5eV and 0.35 eV more stable than the delocalized one for *ts*-BiVO₄ and *ms*-BiVO₄, respectively.

9.3.2 Transport

Taking into account the different structural nature of excess holes in *ts*-BiVO₄ and *ms*-BiVO₄ within 25% HF calculation, we examined conduction mechanisms for each. First, a small hole polaron in *ts*-BiVO₄ will migrate by thermally activated hopping.

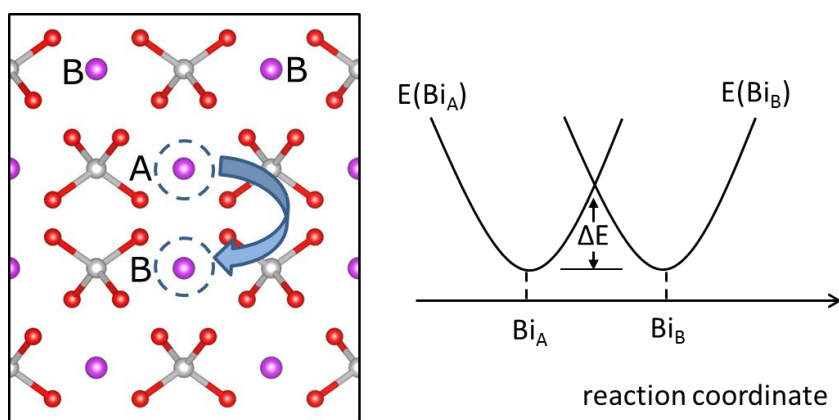


Figure 9.3 Predicted migration pathway for small polaronic hole in *ts*-BiVO₄ (left panel) and potential energy surfaces of the initial [E(Bi_A)] and final state [E(Bi_B)] (right panel). Purple, silver, and red balls represent Bi, V, and O atoms, respectively. All Bi-O bonds are omitted for clarity.

Fig. 9.3 shows the polaron hopping pathway from one Bi (Bi_A) site to an adjacent Bi (Bi_B) site. Note that since the initial (Bi_A) and final (Bi_B) states are translationally equivalent, the transition state is midway between them, and it can be calculated by $q_{\text{TS}} = (q_A + q_B)/2$, where q_A , q_B , and q_{TS} are the position vectors of atoms in the initial (A), final (B), and transition states, under a linear interpolation scheme.^[194] The hopping barrier (ΔE) is calculated to be about 60meV. On the other hand, in *ms*- BiVO_4 , since the delocalized and large polaron structures are very close in energy, both are in principle possible. Transport of both can be described by band-type conduction; e.g. for large the polaron, conduction occurs through band-type motion of polarons.^[195] It is known that the mobility of a small polaron is less than $1\text{cm}^2/\text{Vs}$, which is lower than that of a quasi-free charge carrier (following band conduction).^[196] As a result, it can be expected that hole mobility in *ts*- BiVO_4 might be lower than in *ms*- BiVO_4 .

9.4 NATURE OF EXCESS ELECTRON

9.4.1 Structure and stability

For *ts*- BiVO_4 , we examined delocalized and polaronic states for excess electrons. As shown in Fig.9.4 (a), the (spin-polarized) delocalized state exists at the bottom of the conduction band, which is composed mainly of V 3d with minor contribution from O 2p and Bi 6p. As depicted in (a), the charge is delocalized over all of the V atoms of the cell, especially on the d_{z^2} state of the V atoms. This can be explained by considering that the 3d states, in tetrahedral (T_d) crystal field, split into low lying e states ($3d_{z^2}$ and $3d_{x^2-y^2}$) and higher lying t_2 states ($3d_{xz}$, $3d_{yz}$, and $3d_{xy}$). However, the T_d symmetry of a free $[\text{VO}_4]^{2-}$ ion is reduced to S_4 in the scheelite structure, since the $[\text{VO}_4]^{2-}$ ion in *ts*- BiVO_4 is slightly compressed along the z -direction. This symmetry lowering induces

further splitting of the doubly degenerate e states and makes the d_{z^2} state the lowest in energy.

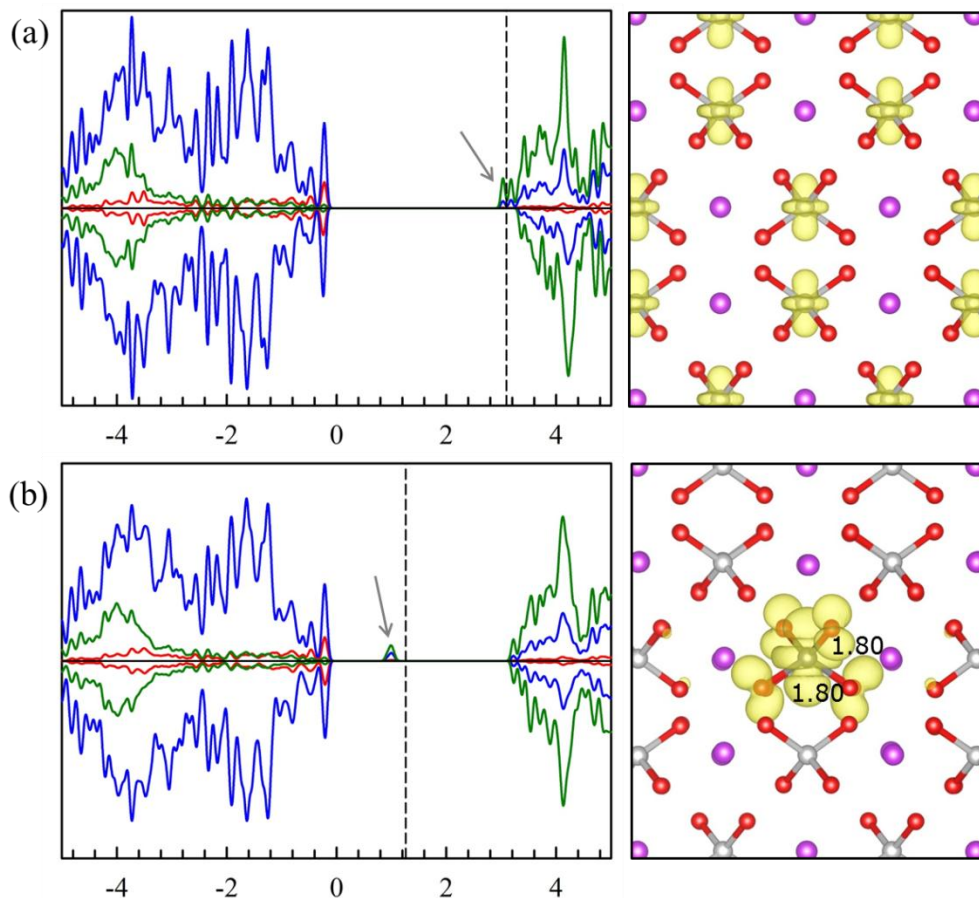


Figure 9.4 Total density of states (DOS) (left panels) and isosurfaces (0.008 electron/Å³) of band-decomposed excess electron densities (right panels) of (a) delocalized and (b) small polaronic electron state in ts -BiVO₄. In the DOS plots, the red, blue, and green solid lines indicate the s , p , and d states, respectively. The energy zero is set at the top of the valence band and the dotted line indicates the Fermi energy. In the right panels, purple, silver, and red balls represent Bi, V, and O atoms, respectively. All Bi-O bonds are omitted for clarity.

On the other hand, the polaronic electron state is localized within the band gap about 2 eV below the conduction band as shown in Fig. 9.4(b). Also, in the inset of (b), the strongly localized charge on the $3d_{z^2}$ of the single V with considerable contribution from O 2p suggests formation of small polaron. That is, with one excess electron, V^{5+} is reduced to V^{4+} , which polarizes the surrounding lattices (mostly O atoms in VO_4), and the resulting atomic distortion causes the excess electron to be self-trapped at that V site. As presented in the inset of Fig. 9.4(b), the V-O bond length (1.80Å) is increased compared with regular V-O bond (1.72Å); the increased V-O bond lengths are due to partial filling of antibonding orbitals formed from the interaction of V 3d and O 2p orbitals, which were initially empty on the conduction band. Similar small polaronic behavior has been observed in TiO_2 ; a small polaronic electron accompanies the lattice distortion surrounding Ti^{3+} with increased Ti-O bond lengths.^[194]

Our hybrid calculation (with 25% HF) predicts that the small polaron model is much stable (by 0.84eV) than the delocalized electron model. However, as mentioned earlier, the relative stability between these two models highly depends on the XC functional. With the PBE functional, the small polaronic model turns out to be unstable and only the delocalized model is found. Oppositely, with higher fraction (50%) of HF exchange, the small polaron structure becomes more favorable than the delocalized model.

Next, Fig. 9.5 shows the ion-projected DOS for two different electron models in *ms*- $BiVO_4$. In the delocalized electron model [in (a)], the excess electron occupies the bottom of the conduction band (only spin-up state). The charge is delocalized on the d_{z^2} state of the all V atoms, similar to that in *t*- $BiVO_4$ [in Fig. 9.4(a)]. For the polaron model [in Fig. 9.5(b)], we also confirmed the formation of small electron polarons by examining the local lattice distortion around V^{4+} site. The two different V-O bond

lengths are also increased from 1.69Å/1.75Å to 1.77Å/1.84Å by trapping one excess electron as indicated in the inset of Fig. 9.4(b).

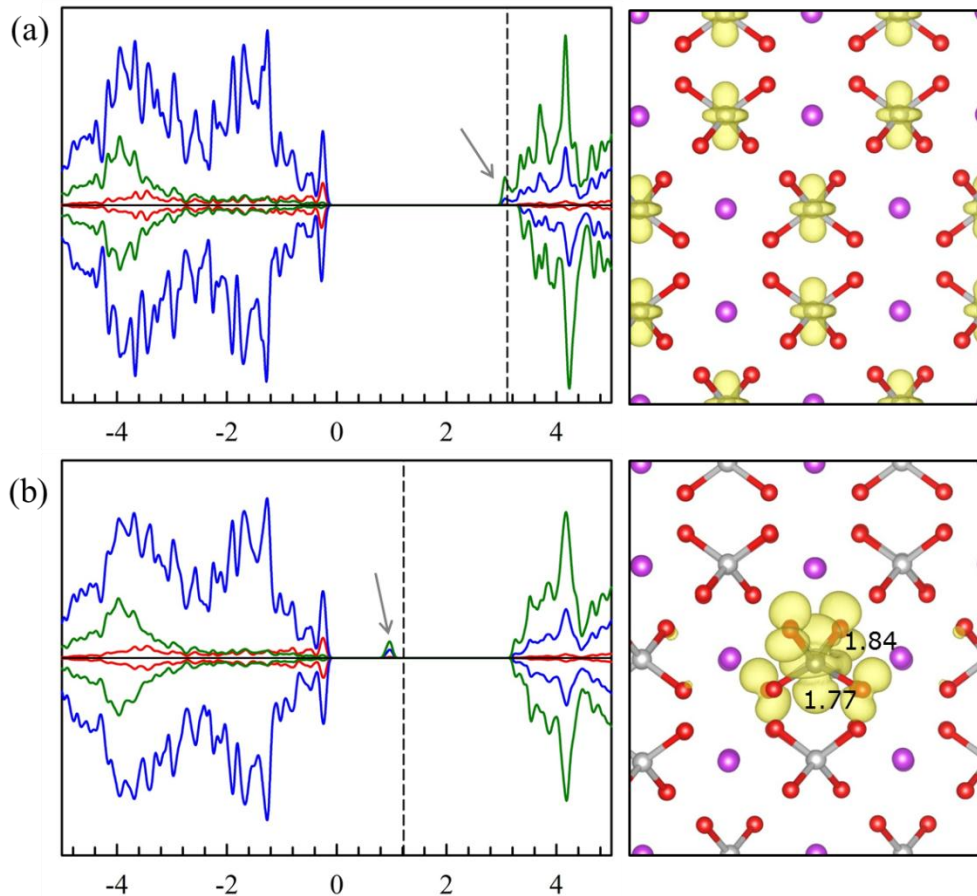


Figure 9.5 Total density of states (DOS) (left panels) and isosurfaces ($0.008 \text{ electron}/\text{\AA}^3$) of band-decomposed excess electron densities (right panels) of (a) delocalized and (b) small polaronic electron state in $ms\text{-BiVO}_4$. In the DOS plots, the red, blue, and green solid lines indicate the s , p , and d states, respectively. The energy zero is set at the top of the valence band and the dotted line indicates the Fermi energy. In the right panels, purple, silver, and red balls represent Bi, V, and O atoms, respectively. All Bi-O bonds are omitted for clarity

This small polaronic electron state is energetically much more favorable (by 0.85 eV) than the delocalized one. In addition, the functional dependence on the relative stability between the delocalized and small polaron model also shows similar trends to that in *ts*-BiVO₄.

To our knowledge, there is no experimental evidence for the existence of small polarons in either *ts*-BiVO₄ or *ms*-BiVO₄. However, it has been observed that excess electrons in PbWO₄ and PbMoO₄ (tetragonal scheelite structure) form small polarons [197]; e.g. for PbWO₄, W⁶⁺ (5d⁰) is reduced to W⁵⁺ (5d¹) by trapping one excess electron, which has been detected by EPR experiments. Considering W 5d states are more extended than V 3d states, it can be expected that excess electrons might form small polarons in BiVO₄. This might also imply that the hybrid functional would predict the nature of the excess electron state more accurately than the semilocal PBE functional, since the PBE calculation fails to give a small polaronic electron state in both *ts*-BiVO₄ and *ms*-BiVO₄.

9.4.2 Transport

In both *ts*-BiVO₄ and *ms*-BiVO₄, electron transport is governed by small polaron hopping (within 25% HF calculation). Fig. 9.6 shows the electron hopping pathway from one V site to its next-nearest neighbor, where the transition state is taken to be the midpoint between the initial and final structures (based on linear interpolation).

For *ms*-BiVO₄, two possible directions ($V_A \rightarrow V_B$ and $V_A \rightarrow V_C$) are examined, while only one direction ($V_A \rightarrow V_B$) is used for *ts*-BiVO₄. It turns out that the energy barriers for *ts*-BiVO₄ and *ms*-BiVO₄ are 0.46 eV and 0.46/0.46 eV, respectively. Although there are no experimental data to verify our calculated values, some experiments to obtain the polaron hopping barrier were performed in PbMoO₄, which

also possesses tetragonal scheelite structure^[197]; the measured activation energy for small polaron hopping is 0.38eV and the carrier mobility extracted from their I-V measurement is $10^{-5}\text{cm}^2/\text{Vs}$. Although this value is somewhat lower than in BiVO_4 , this can perhaps be attributed to the relative width of the V 3d band, which is narrower than the Mo 4d band.

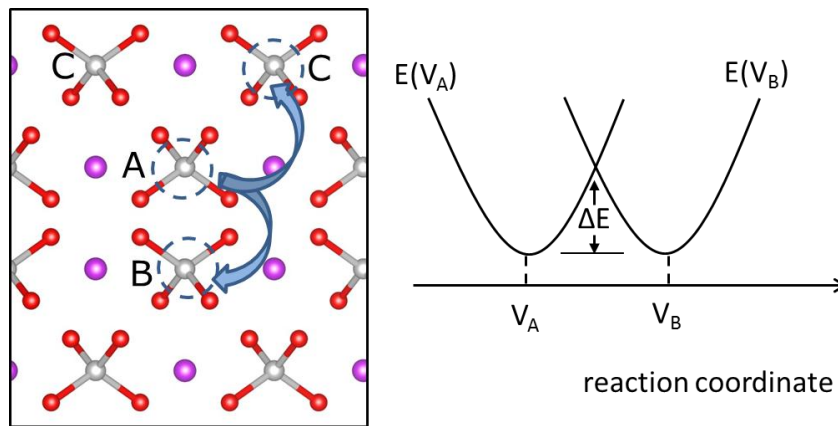


Figure 9.6 Predicted migration pathway for small polaronic electron in $t\text{-BiVO}_4$ and $ms\text{-BiVO}_4$ (left panel) and potential energy surfaces of the initial [$E(V_A)$] and final state [$E(V_B)$] (right panel). Purple, silver, and red balls represent Bi, V, and O atoms, respectively. All Bi-O bonds are omitted for clarity.

9.5 SUMMARY

Based on the hybrid calculation with 25% HF, we found

- the mobility of holes in $ts\text{-BiVO}_4$ might be lower than in $ms\text{-BiVO}_4$, since small polaron hopping typically occurs more slowly than band-type conduction.

- the mobility of electrons in both *ts*- and *ms*-BiVO₄ might be much lower than the mobility of holes in *ts*- and *ms*-BiVO₄, since the hopping barrier (~0.45eV) for electrons is much larger than (~0.06eV) for holes (in *ts*-BiVO₄).

These imply that electron transport might be a limiting factor between electron and hole transport, which agrees well with recently reported experiments.^[188,198] Also, with similar calculated electron mobility in both *ts*-BiVO₄ and *ms*-BiVO₄, the higher photocatalytic performance (especially O₂ evolution) in *ms*-BiVO₄ might be due to higher hole mobility in *ms*-BiVO₄ than in *ts*-BiVO₄.

References

- [1] Editorial, “Perfectly imperfect” *Nature Nanotechnology* **5**, 311 (2010).
- [2] A. Curraon, “Photoelectrochemical water splitting” *Chimia*, **61**, 815 (2007).
- [3] S. Harrison, T. Edgar, and G. S. Hwang, “Interstitial-mediated mechanisms of As and P diffusion in Si: Gradient-corrected density-functional calculations” *Phys. Rev. B* **74**, 195202 (2006).
- [4] Y. Liang, T. Tsubota, L. P. A. Mooij, and R. van de Krol, “Highly improved quantum efficiencies for thin film BiVO₄ photoanodes” *J. Phys. Chem. C* **115**, 17594 (2011).
- [5] J. Su, L. Guo, N. Bao, and C. A. Grimes, “Nanostructured WO₃/BiVO₄ heterojunction films for efficient photoelectrochemical water splitting” *Nano Lett.* **11**, 1928 (2011).
- [6] M. Born and R. Oppenheimer, “Zur quantentheorie der molekeln” *Annalen der Physik* **389**, 457 (1927).
- [7] M. Springborg, *Methods of Electronic Structure Calculations: From molecules to solids* (Wiley, New York, New York, 2000).
- [8] P. Hohenberg and W. Kohn, “Inhomogeneous electron gas” *Phys. Rev.* **136**, B864 (1964).
- [9] R. M. Martin, *Electronic Structure: Basic Theory and Practical Methods* (Cambridge University Press, 2004).
- [10] W. Kohn and L. J. Sham, “Self-consistent equations including exchange and correlation effects” *Phys. Rev.* **140**, A1133 (1965).
- [11] R. M. Dreizler and E. K. U. Gross, *Density Functional Theory* (Springer, 1990).
- [12] R. G. Parr and W. Yang, *Density-Functional Theory of Atoms and Molecules* (Oxford University Press, 1989).
- [13] D. M. Ceperley and B. J. Alder, “Ground state of the electron gas by a stochastic method” *Phys. Rev. Lett.* **45**, 566 (1980).
- [14] K. Capelle, “A bird’s-eye view of density-functional theory”, *Braz. J. Phys.* **36**, 1318 (2006).

- [15] J. P. Perdew and Y. Wang, “Accurate and simple density functional for the electronic exchange energy: Generalized gradient approximation” *Phys. Rev. B*, **33**, 8800 (1986).
- [16] J. P. Perdew, “Unified theory of exchange and correlation beyond the local density approximation” *Electronic Structure of Solids '91* (edited by P. Ziesche and H. Eschrig, 11 1991).
- [17] K. Burke, J. P. Perdew, and Y. Wang, “Derivation of a generalized gradient approximation: The PW91 density functional” *Electronic Density Functional Theory: Recent Progress and New Directions* (edited by J. F. Dobson, G. Vignale and M. P. Das, 81-121, 1997).
- [18] J. P. Perdew, K. Burke, and M. Ernzerhof, “Generalized gradient approximation made simple” *Phys. Rev. Lett.* **77**, 3865 (1996).
- [19] J. P. Perdew, K. Burke, and M. Ernzerhof, “Generalized gradient approximation made simple – Errata” *Phys. Rev. Lett.*, **78**, 1396 (1997).
- [20] B. Hammer, L. B. Hansen, and J. K. Nørskov, “Improved adsorption energetics within density-functional theory using revised Perdew-Burke-Ernzerhof functionals” *Phys. Rev. B* **59**, 7413 (1999).
- [21] A. Krasheninnikov, *Introduction to electronic structure simulations – Lecture 8* (University of Helsinki and Helsinki University of Technology, 2006)
- [22] D. R. Hamann, M. Schlüter, and C. Chiang, “Norm-conserving pseudopotentials” *Phys. Rev. Lett.* **43**, 1494 (1979).
- [23] D. Vanderbilt, “Soft self-consistent pseudopotentials in a generalized eigenvalue formalism” *Phys. Rev. B* **41**, 7892 (1990).
- [24] P. Blöchl, “Generalized separable potentials for electronic-structure calculations” *Phys. Rev. B* **41**, 5414 (1990).
- [25] N. Troullier and J. L. Martins, “Efficient pseudopotentials for plane-wave calculations” *Phys. Rev. B* **43**, 1993 (1991).
- [26] K. C. Pandey, A. Erbil, G. S. Cargill III, R. F. Boehme, and D. Vanderbilt, “Annealing of heavily arsenic-doped silicon – Electrical deactivation and a new defect complex” *Phys. Rev. Lett.* **61**, 1282 (1988).
- [27] P. M. Rousseau, P. B. Griffin, and J. D. Plummer, “Electrical deactivation of arsenic as a source of point defects” *Appl. Phys. Lett.* **65**, 578 (1994).

- [28] P. M. Fahey, P. B. Griffin, and J. D. Plummer, "Point-defects and dopant diffusion in silicon" *Rev. Mod. Phys.* **61**, 289 (1989).
- [29] A. Ural, P. B. Griffin, and J. D. Plummer, "Fractional contributions of microscopic diffusion mechanisms for common dopants and self-diffusion in silicon" *J. Appl. Phys.* **85**, 6440 (1999).
- [30] S. Solmi, M. Ferri, M. Bersani, D. Giubertoni, and V. Soncini, "Transient enhanced diffusion of arsenic in silicon" *J. Appl. Phys.*, **94**, 4950 (2003).
- [31] J. P. Perdew and Y. Wang, "Accurate and simple analytic representation of the electron-gas correlation energy: *Phys. Rev. B* **45**, 13244 (1992).
- [32] G. Kresse and J. Furthmuller, *VASP: The Guide* (Vienna University of Technology, Vienna, Austria, 2001).
- [33] H. J. Monkhorst and J. D. Pack, "Special points for brillouin-zone integrations" *Phys. Rev. B* **13**, 5188 (1976).
- [34] G. Henkelman, B. P. Uberuaga, and H. Jónsson, "A climbing image nudged elastic band method for finding saddle points and minimum energy paths", *J. Chem. Phys.* **113**, 9901 (2000).
- [35] S. A. Harrison, T. F. Edgar, and G. S. Hwang, "Interstitial-mediated mechanisms of As and P diffusion in Si : Gradient-corrected density-functional calculations" *Phys. Rev. B* **74**, 195202 (2006).
- [36] S. A. Harrison, T. F. Edgar, and G. S. Hwang, "Structure and dynamics of the diarsenic complex in crystalline silicon" *Phys. Rev. B* **72**, 195414 (2005).
- [37] W. Lee, S. Lee, and K. J. Chang, "First principles study of the self-interstitial diffusion mechanism in silicon" *J. Phys.: Condens. Matter* **10**, 995 (1998).
- [38] G. M. Lopez and V. Fiorentini, "Structure, energetics, and extrinsic levels of small self-interstitial clusters in silicon" *Phys. Rev. B* **69**, 155206 (2004).
- [39] Y. A. Du, R. G. Hennig, and J. W. Wilkins, "Diffusion mechanisms for silicon di-Interstitials" *Phys. Rev. B* **73**, 245203 (2006).
- [40] J. R. Pfister, L. C. Parrillo, and F. K. Baker, "A physical model for boron penetration through thin gate oxides from p+ polysilicon gates", *IEEE Electron Device Lett.* **11**, 247 (1990).

- [41] Z. J. Ma, J. C. Chen, Z. H. Liu, J. T. Krick, Y. T. Cheng, C. Hu, and P. K. Ko, "Suppression of boron penetration in p⁺ poly-silicon gate p-MOSFET's using low-temperature gate oxide N₂O anneal", IEEE Electron Device Lett. **15**, 109 (1994).
- [42] N. Kimizuka, K. Yamaguchi, K. Imai, T. Iizuka, C. T. Liu, R. C. Keller, and T. Horiuchi, "NBTI enhancement by nitrogen incorporation into ultrathin gate oxide for 0.10 μm gate CMOS generation" Symp. VLSI Technology p. 92 (2000).
- [43] K. Kawase, H. Umeda, M. Inoue, S. Tsujikawa, Y. Akamatsu, T. Suwa, M. Higuchi, M. Komura, A. Teramoto, and T. Ohmi, "Control of nitrogen depth profile and chemical bonding state in silicon oxynitride films formed by radical nitridation", Jpn. J. Appl. Phys. **44**, 7395 (2005).
- [44] K. Kawase, T. Suwa, M. Higuchi, H. Umeda, M. Inoue, S. Tsujikawa, A. Teramoto, T. Hattori, S. Sugawa, and T. Ohmi, "Control of nitrogen depth profile near silicon oxynitride/Si (100) interface formed by radical nitridation", Jpn. J. Appl. Phys. **45**, 6203 (2006).
- [45] H. J. Song, H. J. Shin, Y. Chung, J. C. Lee, and M. K. Lee, "X-ray absorption and photoelectron spectroscopic study of plasma-nitrided SiO₂ film", J. Appl. Phys. **97**, 113711 (2005).
- [46] J. A. Taylor, G. M. Lancaster, A. Ignatiev, J. W. Rabalais, "Interaction of ion beams with surfaces. Reactions of nitrogen with silicon and its oxides", J. Chem. Phys. **68**, 1776 (1978).
- [47] H. D. Hagstrum and G. E. Becker, "Resonance, auger, and autoionization processes involving He⁺(2s) and He⁺⁺ near solid surfaces", Phys. Rev. B **8**, 107 (1973).
- [48] P. E. Blöchl, "Projector augmented-wave method", Phys. Rev. B **50**, 17953 (1994).
- [49] C. M. Carbonaro, V. Fiorentini, and F. Bernardini, "Proof of the thermodynamical stability of the E' center in SiO₂", Phys. Rev. Lett. **86**, 3064 (2001).
- [50] Z. Lu, C. J. Nicklaw, D. M. Fleetwood, R. D. Schrimpf, and S. T. Pantelides, "Structure, properties, and dynamics of oxygen vacancies in amorphous SiO₂", Phys. Rev. Lett. **89**, 285505 (2002).
- [51] P. V. Sushko, S. Mukhopadhyay, A. S. Mysovsky, V. B. Sulimov, A. Taga and A. L. Shluger, "Structure and properties of defects in amorphous silica: new insights from embedded cluster calculations", J. Phys.: Condens. Matter **17**, S2115 (2005).

- [52] B. R. Tuttle and S. T. Pantelides, “Vacancy-related defects and the E_{δ}' center in amorphous silicon dioxide: Density functional calculations”, *Phys. Rev. B* **79**, 115206 (2009).
- [53] D. L. Griscom and E. J. Friebele, “Fundamental radiation-induced defect centers in synthetic fused silicas: atomic chlorine, delocalized E' centers, and a triplet state”, *Phys. Rev. B* **34**, 7524 (1986).
- [54] G. Buscarino, S. Agnello, and F. M. Gelardi, “Delocalized nature of the E_{δ}' center in amorphous silicon dioxide”, *Phys. Rev. Lett.* **94**, 125501 (2005).
- [55] L. Skuja, “Optically active oxygen-deficiency-related centers in amorphous silicon dioxide”, *J. Non-Cryst. Solids*, **239**, 16 (1998).
- [56] A. J. Lelis, T. R. Oldham, H. E. Boesch, and F. B. McLean, “The nature of the trapped hole annealing process”, *IEEE Trans. Nucl. Sci.* **36**, 1808 (1989).
- [57] A. J. Lelis, H. E. Boesch, T. R. Oldham, and F. B. McLean, “Reversibility of trapped hole annealing”, *IEEE Trans. Nucl. Sci.* **35**, 1186 (1988).
- [58] T. Uchino and T. Yoko, “Density functional theory of structural transformations of oxygen-deficient centers in amorphous silica during hole trapping: structure and formation mechanism of the E_{γ}' center”, *Phys. Rev. B* **74**, 125203 (2006).
- [59] D. L. Griscom and M. Cook, “ ^{29}Si superhyperfine interactions of the E' center: a potential probe of range-II order in silica glass”, *J. Non-Cryst. Solids* **182**, 119 (1995).
- [60] T. Uchino, M. Takahashi, and T. Yoko, “Mechanism of interconversion among radiation-induced defects in amorphous silicon dioxide”, *Phys. Rev. Lett.* **86**, 1777 (2001)
- [61] S. Mukhopadhyay, P. V. Sushko, A. M. Stoneham, and A. L. Shluger, “Modeling of the structure and properties of oxygen vacancies in amorphous silica”, *Phys. Rev. B* **70**, 195203 (2004).
- [62] L. Skuja, “Isoelectronic series of twofold coordinated Si, Ge, and Sn atoms in glassy SiO_2 : a luminescence study”, *J. Non-Cryst. Solids* **149**, 77 (1992).
- [63] C. Kuo and G. S. Hwang, “Structure and interconversion of oxygen vacancy related defects on amorphous silica”, *Phys. Rev. Lett.* **97**, 066101 (2006).
- [64] T. Laino, D. Donadio, and I. W. Kuo, “Migration of positively charged defects in α -quartz”, *Phys. Rev. B* **76**, 195210 (2007).

- [65] D. Donadio, M. Bernasconi, M. Boero, “Ab Initio simulations of photoinduced interconversions of oxygen deficient centers in amorphous silica”, *Phys. Rev. Lett.* **87**, 195504 (2001).
- [66] Y. Chung, J. C. Lee, and H. J. Shin, “Direct observation of interstitial molecular N₂ in Si oxynitrides”, *Appl. Phys. Lett.* **86**, 022901 (2005).
- [67] C. R. Brundle, “XPS and UPS studies of the interaction of nitrogen-containing molecules with nickel: the use of binding energy patterns and relative intensities to diagnose surface species”, *J. Vac. Sci. Technol.* **13**, 301 (1976).
- [68] K. Kajihara, M. Hirano, Y. Takimoto, L. Skuja, and H. Hosono, “Diffusion of nitrogen molecules in amorphous SiO₂”, *Appl. Phys. Lett.* **91**, 071904 (2007).
- [69] T. Bakos, S. N. Rashkeev, and S. T. Pantelides, “H₂O and O₂ molecules in amorphous SiO₂: defect formation and annihilation mechanisms”, *Phys. Rev. B* **69**, 195206 (2004).
- [70] G. Pacchioni, L. Skuja, and D. L. Griscom, *Defects in SiO₂ and related dielectrics: Science and technology* (NATO Science Series, Italy, 2000).
- [71] I. Last, A. Aguilar, R. Sayos, M. Gonzalez, and M. Gilibert, “Potential energy surface of the O(¹D)+N₂O→2NO, O₂+N₂ Reactions”, *J. Phys. Chem. A* **101**, 1206 (1997)
- [72] A. F. Shestakov and A. E. Shilov, “On the coupled oxidation-reduction mechanism of molecular nitrogen fixation”, *Russian Chem. Bulletin*, **50**, 2054 (2001).
- [73] J. Dai, J. Yuan, and P. Giannozzi, “Gas adsorption on graphene doped with B, N, Al, and S: A theoretical study” *Appl. Phys. Lett.* **95**, 232105 (2009).
- [74] N. Kurita, “Molecular orbital calculations on lithium absorption in boron- or nitrogen-substituted carbon” *Carbon* **38**, 65 (2000).
- [75] M. Endo, C. Kim, T. Karaki, Y. Nishimura, M. J. Matthews, S. D. M. Brown, M. S. Dresselhaus, “Anode performance of a Li ion battery based on graphitized and B-doped milled mesophase pitch-based carbon fibers” *Carbon* **37**, 561 (1999).
- [76] R. H. Miwa, T. B. Martins, and A. Fazzio, “Hydrogen adsorption on boron doped graphene: An ab initio study” *Nanotechnology* **19**, 155708 (2008).
- [77] Y. Ferro, F. Marinelli, A. Jelea, and A. Allouche, “Adsorption, diffusion, and recombination of hydrogen on pure and boron-doped graphite surfaces” *J. Chem. Phys.* **120**, 11882 (2004).

- [78] Z. H. Zhu, G. Q. Lu, and H. Hatori, "New insights into the interaction of hydrogen atoms with boron-substituted carbon" *J. Phys. Chem. B* **110**, 1249 (2006).
- [79] Y. Zhang, Y. Chen, K. Zhou, C. Liu, J. Zeng, H. Zhang, and Y. Peng, "Improving gas sensing properties of graphene by introducing dopants and defects: A first principles study" *Nanotechnology* **20**, 185504 (2009).
- [80] M. Sankaran and B. Viswanathan, "Hydrogen storage in boron substituted carbon nanotubes" *Carbon* **45**, 1628 (2007).
- [81] R. Wang, D. Zhang, Y. Zhang, and C. Liu, "Boron-doped carbon nanotubes serving as a novel chemical sensor for formaldehyde" *J. Phys. Chem. B* **110**, 18267 (2006).
- [82] R. Singh and P. Kroll, "Magnetism in graphene due to single-atom defects: dependence on the concentration and packing geometry of defects" *J. Phys.: Condens. Matter* **21**, 196002 (2009).
- [83] L. S. Panchakarla, K. S. Subrahmanyam, S. K. Saha, A. Govindaraj, H. R. Krishnamurthy, U. V. Waghmare, and C. N. R. Rao, "Synthesis, structure, and properties of boron- and nitrogen-doped graphene" *Adv. Mater.* **21**, 4726 (2009).
- [84] M. Endo, T. Hayashi, S. Hong, T. Enoki, and M. S. Dresselhaus, "Scanning tunneling microscope study of boron-doped highly oriented pyrolytic graphite" *J. Appl. Phys.* **90**, 5670 (2001).
- [85] C. N. R. Rao, A. K. Sood, Rakesh Voggu, and K. S. Subrahmanyam, "Some novel attributes of graphene" *J. Phys. Chem. Lett.* **1**, 572 (2010).
- [86] O. V. Yazyev and L. Helm, "Defect-induced magnetism in graphene" *Phys. Rev. B* **75**, 125408 (2007).
- [87] P. O. Lehtinen, A. S. Foster, Y. Ma, A. V. Krasheninnikov, and R. M. Nieminen, "Irradiation-induced magnetism in graphite: A density functional study" *Phys. Rev. Lett.* **93**, 187202 (2004).
- [88] H. Amara, S. Latil, V. Meunier, Ph. Lambin, and J.-C. Charlier, "Scanning tunneling microscopy fingerprints of point defects in graphene: A theoretical prediction" *Phys. Rev. B* **76**, 115423 (2007).
- [89] A. Hashimoto, K. Suenaga, A. Gloter, K. Urita, and S. Iijima, "Direct evidence for atomic defects in graphene layers" *Nature* **430**, 870 (2004).

- [90] G. Lee, C. Z. Wang, E. Yoon, N. Hwang, and K. M. Ho, "Vacancy defects and the formation of local haeckelite structures in graphene from tight-binding molecular dynamics" *Phys. Rev. B* **74**, 245411 (2006).
- [91] G. Lee, C. Z. Wang, E. Yoon, N. Hwang, D. Kim and K. M. Ho, "Diffusion, coalescence, and reconstruction of vacancy defects in graphene layers" *Phys. Rev. Lett.* **95**, 205501 (2005).
- [92] I. Suarez-Martinez, A. A. El-Barbary, G. Savini, and M. I. Heggge, "First principles simulations of boron diffusion in graphite" *Phys. Rev. Lett.* **98**, 015501 (2007).
- [93] P. E. Blöchl, O. Jepsen, and O. K. Andersen, "Improved tetrahedron method for brillouin-zone integrations" *Phys. Rev. B* **49**, 16223 (1994).
- [94] S. H. Vosko, L. Wilk, and M. Nusair, "Accurate spin-dependent electron liquid correlation energies for local spin density calculations: A critical analysis" *Can. J. Phys.* **58**, 1200 (1980).
- [95] R. L. Dekock and H. B. Gray, *Chemical structure and bonding* (University Science Books, 1989).
- [96] S. S. Yu, W. T. Zheng, and Q. Jiang, "Electronic properties of nitrogen-/boron-doped graphene nanoribbons with armchair edges" *IEEE Transactions on Nanotechnology* **9**, 78 (2010).
- [97] CPMD, Copyright IBM Corporation 1999-2001, Copy-right MPI für Festkörperforschung, Stuttgart (1997-2004)
- [98] E. Kaxiras and K. C. Pandey, "Energetics of defects and diffusion mechanisms in graphite" *Phys. Rev. Lett.* **61**, 2693 (1988).
- [99] J. Cioslowski and P. Jeffrey Hay, "Electronic structure of borabenzene and its adducts with carbon monoxide and nitrogen" *J. Am. Chem. Soc.* **112**, 1707 (1990).
- [100] A. I. Boldyrev and O. P. Charkin, "Inversion of pyramidal and tetrahedral molecules AX₃ and AX₄" *J. Struct. Chemistry* **26**, 451 (1985).
- [101] M. Saito, K. Yamashita, and T. Oda, "Magic numbers of graphene multivacancies" *Jpn. J. Appl. Phys.* **46**, L1185 (2007).
- [102] Z. Tang, M. Hasegawa, T. Shimamura, Y. Nagai, T. Chiba, Y. Kawazoe, M. Takenaka, E. Kuramoto, T. Iwata, "Stable vacancy clusters in neutron-irradiated graphite: evidence for aggregations with a magic number" *Phys. Rev. Lett.* **82**, 2532 (1999)

- [103] S. M. M. Dubois, Z. Zanolli, X. Declerck, and J. C. Charlier, “Electronic properties and quantum transport in graphene-based nanostructures” *Eur. Phys. J. B* **72**, 1 (2009).
- [104] P. R. Bandaru, C. Daraio, S. Jin, and A. M. Rao, “Novel electrical switching behaviour and logic in carbon nanotube Y-junctions” *Nat. Mater.* **4**, 663 (2005).
- [105] J. Kong, N. R. Franklin, G. Zhou, M. G. Chapline, S. Peng, K. Cho, and H. Dai, “Nanotube molecular wires as chemical sensors” *Science* **287**,622 (2000).
- [106] S. Berber, Y. Kwon, and D. Tománek, “Unusually high thermal conductivity of carbon nanotubes” *Phys. Rev. Lett.* **84**, 4613 (2000).
- [107] D. L. Carroll, Ph. Redlich, X. Blase, J. C. Charlier, S. Curran, P. M. Ajayan, S. Roth, and M. Rühle, “Effects of nanodomain formation on the electronic structure of doped carbon nanotubes” *Phys. Rev. Lett.* **81**, 2332 (1998).
- [108] A. H. Nevidomskyy, G. Csányi, and M. C. Payne, “Chemically active substitutional nitrogen impurity in carbon nanotubes” *Phys. Rev. Lett.* **91**, 105502 (2003).
- [109] Y. Yagi, T. M. Briere, M. H. F. Sluiter, V. Kumar, A. A. Farajian, and Y. Kawazoe, “Stable geometries and magnetic properties of single-walled carbon nanotubes doped with 3d transition metals: A first-principles study” *Phys. Rev. B* **69**,075414 (2004).
- [110] J. Yi and J. Bernholc, “Atomic structure and doping of microtubules” *Phys. Rev. B* **47**,1708 (1993).
- [111] T. Koretsune and S. Saito, “Electronic structure of boron-doped carbon nanotubes” *Phys. Rev. B* **77**,165417 (2008).
- [112] L. Bai and Z. Zhou “Computational study of B- or N-doped single-walled carbon nanotubes as NH₃ and NO₂ sensors” *Carbon* **45**, 2105 (2007).
- [113] Z. Zhou, X. Gao, J. Yan, D. Song, and M. Morinaga “A first-principles study of lithium absorption in boron or nitrogen-doped single-walled carbon nanotubes” *Carbon* **42**, 2677 (2004).
- [114] M. Sankaran and B. Viswanathan, “Hydrogen storage in boron substituted carbon nanotubes” *Carbon* **45**, 1628 (2007).
- [115] C. Jin, K. Suenaga, and S. Iijima, “Vacancy migrations in carbon nanotubes” *Nano. Lett.* **8**, 1127 (2008).
- [116] A. V. Krasheninnikov, and F. Banhart, “Engineering of nanostructured carbon materials with electron or ion beams” *Nat. Mater.* **6**, 723 (2007).

- [117] H. J. Choi, J. Ihm, S. G. Louie, and M. L. Cohen, “Defects, quasibound states, and quantum conductance in metallic carbon nanotubes” *Phys. Rev. Lett.* **84**, 2917 (2000).
- [118] A. R. Rocha, J. E. Padilha, A. Fazzio, and A. J. R. da Silva, “Transport properties of single vacancies in nanotubes” *Phys. Rev. B* **77**,153406 (2008).
- [119] Z. Zanolli and J. C. Charlier, “Spin transport in carbon nanotubes with magnetic vacancy-defects” *Phys. Rev. B* **81**,165406 (2010).
- [120] A. V. Krasheninnikov, P. O. Lehtinen, A. S. Foster, and R. M. Nieminen, “Bending the rules: Contrasting vacancy energetics and migration in graphite and carbon nanotubes” *Chem. Phys. Lett.* **418**,132 (2006).
- [121] J. P. Perdew, K. Burke, and M. Ernzerhof, “Generalized gradient approximation made simple” *Phys. Rev. Lett.* **77**,3865 (1996).
- [122] M. Brandbyge, J. Mozos, P. Ordejón, J. Taylor, and K. Stokbro, “Density-functional method for nonequilibrium electron transport” *Phys. Rev. B* **65**,165401 (2002); J. M. Soler, E. Artacho, J. Gale, D. A. Garcia, J. Junquera, P. Ordejón, and D. Sánchez-Portal, “The SIESTA method for ab initio order-N materials simulation” *J. Phys.: Condens. Matter* **14**, 2745 (2002).
- [123] R. Landauer, “Electrical resistance of disordered one-dimensional lattices” *Philos Mag* **21**,863 (1970).
- [124] Y. Meir and N. S. Wingreen, “Landauer formula for the current through an interacting electron region” *Phys. Rev. Lett.* **68**, 2512 (1992).
- [125] S. Datta, *Electronic transport in mesoscopic systems* (Cambridge University Press 1995).
- [126] A. J. Lu and B. C. Pan, “Nature of single vacancy in achiral carbon nanotubes” *Phys. Rev. Lett.* **92**,105504 (2004).
- [127] K. E. Kweon and G. S. Hwang, “Formation, structure, and bonding of boron-vacancy pairs in graphene: A first-principles study” *Phys. Rev. B* **82**, 195439 (2010).
- [128] S. V. Morozov, K. S. Novoselov, and A. K. Geim, “Electron transport in grapheme” *Physics-Uspekhi* **51**, 744 (2008).
- [129] X. Liang, Z. Fu, and S. Y. Chou, “Graphene transistors fabricated via transfer-printing in device active-areas on large wafer” *Nano Lett.* **7**, 3840 (2007).

- [130] D. Li, W. Windl, and N. P. Padture, "Toward site-specific stamping of graphene" *Adv. Mater.* **21**, 1243 (2009).
- [131] M. Ishigami, J. H. Chen, W. G. Cullen, M. S. Fuhrer, and E. D. Williams, "Atomic structure of graphene on SiO₂" *Nano Lett.* **7**, 1643 (2007).
- [132] J. C. Meyer, C. O. Girit, M. F. Crommie, and A. Zettl, "Hydrocarbon lithography on graphene membranes" *Appl. Phys. Lett.* **92**, 123110 (2008).
- [133] M. Z. Hossain, "Chemistry at the graphene-SiO₂ interface" *Appl. Phys. Lett.* **95**, 143125 (2009).
- [134] Y. J. Kang, J. Kang, and K. J. Chang, "Electronic structure of graphene and doping effect on SiO₂" *Phys. Rev. B* **78**, 115404 (2008).
- [135] T. O. Wehling, A. I. Lichtenstein, and M. I. Katsnelson, "First-principles studies of water adsorption on graphene: The role of the substrate" *Appl. Phys. Lett.* **93**, 202110 (2008).
- [136] L. Skuja, "Optically active oxygen-deficiency-related centers in amorphous silicon dioxide" *J. Non-Cryst. Solids* **239**, 16 (1998).
- [137] Y. Xiong, S. Yao, R. Müller, M. Kaupp, and M. Driess, "From silicon(II)-based dioxygen activation to adducts of elusive dioxasiliranes and sila-ureas stable at room temperature" *Nature Chemistry* **2**, 577 (2010).
- [138] K. Raghavachari and G. Pacchioni, "Photoabsorption of dioxasilirane and silanone groups at the surface of silica" *J. Chem. Phys.* **114**, 4657 (2001).
- [139] N. Sawwan and A. Greer, "Rather exotic types of cyclic peroxides: Heteroatom dioxiranes" *Chem. Rev.* **107**, 3247 (2007).
- [140] D. G. Permenov and V. A. Radzig, "Mechanisms of heterogeneous processes in the system SiO₂ + CH₄: III. Products of >Si" *Kinetics and Catalysis* **45**, 273 (2004).
- [141] C. L. Kuo and G. S. Hwang, "Structure and interconversion of oxygen-vacancy-related defects on amorphous silica" *Phys. Rev. Lett.* **97**, 066101 (2006); references cited therein.
- [142] C. Morterra and M. J. D. Low, "Reactive silica: Novel aspects of the chemistry of silica surfaces" *Ann. N. Y. Acad. Sci.* **220**, 133 (1973).
- [143] C. L. Kuo, S. Lee, and G. S. Hwang, "Strain-induced formation of surface defects in amorphous silica: A theoretical prediction" *Phys. Rev. Lett.* **100**, 076104 (2008).

- [144] G. Henkelman, A. Arnaldsson, and H. Jónsson, “A fast and robust algorithm for Bader decomposition of charge density” *Comput. Mater. Sci.* **36**, 354 (2006).
- [145] H. Bornemann and W. Sander, “Oxidation of methyl(phenyl)silylene-Synthesis of a dioxasilirane” *J. Am. Chem. Soc.* **122**, 6727 (2000).
- [146] R. Becerra, S. J. Bowes, J. S. Ogden, J. P. Cannady, I. Adamovic, M. S. Gordon, M. J. Almond, and R. Walsh, “Time-resolved gas-phase kinetic and quantum chemical studies of the reaction of silylene with oxygen” *Phys. Chem. Chem. Phys.* **7**, 2900 (2005).
- [147] S. Nagase, T. Kudo, T. Akasaka, and W. Ando, “Theoretical study of a silylene-oxygen adduct. Is a silanone oxide structure (H_2SiOO) kinetically stable in the singlet state?” *Chem. Phys. Lett.* **163**, 23 (1989).
- [148] A. S. Zyubin, A. M. Mebel, S. H. Lin, Y. D. Glinka, “Photoluminescence of silanone and dioxasilirane groups in silicon oxides: A theoretical study” *J. Chem. Phys.* **116**, 9889 (2002).
- [149] P. E. Blöchl, O. Jepsen, and O. K. Andersen, “Improved tetrahedron method for Brillouin-zone integrations” *Phys. Rev. B* **49**, 16223 (1994).
- [150] I. Gierz, C. Riedl, U. Starke, C. R. Ast, and K. Kern, “Atomic Hole Doping of Graphene” *Nano Lett.* **8**, 4603 (2008).
- [151] T. O. Wehling, M. I. Katsnelson, and A. I. Lichtenstein, “Adsorbates on graphene: Impurity states and electron scattering” *Chem. Phys. Lett.* **476**, 125 (2009).
- [152] Y. G. Zhou, X. T. Zu, F. Gao, H. F. Lv, and H. Y. Xiao, “Adsorption-induced magnetic properties and metallic behavior of grapheme” *Appl. Phys. Lett.* **95**, 123119 (2009).
- [153] P. Häussinger, R. Lohmüller, A. M. Watson, “Hydrogen”, *Ullmann's Encyclopedia of Industrial Chemistry* (Weinheim, Wiley-VCH, 2005).
- [154] J. A. Turner, “Sustainable hydrogen production” *Science* **305**, 972 (2004).
- [155] A. Fujishima and K. Honda, “Electrochemical photolysis of water at a semiconductor electrode” *Nature* **238**, 37 (1972).
- [156] A. Kudo and Y. Miseki, “Heterogeneous photocatalyst materials for water splitting” *Chem. Soc. Rev.* **38**, 253 (2009).
- [157] J. Zhu and M. Zäch, “Nanostructured materials for photocatalytic hydrogen production” *Current opinion in colloid & interface science* **13**, 260 (2009).

- [158] K. Maeda and K. Domen, "New non-oxide photocatalysts designed for overall water splitting under visible light" *J. Phys. Chem. C* **111**, 7851 (2007).
- [159] A. Walsh, Y. Yan, M. N. Huda, M. M. Al-Jassim, and S. Wei, "Band edge electronic structure of BiVO₄: Elucidating the role of the Bi *s* and V *d* orbitals" *Chem. Mater.* **21**, 547 (2009).
- [160] R. van de Krol and M. Grätzel, *Photoelectrochemical Hydrogen Production* (Electronic Materials: Science & Technology, Springer 2011).
- [161] L. Zang, *Energy Efficiency and Renewable Energy through Nanotechnology* (Green Energy and Technology, 2011).
- [162] M. D. Hernández-Alonso, F. Fresno, S. Suárez and J. M. Coronado, "Development of alternative photocatalysts to TiO₂: Challenges and opportunities" *Energy Environ. Sci.* **2**, 1231 (2009).
- [163] X. Wang, J. C. Yu, C. Ho, Y. Hou and X. Fu, "Photocatalytic activity of a hierarchically macro/mesoporous titania" *Langmuir* **21**, 2552 (2005).
- [164] A. Kudo, K. Omori, and H. Kato, "A novel aqueous process for preparation of crystal form-controlled and highly crystalline BiVO₄ powder from layered vanadates at room temperature and its photocatalytic and photophysical properties" *J. Am. Chem. Soc.* **121**, 11459 (1999).
- [165] H. Luo, A. H. Mueller, T. M. McCleskey, A. K. Burrell, E. Bauer, and Q. X. Jia, "Structural and photoelectrochemical properties of BiVO₄ thin films" *J. Phys. Chem. C* **112**, 6099 (2008).
- [166] K. Sayama, A. Nomura, T. Arai, T. Sugita, R. Abe, M. Yanagida, T. Oi, Y. Iwasaki, Y. Abe, and H. Sugihara, "Photoelectrochemical decomposition of water into H₂ and O₂ on porous BiVO₄ thin-film electrodes under visible light and significant effect of Ag ion treatment" *J. Phys. Chem. B* **110**, 11352 (2006).
- [167] H. S. Park, K. E. Kweon, H. Ye, E. Paek, G. S. Hwang, and A. J. Bard, "Factors in the metal doping of BiVO₄ for improved photoelectrocatalytic activity as studied by scanning electrochemical microscopy and first-principles density-functional calculation" *J. Phys. Chem. C*, **115**, 17870 (2011).
- [168] H. Ye, J. Lee, J. S. Jang, and A. J. Bard, "Rapid screening of BiVO₄ based photocatalysts by scanning electrochemical microscopy and studies of their photoelectrochemical properties" *J. Phys. Chem. C* **114**, 13322 (2010)

- [169] J. D. Bierlein, A. W. Sleight, "Ferroelasticity in BiVO_4 " *Solid State Commun.* **16**, 69 (1975).
- [170] S. Tokunaga, H. Kato, and A. Kudo, "Selective preparation of monoclinic and tetragonal BiVO_4 with scheelite structure and their photocatalytic properties" *Chem. Mater.* **13**, 4624 (2001).
- [171] J. Yu and A. Kudo, "Effects of structural variation on the photocatalytic performance of hydrothermally synthesized BiVO_4 " *Adv. Funct. Mater.* **16**, 2163 (2006).
- [172] D. I. Bilc, R. Orlando, R. Shaltaf, G. M. Rignanese, J. Iniguez and Ph. Ghosez, "Hybrid exchange-correlation functional for accurate prediction of the electronic and structural properties of ferroelectric oxides" *Phys. Rev. B* **77**, 165107 (2008).
- [173] J. Wróbel, K. J. Kurzydłowski, K. Hummer, G. Kresse, and Jacek Piechota, "Calculations of ZnO properties using the Heyd-Scuseria-Ernzerhof screened hybrid density Functional" *Phys. Rev. B* **80**, 155124 (2009)
- [174] R. Wahl, D. Vogtenhuber, and G. Kresses, "SrTiO₃ and BaTiO₃ revisited using the projector augmented wave method: Performance of hybrid and semilocal functionals" *Phys. Rev. B* **78**, 104116 (2008).
- [175] A. Stroppa and S. Picozzi, "Hybrid functional study of proper and improper multiferroics" *Phys. Chem. Chem. Phys.* **12**, 5405 (2010).
- [176] Matthew W. Stoltzfus, Patrick M. Woodward, Ram Seshadri, Jae-Hyun Klepeis, and Bruce Bursten, "Structure and bonding in SnWO_4 , PbWO_4 , and BiVO_4 : lone pairs vs inert pair" *Inorg. Chem.* **46**, 3839 (2007),
- [177] W. I. F. David and I. G. Wood, "Ferroelastic phase transition in BiVO_4 : V. Temperature dependence of Bi^{3+} displacement and spontaneous strains" *J. Phys. C: Solid state phys.* **16**, 5127 (1983).
- [178] R. M. Hazen and J. W. E. Mariathasan, "Bismuth vanadate: A high pressure, high-temperature crystallographic study of the ferroelastic paraelastic transition" *Science* **216**, 991(1982).
- [179] Y. Zhang, N. A. W. Holzwarth, and R. T. Williams, "Electronic band structures of the scheelite materials CaMoO_4 , CaWO_4 , PbMoO_4 , and PbWO_4 " *Phys. Rev. B* **57**, 12738 (1998).
- [180] D. Errandonea and F. J. Manjón, "Pressure effects on the structural and electronic properties of ABX_4 scintillating crystals", *Progress in Materials Science* **53**, 711 (2008).

- [181] Ralph A. Wheeler and P. N. V. Pavan Kumar, "Stereochemically active or inactive lone pair electron in some six-coordinate, group 15 halides" *J. Am. Chem. Soc.* **114**, 4776 (1992).
- [182] J. Heyd, G. E. Scuseria, M. Ernzerhof, "Hybrid functionals based on a screened Coulomb potential" *J. Chem. Phys.* **118**, 8207 (2003); 124, 219906(E) (2006).
- [183] F. Birch, "Finite Elastic Strain of Cubic Crystals" *Phys. Rev.* **71**, 809 (1947).
- [184] Z. Zhao, Z. Li and Z. Zou, "Electronic structure and optical properties of monoclinic clinobisvanite BiVO_4 " *Phys. Chem. Chem. Phys.* **13**, 4746 (2011).
- [185] W. Yin, S. Wei, M. M. Al-Jassim, J. Turner, and Y. Yan, "Doping properties of monoclinic BiVO_4 by studied by first principles density functional theory" *Phys. Rev. B* **83**, 155102 (2011).
- [186] W. Tang, E. Sanville, and G. Henkelman, "A grid-based Bader analysis algorithm without lattice bias", *J. Phys.: Condens. Matter* **21**, 084204 (2009).
- [187] A. Stroppa and S. Picozzi, "Hybrid functional study of proper and improper multiferroics" *Phys. Chem. Chem. Phys.* **12**, 5405 (2010).
- [188] Y. Liang, T. Tsubota, L. P. A. Mooij, and R. van de Krol, "Highly improved quantum efficiencies for thin film BiVO_4 Photoanodes" *J. Phys. Chem. C* **115**, 17594 (2011).
- [189] D. K. Zhong, S. Choi, and D. R. Gamelin, "Near-complete suppression of surface recombination in solar photoelectrolysis by "Co-Pi" catalyst-modified W:BiVO_4 " *J. Am. Chem. Soc.* **133**, 18370 (2011).
- [190] P. A. Cox, *Transition metal oxides* (Oxford University Press, USA, 1992)
- [191] C. Kittel, *Introduction to solid state physics* (John Wiley & Sons, 2005)
- [192] C. Franchini, G. Kresse, and R. Podloucky, "Polaronic hole trapping in doped BaBiO_3 " *Phys. Rev. Lett.* **102**, 256402 (2009).
- [193] E. Finazzi, C. Di Valentin, G. Pacchioni, A. Selloni, "Excess electron state in Reduced Bulk Anatase TiO_2 : Comparison of standard GGA, GGA+U, and hybrid DFT calculations" *J. Chem. Phys.* **129**, 154113 (2008).
- [194] N. Aaron Deskins and M. Dupuis, "Electron transport via polaron hopping in bulk TiO_2 : A density functional theory characterization" *Phys. Rev. B* **75**, 195212 (2007).

- [195] R. Bharati and R.A. Singh, “Electrical conduction in manganese tungstate” *J. Phys. Chem. Solids* **43**, 641 (1982).
- [196] D. Emin, “Small polarons” *Phys. Today* (1982).
- [197] M. D. Volnyanskiĭ, A.Yu. Kudzin, S. N. Plyaka, and Z. Balasme, “Charge transport in PbMoO_4 crystals” *Phys. Solid State* **46**, 2012 (2004).
- [198] J. Su, L. Guo, N. Bao, and C. A. Grimes, “Nanostructures $\text{WO}_3/\text{BiVO}_4$ heterojunction films for efficient photoelectrochemical water splitting” *Nano Lett.* **11**, 1928 (2011).

Vita

Kyoung Eun Kweon was born in Bucheon, Korea, on November 15, 1981, the daughter of Youngman Kweon and Jungyoon Shim. After graduating from Bucheon Women High School in Bucheon, she entered Yonsei University in Seoul. With one year as exchange student in University of California, Santa Barbara, she graduated from Yonsei University with a Bachelor of Science in Electrical and Electronic Engineering in June of 2005. In August 2005, she entered Graduate School of the University of Texas at Austin. She joined Computational Nanoengineering Laboratory Group in January 2006 and began research under the guidance of Professors Gyeong S. Hwang in Chemical Engineering. She received a Master of Science degree in Electrical Computer Engineering in May of 2007 and continued to pursue Ph.D. in Electrical Computer Engineering. Her Ph.D. topic is first-principles calculations for defects and impurities in nanomaterials, particularly metal oxide materials for solar energy applications. She will continue her investigation on finding highly efficient metal oxide photocatalysts for solar hydrogen production from water splitting.

Permanent address: 3600 Greystone Dr. #546
Austin, TX 78731

This manuscript was typed by the author.